

THERMOELECTRICITY AND HEAT CONDUCTION IN III-V NANOWIRES

THERMOELECTRICITY AND HEAT CONDUCTION IN III-V NANOWIRES

By ARA GHUKASYAN, B.Sc.

A Thesis Submitted to The School of Graduate Studies in Partial Fulfillment of The Requirements
for The Degree Doctor of Philosophy

McMaster University

© Copyright by Ara Arayik Ghukasyan, March 2022

DOCTOR OF PHILOSOPHY (2022)
(Engineering Physics)

McMaster University
Hamilton, Ontario

TITLE: Thermoelectricity and Heat Conduction in III-V Nanowires
AUTHOR: Ara A. Ghukasyan, B.Sc. (McMaster University)
SUPERVISOR: Dr. R.R. LaPierre

NUMBER OF PAGES: xxi, 146

Lay Abstract

In a circuit of dissimilar conductors, temperature differences create voltage differences that can drive electrical currents. Similarly, electrical currents in such circuits inherently lead to heating *and* cooling. These phenomena are known as thermoelectric effects because they couple heat and charge transport (electricity) in a symmetric and reversible way. The goal of some thermoelectric devices (TEDs) is to exploit these effects to generate electrical power or to provide controlled cooling. However, greater conversion efficiencies are required to compete against other existing technologies.

With the advent of nanofabrication, semiconductor nanowires (NWs) have emerged as an attractive material system for efficient TEDs. In this thesis, we explore their thermal and electronic properties. We demonstrate a novel way to measure the NW thermal conductivity and employ computational methods to examine heat transport in NWs with various crystal structures. Finally, we examine how synthesis conditions can determine the morphology of NWs.

Abstract

Thermoelectric devices (TEDs) are useful in a variety of niche applications, but low efficiencies limit their broader application. Semiconductor nanowires (NWs) could be the key to efficient thermoelectrics, through the benefits of one-dimensional band structures and a greatly reduced thermal conductivity. This thesis explores the transport fundamentals, experimental characterization, and computational approaches relevant to prospective III-V NW TEDs.

Predictive electronic transport models are outlined for NWs and bulk III-Vs. These models are used to determine the optimum carrier concentration for maximizing the thermoelectric figure of merit (ZT) in the bulk and in NWs of arbitrary size. We demonstrate the physical mechanisms underlying electronic thermoelectric improvements in NWs and confirm the superior performance of InSb and InAs, among other III-Vs.

Next, thermal conductivity reduction in structurally complex NWs is investigated as a means of improving ZT . We compare polytypic and twinning superlattice (TSL) GaAs NWs in measurements obtained by a novel application of the 3ω method. We find thermal conductivities of 8.4 ± 1.6 W/m-K and 5.2 ± 1.0 W/m-K for the polytypic and TSL NWs, respectively, demonstrating a significant difference and an almost ten-fold reduction compared to 50 W/m-K of bulk GaAs.

We employ molecular dynamics simulations and the atomistic Green's function method to address phonon engineering in generalized GaAs NW structures. In

comparing twinning NWs, we find that a TSL period of 50 Å minimizes the lattice thermal conductivity across all the diameters considered. Our results also illustrate the importance of NW surfaces versus the internal crystal structure. Phonon coherence lengths are obtained by analyzing thermal conductivity trends in periodic and aperiodic structures. Transmission spectra are calculated to reveal the phonon frequencies targeted by structural engineering in NWs. These findings explain the range of thermal conductivities obtained for GaAs NWs with various crystal phases.

Finally, to inform future growths of TSL NWs, we study the influence of the substrate temperature and V/III flux ratio on TSL formation in Te-doped GaAs NWs. The crystal structure of several NWs is investigated using transmission electron microscopy, revealing a range of polytypic and TSL morphologies. We find that periodic TSLs form only at low V/III flux ratios of 0.5 and substrate temperatures of 492 to 537 °C. To explain these trends, we derive a phase diagram for TSL NWs based on a kinetic growth model.

Acknowledgements

My sincere gratitude to the members of my advisory committee, Drs. John Preston and Rafael Kleiman, for the insight that challenged and motivated this work. For the opportunity to start this journey, the encouragement to continue, and the guidance to succeed, I thank my thesis supervisor, Dr. Ray LaPierre.

To past members of the LaPierre Group, especially Nebile Goktas, Mitch Robson, and Simon McNamee: Thank you for your patience and everything you taught me. I would also like to thank current members, Paige Wilson, for helping me get started with computational methods and Curtis Goosney, for his friendship and company in recent times of social isolation. A special thanks to Tahereh Majdi for her invaluable help with developing the 3ω measurement system.

To my family and loved ones, thank you for enduring with me.

The growth, processing, and characterization of nanowires for this work was enabled by facilities at the CEDT, the TNFC (at the University of Toronto), and the CCEM. Computational work was made possible by SHARCNET (www.sharcnet.ca) and Compute/Calcul Canada. I am grateful for funding from the Natural Sciences and Engineering Research Council of Canada, which enabled this research.

I dedicate this work to my grandparents, Elga and Pavlik.

Table of Contents

LAY ABSTRACT	III
ABSTRACT	IV
ACKNOWLEDGEMENTS	VI
TABLE OF CONTENTS.....	VIII
LIST OF FIGURES	XI
LIST OF TABLES	XVI
LIST OF ABBREVIATIONS AND SYMBOLS.....	XVII
DECLARATION OF ACADEMIC ACHIEVEMENT	XXI
1. BACKGROUND.....	1
1.1. THERMOELECTRICS	1
1.2. NANOSCALE THERMOELECTRICS	4
1.3. EXISTING RESULTS ON NANOWIRE THERMOELECTRICS	7
1.4. NANOWIRE THERMAL CONDUCTIVITY.....	10
1.5. PHONON ENGINEERING IN NANOWIRES.....	12
1.6. TUNABLE THERMAL CONDUCTIVITY.....	14
1.7. THESIS OVERVIEW	16
2. BOLTZMANN TRANSPORT MODEL	18
2.1. SUMMARY	18
2.2. INTRODUCTION	19
2.3. THERMOELECTRIC EFFECTS.....	20
2.3.1. <i>The Seebeck Effect</i>	20
2.3.2. <i>The Peltier Effect</i>	24
2.3.3. <i>The Thomson Effect</i>	25

2.4.	THE FIGURE OF MERIT	28
2.5.	ELECTRONIC BAND STRUCTURE	30
2.6.	TRANSPORT FORMALISM	33
2.7.	THE RELAXATION TIME APPROXIMATION	37
2.8.	NANOWIRE TRANSPORT COEFFICIENTS	39
2.9.	BULK TRANSPORT COEFFICIENTS	45
2.10.	RESULTS AND DISCUSSION.....	54
2.11.	CONCLUSIONS	60
3.	MEASUREMENTS OF NANOWIRE THERMAL CONDUCTIVITY	62
3.1.	SUMMARY	62
3.2.	INTRODUCTION	63
3.3.	NANOWIRE GROWTH AND CHARACTERIZATION	65
3.4.	DEVICE FABRICATION	67
3.5.	3ω MEASUREMENTS.....	68
3.6.	3ω DATA FITTING.....	70
3.7.	RESULTS AND DISCUSSION.....	72
3.8.	CONCLUSIONS	76
4.	SIMULATIONS OF HEAT TRANSPORT IN NANOWIRES	77
4.1.	SUMMARY	77
4.2.	INTRODUCTION	78
4.3.	GENERALIZING NANOWIRE STRUCTURES	80
4.4.	COMPUTATIONAL METHODS	82
4.5.	RESULTS AND DISCUSSION.....	83
	4.5.1. <i>Thermal Conductivity</i>	83
	4.5.2. <i>Transmission Functions</i>	90
4.6.	CONCLUSIONS	92

5.	PHASE DIAGRAM FOR TWINNING SUPERLATTICE NANOWIRES	94
5.1.	SUMMARY	94
5.2.	INTRODUCTION	95
5.3.	METHODS.....	96
5.4.	RESULTS AND DISCUSSION.....	98
5.5.	CONCLUSIONS	105
6.	SUMMARY AND FUTURE WORK	106
6.1.	THESIS SUMMARY	106
6.2.	FUTURE WORK	109
	REFERENCES	113
	APPENDIX.....	133
I.	FIGURE OF MERIT FOR VARIOUS NANOWIRE MATERIALS	133
II.	BULK SCATTERING AND BAND FORMULAE	134
III.	3ω PARAMETERS AND SUPPLEMENTARY INFORMATION	136
a.	<i>Nanowire Growth.....</i>	136
b.	<i>Heater Line Resistance Coefficients</i>	138
c.	<i>Model Sensitivity.....</i>	140
d.	<i>Tables of Fitted Parameters.....</i>	142
IV.	COMPUTATIONAL DETAILS	144
a.	<i>Molecular Dynamics.....</i>	144
b.	<i>Atomistic Green's Function</i>	145

List of Figures

- Figure 1.1** Shape of the electronic density of states (eDOS) for a one-, two-, and three-dimensional (bulk) electron gas. E_0 indicates the bulk conduction band edge. The remaining energy labels indicate sub-band edges in the one- and two-dimensional cases. **5**
- Figure 1.2** Electron distributions at the carrier concentrations maximizing the power factor ($S^2\sigma$) for bulk (blue) and 10 nm diameter NW (red) GaAs, at 300 K. Areas of the shaded regions measure the equilibrium electron concentrations. Here, both the 1D and 3D systems have $S \approx -150 \mu\text{V/K}$. However, the maximum power factor is much larger in the 1D case (17.3 vs. 2.0 mW/m-K²), because $\sigma_{1\text{D}} = 7300 \text{ S/cm}$, while $\sigma_{3\text{D}} = 860 \text{ S/cm}$. **6**
- Figure 2.1** A thermoelectric circuit illustrating the origin of the Seebeck effect. The larger area under the red distribution plot indicates an excess of free electrons on the hot side. Potential energy is stored in the electron concentration gradient and is measured per unit charge as $\Delta V_{\text{oc}} = S(T_{\text{h}} - T_{\text{c}})$. The current in the circuit, I , only appears once the switch is closed. **21**
- Figure 2.2** A thermoelectric circuit illustrating the origin of the Peltier effect. Electrons absorb or expel energy as they traverse the discontinuous energy levels across different materials, leading to local cooling or heating of the surroundings. **25**
- Figure 2.3** Total (dashed) and individual scattering rates in an InSb NW at 300 K with (a) background impurity and (b) remote impurity scattering. The NW diameter is 20.0 nm and $n = 4.36 \times 10^{16} \text{ cm}^{-3}$. **42**
- Figure 2.4** Elastic and inelastic scattering rates for bulk III-V semiconductors, shown here for InSb at (a) the optimum carrier concentration of $n = 1.79 \times 10^{17} \text{ cm}^{-3}$ and (b) at the intrinsic carrier concentration, both at 300 K. Panels (c) and (d) show the differential electric current density (proportional to the transport distribution) in either case. The distribution is smoothed by stronger elastic scattering due to ionized impurities in (a) and (c). **50**

- Figure 2.5** Thermoelectric transport coefficients calculated for bulk III-V semiconductors at 300 K. The magnitude of the Seebeck coefficient (a) is calculated using Eq. (2.108), which yields negative values of S , as required. The electrical conductivity (b) and the electronic thermal conductivity (c) are given by Eq. (2.106) and (2.110), respectively. The dimensionless figure of merit (d) is calculated in the usual way (Eq. (1.1)) using the bulk lattice thermal conductivity. **55**
- Figure 2.6** Thermoelectric transport coefficients calculated for 10 nm diameter NWs at 300 K. The total value of all transport coefficients is shown, using the total scattering rate obtained from Matthiessen's rule applied over Eqs. (2.63) to (2.69), with $R = 5$ nm. The magnitude of the Seebeck coefficient (a) is the conductivity-weighted sum over terms given by Eq. (2.80). The total electrical conductivity and electronic thermal conductivity are calculated by summing over terms given by Eq. (2.76) and (2.83), respectively. The figure of merit (d) is calculated from the total values in the other panels, along with the thermal conductivity curves taken from Ref. 73. **56**
- Figure 2.7** Thermoelectric transport coefficients calculated for 1 nm diameter NWs at 300 K. The total value of all the transport coefficients is shown. The same equations were used as for Figure 2.6, except with $R = 0.5$ nm. **57**
- Figure 2.8** (a) Maximum thermoelectric figure of merit for NW diameters as fraction of the thermal de Broglie wavelength of the corresponding material, where the minimum diameter is 1 nm and the maximum is λ_D . (b) The electron concentrations that maximize the figure of merit for the corresponding material. Dashed lines in both plots indicate the values for remote impurities. **59**
- Figure 2.9** Thermoelectric figure of merit of large diameter NWs. **60**

- Figure 3.1** Models of three-dimensional structures for (a) polytypic zincblende/wurtzite (ZB/WZ) and (b) ZB-twinning superlattice (ZB-TSL) NWs, showing [111]A and [111]B surface faceting in the latter. (c) Bilayer stacking in the TSL, as seen in an orthogonal projection along $[11\bar{2}]$, exhibiting reversal of the normal ABC stacking sequence across the twin plane. (d) Twinning is equivalent to a rotation of the crystal structure about the NW axis by 60° , illustrated by tetrahedral primitives of bulk GaAs. The indicated growth direction applies to the entire figure. **64**
- Figure 3.2** (a) SEM image of the NW array from sample B. (b) SEM image of a NW top, showing surface faceting due to a TSL. (c) Size and morphology comparison in side-by-side TEM images of a polytypic NW from sample A (left) and a TSL NW from sample B (right). (d) HRTEM image near the centre of the same NW from sample A, showing polytypic NW structure. (e) HRTEM image near the center of the TSL in sample B. (f) Selective-area electron diffraction pattern confirming ZB twins in the TSL region of sample B. **66**
- Figure 3.3** (a) Diagrams illustrating the device layers used to model heat conduction: (1) the electrically insulating BCB excess, (2) the target NW-BCB composite layer, and (3) the silicon substrate. (a) Schematic of the device. Inset shows the heater line and four contact pads. (b) Cross-sectional SEM image of a device from sample B. **68**
- Figure 3.4** (a) Measured temperature amplitudes for samples A, B, and C, along with fitted curves, for the in-phase and out-of-phase (inset) components of each. (b) Thermal conductivity of GaAs NWs, with the polytypic ZB/WZ NWs (red, sample A) and the TSL NWs (blue, sample B) data points corresponding to measurements in panel (a). For comparison, the white markers indicate the experimental results of Juntunen et al.³⁶ and Soini et al.³³ The dashed and dotted lines represent theoretical results from Mingo et al.⁸⁸ and Martin et al.,¹²⁹ respectively, with Δ indicating surface roughness for the latter. **73**

- Figure 4.1** Orthographic and perspective views of several representative NW structures studied in Chapter 4. (a) A faceted TSL NW with a twin segment length of 7 bilayers. (b) A non-faceted TSL NW structure with the same periodicity as (a). (c) A NW exhibiting random polytypism with a ZB/WZ ratio of 50%. (d) A single-crystalline ZB NW. (e) A single-crystalline WZ NW. Corresponding three-dimensional models are shown below each structure in (a)-(e). Horizontal lines in (a)-(e) represent the twin or polytypic boundaries. The faceted TSL NW in (f) spans the length of the simulation cell used in NEMD calculations and is shown here at the largest diameter studied (100 Å). **80**
- Figure 4.2** (a) NEMD results for the thermal conductivity of non-faceted TSL NWs (ZBT(n), red) and faceted TSL NWs (ZBTF(n), green) versus twin period (bottom axis) or twin segment length in bilayers, n , (top axis). (b) Thermal conductivity versus ZB ratio in ZBWZ(x) (blue) and ZBT(n) (red). Diameters are indicated by the line weight. Dashed lines (black) correspond to the pristine ZB NW thermal conductivities. **84**
- Figure 4.3** NEMD thermal conductivity for (a) ZBT(x) and (b) ZBWZ(x) versus thermal conductivity in the incoherent limit (dotted lines). Corresponding values of r and l_c are shown in Table 4.2. **89**
- Figure 4.4** (a) Values of the transmission function $\mathcal{T}(\omega)$ for pristine WZ and ZB, as well as several intermediate twinning structures, for NW diameters of 50 Å. In the lower panel of (a), transmission functions are normalized by the ZB transmission. (b) Phonon dispersion and density of states (DOS) for the WZ NW. **90**
- Figure 5.1** (a) Three-dimensional morphology of a TSL NW, with arrows indicating the growth direction and the surface microfacet orientations in one period of the TSL. (b) Bilayer stacking sequence for a ZB TSL nanowire, illustrating reversal (mirroring) of the stacking sequence across the twin boundary. Included for comparison, bilayer stacking sequences in (c) ZB and (d) WZ NWs. (e) Stacking sequence of tetrahedral primitives for each structure type. Yellow and red atoms represent Ga and As, respectively. **96**
- Figure 5.2** (a) SEM image of a self-assisted GaAs NW array grown at 537 °C, with a V/III ratio of 0.5. (b) A corresponding HRTEM image showing twinning at the top of a NW. **97**

Figure 5.3	Data points at different growth temperatures and V/III flux ratios. Green (TSL) and red (non-TSL) markers indicate the resulting NW morphology. The estimated TSL and non-TSL regions are colored green and red, respectively, with the boundary determined by critical curves calculated from Eqs. 5.5 and 5.6, for $\lambda_3(T_0)/R$ from 11 to 30. Corresponding images of GaAs NW tops showcase the different crystal structures: (a) TEM image showing ZB with low fault density, (b) TEM image showing random ZB twins, (c) HRTEM (left) and TEM (right) showing “pseudoperiodic” TSL, (d) TEM showing periodic TSL, and (e) HRTEM showing a high fault density.	99
Figure A1	Maximal ZT values (at various temperatures) for recent (a) p-type and (b) n-type NW thermoelectrics. Reprinted with permission from Ref. 25.	133
Figure A2	Growth conditions over time, showing the substrate temperature and actual dopant concentration.	137
Figure A3	Temperature dependence of the line resistance for sample A.	138
Figure A4	Temperature dependence of the line resistance for sample B.	139
Figure A5	Temperature dependence of the line resistance for sample C.	139
Figure A6	Sensitivity of the objective function versus perturbations about the optimal point. The upper three curves indicate a strong sensitivity to the thermal conductivities of the BCB and NW-BCB layers, as well as the volumetric heat capacity of the BCB. A weaker sensitivity to the substrate (p ⁺ -Si) thermal conductivity is also seen.	141
Figure A7	Thermal penetration depth (q^{-1}) in μm , calculated using Eq. (A21), using a range of values for BCB and the NW-BCB composite from Tables A1-A4.	141
Figure A8	Saturation of the thermal conductivity in non-equilibrium molecular dynamics simulations. Data points correspond to a pristine zincblende nanowire with diameter 50 Å.	144
Figure A9	An illustration of the NW system used for atomistic Green’s function calculations. Two semi-infinite “contacts” connect to either end of the “device”, here consisting of one zincblende unit cell. A NW with diameter 35 Å is shown for clarity.	146

List of Tables

Table 1.1	Summary of NW measurements discussed in Chapter 1.	9
Table 2.1	Material parameters used for all calculations in Chapter 2.	54
Table 4.1	Summary of thermal conductivity extrema (in W/m-K) obtained by NEMD simulations.	85
Table 4.2	Coherence length (l_c) and interfacial thermal resistance (r) between WZ and ZB segments.	89
Table A1	Fitted parameter values for sample A.	143
Table A2	Fitted parameter values for sample B.	143
Table A3	Fitted parameter values for sample C.	143

List of Abbreviations and Symbols

AC	acoustic deformation potential
AGF	atomistic Green's function
BTE	Boltzmann transport equation
COP	coefficient of performance
DOS	density of states
HR	high resolution
II	ionized impurity
MBE	molecular beam epitaxy
NEMD	non-equilibrium molecular dynamics
NW	nanowire
PE	piezoelectric
PO	polar-optical
RTA	relaxation time approximation
SA	self-assisted
SEM	scanning electron microscopy
TEC	thermoelectric cooler
TED	thermoelectric device
TEG	thermoelectric generator
TEM	transmission electron microscopy
TSL	twinning superlattice
VLS	vapour-liquid-solid
WZ	wurtzite
ZB	zinblende
ZBRWZ	zinblende with random wurtzite
ZBT	zinblende twinning
ZBTF	zinblende twinning with facets

ZT	thermoelectric figure of merit
S	Seebeck coefficient
Π	Peltier coefficient
t	Thomson coefficient
ΔV_{oc}	open circuit voltage
σ	electrical conductivity
T	temperature
κ_e	electronic thermal conductivity
κ_L	lattice thermal conductivity
$S^2\sigma$	thermoelectric power factor
$P_{in/out}$	rate of electrical energy input/output
η_{TEG}	efficiency of a thermoelectric generator
ϕ_{TEC}	coefficient of performance of a thermoelectric cooler
α	energy band non-parabolicity parameter
E_g	energy band gap
E_F	Fermi energy (or chemical potential)
E_j	relaxation-time-averaged electron energy
$E_{l,u}$	energy eigenvalues in a cylindrical quantum well
E_{ac}	acoustic deformation potential
J_l	ordinary Bessel function of order l
I_ν	modified Bessel function of the first kind of order ν
K_ν	modified Bessel function of the second kind of order ν
Θ	Heaviside step function
\mathcal{N}	degeneracy of minima in the electronic band structure
ρ^{3D}	electron density of states in a 3-dimensional band structure
ρ^{1D}	electron density of states in a 1-dimensional band structure
F	total electric field
ε	negative voltage gradient in space
ψ	electrochemical potential
f_0	Fermi-Dirac distribution function

f	non-equilibrium electron distribution function
g	perturbation component of the electron distribution
λ_D	thermal de Broglie wavelength
\hbar	reduced Plank's constant
m^*	electron effective mass
m_e	free electron mass
e	elementary charge
k_B	Boltzmann constant
\mathcal{D}	phonon density of states
C_v	lattice heat capacity
l_{ph}	phonon mean-free-path
v	velocity
ω	angular frequency
ω_{po}	polar optical phonon frequency
N_{po}	occupation number of polar-optical phonons
N_I	density of ionized impurities
$\tau_{(i)}$	scattering/relaxation rate for a mechanism (i)
τ	total scattering/relaxation rate
p	specularity parameter
k	wave number
f_0	the Fermi-Dirac distribution
J	charge current density
Q	heat current density
E	energy
J_E	energy flux
ρ_E	energy density
$\epsilon_{S/\infty}$	low/high frequency dielectric permittivity
ϵ_0	permittivity of free space
c_l	longitudinal elastic constant
\mathcal{P}	piezoelectric coefficient

$S_{\text{in/out}}^{\pm}$	inelastic scattering function in Rode's method
ξ	initial perturbation distribution in Rode's method
$\tilde{\theta}_{2\omega,\text{rms}}$	measured temperature rise of the heater line
\tilde{T}_h	calculated temperature rise for the heater line
$\bar{\epsilon}$	mean squared error
κ_A	nanowire array thermal conductivity (polytypic sample)
κ_B	nanowire array thermal conductivity (twinning sample)
κ_{eff}	effective thermal conductivity
R	nanowire radius
L_{NW}	nanowire length
A_{NW}	nanowire cross-sectional area
N_{int}	number of crystal interfaces in a nanowire
l_c	phonon coherence length
r	interfacial thermal resistance
n_z	number of atomic bilayers in a nanowire
a_z	atomic bilayer spacing
\mathcal{T}	phonon transmission function
β	Ga droplet contact angle
v_3	atomic flux of Ga
v_5	atomic flux of As
v_5^{des}	desorption flux of As
λ_3	Ga adatom diffusion length
α_3	Ga beam angle with respect to the substrate
α_5	As ₂ beam angle with respect to the substrate
ϵ	As re-emission constant
B	Arrhenius coefficient for Ga adatom diffusion
C	Arrhenius coefficient for Ga adatom desorption
T_0	temperature for maximum Ga adatom diffusion

Declaration of Academic Achievement

This work contains material that was previously published in academic journals. I, Ara Ghukasyan, acknowledge the contribution of the following collaborators, whose efforts were essential to this work.

Transmission electron micrographs in Chapters 3 and 5 were obtained by Nebile Goktas, who also oversaw the growth of nanowires for Chapter 5. The 3ω method was implemented in a joint effort with Pedro Oliveira (undergraduate student under my supervision). Technicians Alex Tsukernik and Shahram Ghanad-Tavakoli operated the electron beam lithography and molecular beam epitaxy systems, respectively.

My supervisor, Dr. Ray LaPierre, and members of my advisory committee, Drs. Preston and Kleiman, provided guidance throughout the course of this project. Nanowire growth models in Chapter 5 were developed with Dr. Vladimir Dubrovskii at St. Petersburg State University.

All other work, including the authorship of this document, is solely my own. To the best of my knowledge, this work does not infringe on any copyrights.

1. Background

1.1. Thermoelectrics

The global demand for clean and renewable energy is an issue of ever-increasing importance in the modern world, and a variety of large-scale solutions have been developed to meet this demand in a more sustainable way. This includes nuclear, hydroelectric, wind, and photovoltaic power systems. At the same time, there is a growing necessity for smaller, portable, and remote electrical power systems in, for example, low-light conditions precluding the use of photovoltaics or in weight-limited applications, where sufficient battery life is unavailable. Thermoelectric generators (TEGs) represent a reliable alternative in such cases; being compact, having no moving parts, producing no waste, and requiring minimal maintenance. TEGs can also be used to recover energy from waste heat produced in automotive and industrial processes, thereby improving the overall efficiency or powering auxiliary systems.¹

The basic operating principle of all thermoelectric devices (TEDs) relies on the direct and reversible conversion between differences in temperature and electrical potential. In the presence of a temperature gradient, TEGs provide a proportional potential difference via the Seebeck effect, which can be used to drive an electrical current. Conversely, when an external power source drives a current through a TED, a proportional amount of heat is pumped via the complementary Peltier effect. In this alternate mode of operation, the TED functions as a solid-state heat pump, cooling one

side of the device while heating the other. Thermoelectric coolers (TECs) based on the Peltier effect (sometimes called “Peltier elements”) provide a compact and silent means of refrigeration, in contrast to traditional systems.²

Widespread use of TEDs—for both power generation and refrigeration—is hindered by the comparably low conversion efficiencies and coefficients of performance of TEGs and TECs, respectively. This limits their applications to niche cases, where size and reliability take precedence over the absolute efficiency. A dimensionless, temperature-dependent quantity called the “thermoelectric figure of merit” is most often used to holistically quantify thermoelectric materials.³ A material’s figure of merit is given by

$$ZT = \frac{S^2 \sigma T}{\kappa_e + \kappa_L} \quad (1.1)$$

where T is the absolute temperature, S is the Seebeck coefficient (or sometimes “thermopower”), σ is the electrical conductivity, and κ_L/κ_e are the lattice/electronic thermal conductivities, respectively. In view of Eq. (1.1), a large ZT corresponds to a higher open-circuit voltage, given large $|S|$; a higher maximum power output, given high σ ; and lower parasitic heat conduction, given a smaller total thermal conductivity, $\kappa = \kappa_L + \kappa_e$. All these quantities vary with temperature and are collectively referred to as the “thermoelectric transport coefficients”. The figure of merit, accordingly, has a maximum at some temperature for a given thermoelectric material, indicating the point of maximum efficiency. Improving ZT is the central goal of thermoelectrics research.

In principle, thermoelectricity is observed in any material with a finite electrical conductivity, provided there exists a connection to another conductor somewhere within the circuit. In practice, however, only semiconductors exhibit large enough Seebeck coefficients to be viable for energy conversion or cooling, with typical $|S| \approx 100 \mu\text{V/K}$. For metals, S is usually one or two orders of magnitude smaller (and it is well known that $S = 0$ in superconductors).⁴ The much higher σ of metals does not offset the low ZT owing to their small values of S . Rather, high electrical conductivity is itself offset by a high electronic thermal conductivity (κ_e), which increases proportionally as per the Wiedemann-Franz law.⁵ Nonetheless, some specialized metallic alloys (for example, alumel and chromel) are staple materials for thermocouples used in temperature measurement.³

Traditional TEDs are based on Bi_2Te_3 or related materials and achieve a maximum $ZT \approx 1$ near room temperature (efficiency $\sim 10\%$). A comparable ZT is achieved in PbTe near $T \approx 600$ K, which is perhaps more suitable for waste heat recovery. The most efficient commercial TEDs achieve $1 < ZT < 2$ around 500 to 900 K. These are based on complex chalcogenides⁶ or skutterudite compounds.⁷ $\text{Si}_{1-x}\text{Ge}_x$ alloys are the dominant thermoelectric material for very high temperature applications, exhibiting a maximum $ZT \approx 1$ near 1200 K. Perhaps most famously, $\text{Si}_{1-x}\text{Ge}_x$ TEGs powered by a decaying radioisotope (as a heat source) have been used by NASA on *Voyager*, *Cassini*, and many other projects^{1,8} as reliable on-board power systems.

1.2. Nanoscale Thermoelectrics

An ongoing interest in nanostructured or “low dimensional” materials—*i.e.*, thin films, nanowires (NWs), and quantum dots—was sparked in theoretical studies^{9,10} by Hicks and Dresselhaus in the early 1990s, wherein a significant ZT enhancement was predicted via an increase of the power factor, $S^2\sigma$ (in the numerator of Eq. (1.1)). Nanoscale materials, in general, have distinct electronic properties compared to their bulk counterparts.¹¹ The resulting thermoelectric improvements can be understood as follows.

The electronic band structure of nanoscale materials is altered by confinement of the wave function in a potential well (the specimen) of comparable physical size. In quantum wires or two-dimensional quantum wells, the electron remains “free” in one or two directions, respectively. The result of this partial confinement is the splitting of bulk energy bands (allowed electron states) into sub-bands offset by the discrete confinement energies.¹¹ Crucially, the electronic density of states (eDOS) in these sub-bands differs drastically from the bulk, as shown qualitatively in Figure 1.1.

The one- and two-dimensional eDOS, unlike the bulk, are non-zero at the lowest energy states in the conduction band. This strongly affects the thermoelectric transport coefficients, which depend directly on the energy distribution of charge carriers. One component of the power factor, σ , increases with the number of conduction electrons, as determined by the overlap of the Fermi-Dirac distribution⁵ and the eDOS. The other component, S , grows in magnitude with the *difference* between the Fermi energy (or

chemical potential), E_F , which characterizes the occupation probability, and the average energy of conducting electrons, E_J . The other component, $|S|$, is maximized when E_F is below the band edge, where the difference between E_F and the E_J becomes large. However, a lower E_F also corresponds to lower σ , because the overlap with the eDOS will be smaller.

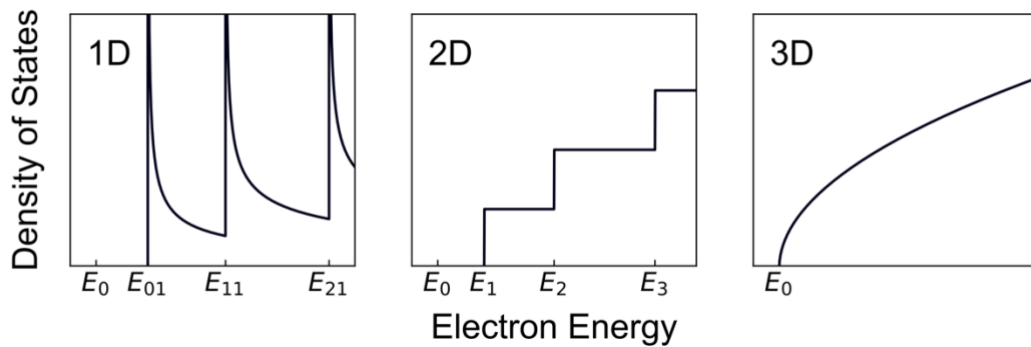


Figure 1.1: Shape of the electronic density of states (eDOS) for a one-, two-, and three-dimensional (bulk) electron gas. E_0 indicates the bulk conduction band edge. The remaining energy labels indicate sub-band edges in the one- and two-dimensional cases.

Thus, $|S|$ and σ have an opposing dependence on E_F . This presents a compromise that is more favourable in low-dimensional band structures, which feature many more low-energy states (*i.e.*, a large eDOS at the band edge). Accordingly, σ can be higher while E_F is low enough to ensure a large $|S|$, yielding higher $S^2\sigma$ compared to the bulk. Figure 1.2 illustrates this result for a 10 nm diameter GaAs NW. This enhancement is in theory greater for NWs^{9,12} (quantum wires) than for thin layers¹⁰ (quantum wells). In fact, the optimal shape for the electron distribution (shaded regions in Figure 1.2) is a “delta function” spike,¹³ which the 1D case approximates most closely.

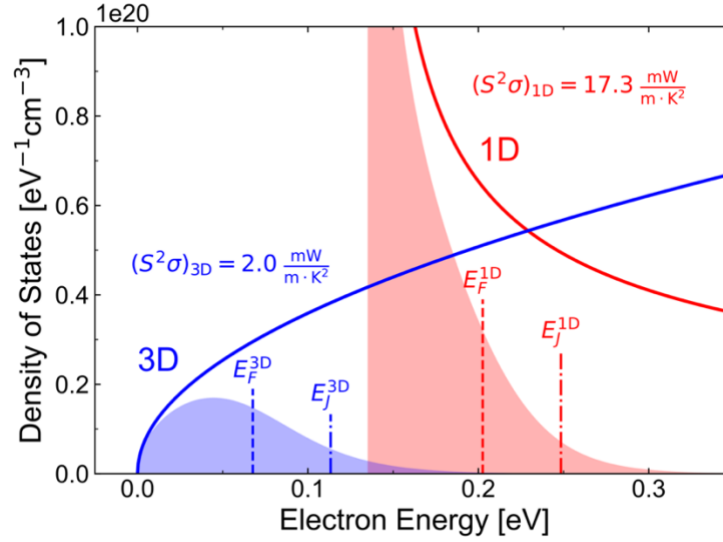


Figure 1.2: Electron distributions at the carrier concentrations maximizing the power factor ($S^2\sigma$) for bulk (blue) and 10 nm diameter NW (red) GaAs, at 300 K. Areas of the shaded regions measure the equilibrium electron concentrations. Here, both the 1D and 3D systems have $S \approx -150 \mu\text{V/K}$. However, the maximum power factor is much larger in the 1D case (17.3 vs. 2.0 $\text{mW/m}\cdot\text{K}^2$), because $\sigma_{1\text{D}} = 7300 \text{ S/cm}$, while $\sigma_{3\text{D}} = 860 \text{ S/cm}$.

In NW structures, charge carriers are bulk-like in the axial direction, given a long enough NW, and quantum confined perpendicular to the axis (radially), given a small enough diameter. The threshold confinement size can be approximated by the thermal de Broglie wavelength¹⁴ of the electron:

$$\lambda_D = \sqrt{\frac{2\pi\hbar^2}{m^*k_B T}} \quad (1.2)$$

Here, \hbar is the reduced Planck's constant ($\approx 1.055 \times 10^{-34} \text{ J}\cdot\text{s}$), k_B is the Boltzmann constant ($\approx 1.381 \times 10^{-23} \frac{\text{m}^2\text{kg}}{\text{s}^2\text{K}}$), and m^* is the effective mass—the only material parameter. From Eq. (1.2) at room temperature, the wavelength of electrons is around

20 to 50 nm in III-V semiconductors (GaAs, InAs, InSb, InP, etc.). NWs of a comparable diameter remain difficult to produce reliably in ordered and free-standing arrays for macro-scale devices. Practical quantum confinement in p-type NWs is, for the same reason, even more difficult to achieve since much smaller values of λ_D result for holes (electron vacancies in semiconductors), the majority of which are significantly “heavier”.

Despite this difficulty, several studies on *individual* NWs have produced encouraging results in terms of ZT increases due to a reduced lattice thermal conductivity (κ_L). Some of the key challenges in optimizing the power factor can also be gleaned from these works.

1.3. Existing Results on Nanowire Thermoelectrics

Among the earliest works on NW thermoelectrics is a 2006 study by Mavrokefalos et al.,¹⁵ where InAs NWs with a rectangular cross section (equivalent-area diameter ≈ 90 nm) were examined. These NWs were formed by selective etching of an InAs film grown on lattice-mismatched GaAs. Strain-induced dislocations led to a low electrical conductivity (14 S/cm), thus reducing the thermoelectric efficiency. Later, in 2007, Seol et al.¹⁶ identified one-dimensional thermoelectric transport in 40 nm diameter InSb NWs grown by a vapour-liquid-solid (VLS) method.¹⁷ However, a low ZT was once again reported; this time due to a small $|S| \approx 30 \mu\text{V/K}$, attributed to unintentional donor impurities (non-optimal E_F). The following year, Hochbaum et al.¹⁸ produced Si NWs by electroless etching—a method yielding much rougher NW surfaces

compared to VLS growth—and measured $ZT \approx 1$ at 300 K. Notably, this was despite a large *decrease* of the power factor ($S^2\sigma$) versus bulk Si, which is a decidedly poor thermoelectric material with $\kappa \approx 150$ W/m-K.¹⁹ Here, ZT enhancement was achieved from a reduction in the thermal conductivity by two orders of magnitude compared to the bulk, owing to increased phonon-boundary scattering at the rough NW surfaces. Three years later, Liu et al.²⁰ measured $ZT = 1.6$ at $T = 700$ K—one of the largest NW values ever reported—in β -Zn₄Sb₃ NWs grown by physical vapour deposition. A very low thermal conductivity was again observed, $\kappa \approx 0.6$ W/m-K, and attributed to phonon scattering at grain boundaries along the NW.

Around the same time, Tian et al.²¹ observed confinement effects on the electrical conductance of 20 nm InAs NWs. Specifically, the conductance was seen to increase stepwise with increasing backgate voltage; each step indicating the filling of a single sub-band. This was only evident up to 40 K, however, where electron scattering mechanisms were quenched in the NWs. A small Seebeck coefficient, $|S| < 10$ μ V/K, was also measured. Subsequent measurements by Schmidt et al.²² yielded σ and S corresponding to a room temperature power factor of 525 μ W/m-K² in their InAs NWs, about one seventh of the power factor reported by Hochbaum et al. (≈ 3500 μ W/m-K²). Most recently, Yazji et al.²³ measured $S^2\sigma \approx 1300$ μ W/m-K² in Se-doped InSb NWs with larger diameters ranging from 150 to 200 nm. However, the figure of merit was once again low at $ZT \approx 0.02$, due to a large bulk-like thermal conductivity near 20 W/m-K in their VLS-grown NWs.

These results are summarized in Table 1.1. A comprehensive review of NW thermoelectric materials can be found in Ref. 24 and a figure summarizing the ZT values therein is included in Appendix I (Figure A1).

Table 1.1: Summary of NW measurements discussed in this section.

nanowire material	diameter [nm]	T [K]	$ S $ [$\mu\text{V/K}$]	σ [S/cm]	κ [W/m-K]	$S^2\sigma$ [$\mu\text{W/m-K}^2$]	ZT	ref.
InAs	60	24	10	5000	-	50	-	25
InAs	90	300	60	14	4	5	0.0003	15
InAs	125	300	50	20	2.6	5	0.0006	26
InAs	30	317	145	250	-	525	-	22
InSb	40	350	30	370	-	32	-	16
InSb	160	300	250	140	20	1300	0.02	23
Si	50	300	245	588	1.5	3500	0.6	18
$\beta\text{-Zn}_4\text{Sb}_3$	125	700	200	330	0.9	1300	1.6	20

The preceding studies indicate that the power factor suffers in NWs due to either excess doping or unwanted electron scattering. Both are somewhat universal symptoms of nanoscale materials, and they serve to nullify or obscure any room temperature quantum effects in real NWs. Indeed, the theoretical ZT enhancement predicted by Dresselhaus et al.^{9,10} remains largely unrealized experimentally. Improving the ideality of NWs in this respect requires significant advances in growth technologies, to allow more precise control over the donor/acceptor concentration and crystal structure. Nonetheless, near term NW TEDs can benefit from a small enough thermal conductivity,

despite exhibiting sub-optimal electronic transport properties. Thus, there is incentive to find means of lowering κ_L which do not severely impact σ .

1.4. Nanowire Thermal Conductivity

The lattice thermal conductivity can be written as²⁷

$$\kappa_L = \int_0^{\omega_{\max}} \mathcal{D} C_v v l_{\text{ph}} d\omega \quad (1.3)$$

with \mathcal{D} representing the phonon density of states, C_v the lattice heat capacity, v the phonon group velocity, and l_{ph} the phonon mean-free-path. The value ω_{\max} represents the highest frequency among vibrational modes in the lattice. Small values of κ_L are measured for NWs universally and orders of magnitude lower values versus the bulk thermal conductivity are common.²⁴ A baseline reduction of the group velocities, v , is expected in NWs due to phonon confinement in the finite structure.²⁸ Additional features, like surface roughness, serve to reduce the phonon mean-free-path, l_{ph} —or to increase the effective scattering rate, $\tau^{-1} = \frac{v}{l_{\text{ph}}}$.

In long and crystalline NWs, κ_L is also suppressed by phonon-boundary scattering, for which the scattering rate,²⁸

$$\tau_B^{-1} = \frac{v}{w} (1 - p) \quad (1.4)$$

depends on the NW width (w) and the specularity parameter, $0 \leq p \leq 1$. Note that τ_B^{-1} lacks any explicit temperature dependence. Indeed, a signature of predominant phonon-boundary scattering is a thermal conductivity that quickly saturates with increasing

temperature.²⁶ Some intuition about p is provided by the Ziman expression²⁹ for the specularity of plane wave scattering at a boundary with root-mean-squared (RMS) roughness η :

$$p(k) = \exp(-4k^2\eta^2 \cos^2 \theta) \quad (1.5)$$

Here, k is the phonon wave vector and θ is the angle of incidence on the boundary. Let us consider normal incidence ($\cos \theta = 1$) for the sake of example. According to Eq. (1.5), fine roughness is ignored by long wavelength (small k) phonons, which scatter with high specularity, corresponding to $p \rightarrow 1$. Conversely, $p \rightarrow 0$ for short wavelength (large k) phonons, which scatter in random directions from the detail of a rough surface. In other words, low specularity means that outgoing phonons are diffused in many directions. In the limit of virtually no roughness ($\eta \rightarrow 0$), boundary scattering is entirely specular and τ_B^{-1} is zero. If the NW is too wide ($w \gg l_{\text{ph}}$), then boundaries are seldom encountered and again τ_B^{-1} is zero. However, phonon-boundary scattering is almost always significant in real NWs.^{15,18,20,26} Boundary scattering and phonon confinement can reduce the thermal conductivity of VLS-grown III-V NWs by up to 80% compared to the bulk.^{30–34} Experiments on rough Si and Si_{1-x}Ge_x NWs have also shown additional thermal conductivity reductions compared to nominally smooth NWs.³⁵ The roughness of radial and axial heterointerfaces can be treated similarly,³⁶ and a core-shell mismatch of the acoustic impedance (*i.e.*, the density and sound velocity) could reduce the thermal conductivity further.³⁷ As well, mass variation³⁸ due to impurities, isotopes,³⁹ or alloying also suppresses the thermal conductivity.

1.5. Phonon Engineering in Nanowires

In a somewhat alternate approach, other studies have examined the possibility of tuning the phonon spectra of nanostructures using *coherent* phonon engineering. Coherence is distinct from specularity and here refers to the phase of scattered phonons,²⁷ although phase-preserving (*i.e.*, elastic) scattering events are correlated with specularity.⁴⁰ Unlike the previous approaches, pristine boundaries and interfaces are in fact preferred, and thermal conductivity reduction can be attributed to the stalling of certain vibrational modes, as determined by the structural periodicity.⁴¹

A planar superlattice TEG was demonstrated by Subramanian et al.,⁴² who measured an impressive room temperature figure of merit, $ZT \approx 2.4$. Cross-plane thermal conductivity measurements by the same authors⁴³ indicated a non-linear dependence on the superlattice period, with a minimum thermal conductivity achieved for a period ~ 50 Å. The carrier mobility exhibited similar behaviour and, unlike the thermal conductivity, varied with the relative thicknesses of superlattice layers. Notably, cross-plane thermal conductivity and mobility minima were attained at different superlattice periods. Regarding the limiting behaviour, the authors observed that small periods ($\ll 50$ Å) reproduced the alloy thermal conductivity, while large periods reproduced the length-weighted average of constituent layers.

To reconcile the coherent (wave-like) picture of phonon transport with diffusive (corpuscular) expressions like Eq. (1.3), the effect of coherent backscattering can be

understood as an increase in the apparent “viscosity” of a diffusive medium.⁴¹ In the frequency domain, the phonon mean-free-path is expressed as⁴³

$$l_{\text{ph}} = \sqrt{\frac{2D}{\omega}} \quad (1.6)$$

using the diffusion coefficient, $D = \frac{1}{3}\bar{v}l_{\text{ph}}$, with \bar{v} being the average group velocity of phonons.⁵ Eq. (1.6) then allows a cut-off frequency to be estimated:

$$\omega_{\text{min}} = \frac{2\bar{v}}{3l_{\text{ph}}} \quad (1.7)$$

In this simple model, phonon transport at frequencies $\omega < \omega_{\text{min}}$ is suppressed, since frequencies lower than ω_{min} require a larger-than- l_{ph} mean-free-path to effectively conduct heat. The mean-free-path, in turn, varies non-linearly with the superlattice period and proportionally with the thermal conductivity. In quasi-one-dimensional NWs, where three-dimensional equipartition is violated (*i.e.*, $D \approx \bar{v}l_{\text{ph}}$), this cut-off frequency could be even higher, leading to an even lower thermal conductivity. While Eq. (1.7) can be used to explain the room temperature results of Subramanian et al.,⁴³ phonon transmission consistent with the Bragg reflection⁵ of narrow frequency bands has been observed at much lower temperature in GaAs/AlAs superlattices.⁴⁴

In terms of heat transport, Si/Ge and related materials represent the most-studied NW superlattices.^{35,45–50} Li et al.⁴⁹ measured the thermal conductivity in Si/Si_{0.9}Ge_{0.1} NWs from 20 K up to room temperature and found that the smooth superlattice NWs had thermal conductivities comparable to the rough Si NWs studied by

Hochbaum et al.^{18,51} However, boundary scattering and alloy scattering (in the $\text{Si}_{0.9}\text{Ge}_{0.1}$ segments) were implicated in the observed thermal conductivity reduction, as opposed to any superlattice (*i.e.*, wave interference) phenomena in the NWs. The authors noted that interfacial sharpness between segments was unlikely, as interfaces would be disturbed by atomic diffusion at the NW growth temperatures.

Computational studies on superlattices, where interfacial sharpness can be guaranteed, have shown a pronounced dependence of the thermal conductivity on the superlattice period.^{27,47,50} Indeed, the same trend as the experimental data of Subramanian et al.⁴³ is reproduced in these studies; namely, a sharp descent to a minimum thermal conductivity, followed by a more gradual rise with increasing superlattice period.

1.6. Tunable Thermal Conductivity

More recently, twinning superlattice (TSL) NWs^{52–56} have attracted attention as periodic structures suitable for phonon engineering. In Si, some III-Vs, and other cubic semiconductors, NWs grown along the $\langle 111 \rangle$ direction can exhibit twinning in the form of abrupt 60° rotations in the crystal structure about the NW axis. When this twinning is periodic, a TSL NW is produced as a stack of complementary A/B twin segments. Unlike heterojunction superlattices, diffusion is a non-issue for TSLs because there is no concentration gradient across the twin boundary. Hence, the principal advantage of TSL NWs is, in this respect, the inherent sharpness of crystal twin interfaces (see, for

example, Ref. 52). These interfaces may be more conducive to coherent phonon scattering and thus provide a means of tuning the phonon spectra of NWs. Additionally, corrugated (111)A/B surface faceting⁵⁷ often accompanies twinning and some theoretical studies have predicted that these surfaces can contribute significantly to phonon backscattering.^{58,59} The formation of microfacets, as opposed to flat ($1\bar{1}0$) sidewalls in “pristine” NWs, may be central to the kinetics of NW TSL formation in general.⁶⁰

Current growth technologies enable some control over the TSL period,⁶⁰ as well as the overall density and randomness of twinning/stacking faults in III-V NWs.^{61,62} Unlike traditional superlattice growth, the length of individual twin segments is not determined by changing precursor fluxes. Rather, the conditions as a whole—the temperature, flux ratios, growth rate, etc.—create a TSL growth regime corresponding to a set NW morphology. In III-V NWs, dopants like Zn, Te, and Be are known to induce TSL growth,^{63,64} but dopant-free TSL NWs have also been reported.^{56,61}

Coherent phonon transport has been identified in GaP TSL NWs at room temperature, by using Raman scattering to probe the optical phonon modes.⁶⁵ A reduced thermal conductivity in *disordered* twinning NWs, where crystal rotations appear to happen randomly, has also been measured.^{26,66} Computational studies on periodic Si TSLs^{67,68} have found minima in the thermal conductivity versus the twin period, as well as overall trends closely resembling experimental results on traditional superlattices.⁴³

In general, neither the electronic nor phononic band structure of the parent material is invariant under the crystal rotations that characterize twinning, so the twin interface is in many ways analogous to an interface of different materials. For example, electronic minibands in TSLs could allow for direct transitions in normally indirect band gap semiconductors.^{69,70} The phonon spectra of periodic TSLs are also distinct,^{67,71} owing to a much larger unit cell (comprising one twin period) and additional symmetries afforded by the twinning structure.⁶⁵

1.7. Thesis Overview

With the possible exception of InSb, which can have a very high electron mobility,⁷² III-V semiconductors are far from ideal thermoelectric compounds.⁷³ However, the ubiquity of III-Vs, which is spurred by their technological importance, guarantees mature tools for the synthesis, characterization, and modelling of these materials. While there is still room for improvement, quality macroscopic arrays of GaAs NWs (1 to 4 mm² area) are readily grown using selective-area epitaxy and VLS methods. Dopant incorporation and crystal twinning are also increasingly well understood in these NWs, precisely because they are easier to synthesize. Thus, GaAs is a reasonable candidate for NW thermoelectrics research.

Using transport calculations, experiments, and simulations on GaAs NWs, we aim to draw conclusions that are more broadly relevant to III-Vs and perhaps NW

thermoelectrics in general. These investigations comprise the next three chapters of the thesis.

Chapter 2 provides a comprehensive review of the physical models underlying electronic transport calculations for select III-Vs, based on the Boltzmann Transport Equation.⁷⁴ Chapter 3 introduces, for the first time, experimental thermal conductivity measurements on as-grown arrays of polytypic versus TSL GaAs NWs, using a NW-composite device adapted to the 3ω method.^{75,76} Chapter 4 explores thermal conductivity and phonon transmission in a variety of GaAs NW structures, using non-equilibrium molecular dynamics simulations⁷⁷ and the atomistic Green's function method,^{78,79} respectively. In Chapter 5, we investigate the growth conditions leading to TSL formation in GaAs NW arrays and determine a phase diagram to inform future growths of high-yield TSL NW arrays. Finally, Chapter 6 provides concluding remarks and a discussion of future work in NW thermoelectrics.

2. Boltzmann Transport Model

2.1. Summary

This chapter begins by developing a first principles understanding of thermoelectric phenomena, as originally observed via the Seebeck, Peltier, and Thomson effects in the nineteenth century. Subsequent sections introduce the relevant physics of bulk and nanoscale semiconductors, as well as a transport formalism based on Onsager's reciprocal relations⁸⁰ and the Boltzmann Transport Equation.⁸¹ Together with a description of scattering via the various prevailing mechanisms, this culminates in models for the thermoelectric transport coefficients S (Seebeck coefficient), σ (electrical conductivity), and κ_e (electronic thermal conductivity) of bulk and NW semiconductors. Using these models, we calculate transport coefficients for GaAs, InAs, InP and InSb, and determine the thermoelectric figure of merit, ZT , where we find an enhancement by two orders of magnitude for the small NW case compared to the bulk. The optimal electron concentration, *vis a vis* the thermoelectric efficiency, is determined as a function of diameter for both background and modulation doped NWs.

The contents of this chapter are based on our publication⁸² in *Nanotechnology*, "Modelling thermoelectric transport in III-V NWs using a Boltzmann transport approach: a review". Here, we aim to provide a comprehensive and unified description of the physics underlying thermoelectric phenomena. Derivations, solution methods, and complete sets of material parameters are provided to aid future implementations.

2.2. Introduction

It has been known since the early nineteenth century^{83,84} that the transport of heat and electrical energy can be coupled directly, without intermediate mechanical processes involving turbines or compressors. Direct conversion of this sort forms the operating principle of thermoelectric devices (TEDs), wherein the “working fluid” is the Fermi gas of charge carriers (electrons and/or holes) in a solid-state material. This allows TEDs to be silent, compact, and virtually maintenance free. Despite these advantages, however, TEDs remain less efficient and often more expensive than their mechanical analogues. Nonetheless, they are extremely useful for both power generation and refrigeration in a variety of systems. For example, when coupled with simple control circuitry, thermoelectric coolers (TECs) provide a means of precise temperature control for cooling laser diodes.⁸⁵ Thermoelectric generators (TEGs) with a radioisotope heat source^{86,87} have been used by NASA as the main power system for a number of rovers and space probes⁸—owing partly to the reliability of TEGs as compared to photovoltaics in dusty or low-light conditions.

Hicks and Dresselhaus^{9,10} were first to identify potential improvements in nanoscale thermoelectrics due to beneficial changes in the electronic properties of carrier-confined systems. Further efficiency improvements through the reduction of thermal conductivity (by various mechanisms) have also been predicted^{28,37,88} and demonstrated experimentally.^{18,36,49}

In this chapter we discuss models for the electronic thermoelectric properties of both bulk and NW materials. We shall concentrate, in particular, on III-V NWs that can be grown by the self-assisted vapour-liquid-solid (SA-VLS) method.^{17,89}

2.3. Thermoelectric Effects

2.3.1. *The Seebeck Effect*

The Seebeck effect creates an electrical potential difference, given a difference in temperature. This effect forms the basis for thermoelectric generators (TEGs), as the resulting voltage can be used to drive a current. The Seebeck effect can also be described as the conversion of a temperature difference to an electric current.⁹⁰ The Seebeck *coefficient*, S , is defined as the ratio of the open circuit voltage to the applied temperature difference:

$$S \equiv \frac{\Delta V_{oc}}{T_h - T_c} \quad (2.1)$$

The linear dependence of ΔV_{oc} on $\Delta T = T_h - T_c$ was observed experimentally long before the discovery of the electron.⁸³ In the modern understanding of the Seebeck effect, it is caused by a difference in electron distributions between the hot and cold sides of a conductor. Figure 2.1 illustrates a simple thermoelectric circuit, where an ideal connection is made to an n-type conductor by hot and cold metal contacts, which remain at constant temperatures. The electron distributions at the hot and cold sides

are given by $f_0(E, E_F, T_h)$ and $f_0(E, E_F, T_c)$, respectively, where f_0 is the Fermi-Dirac distribution:

$$f_0(E, E_F, T) = \frac{1}{\exp\left(\frac{E - E_F}{k_B T}\right) + 1} \quad (2.2)$$

The function f_0 indicates the equilibrium occupation probability of an electron state with energy E . The Fermi energy, E_F , is the energy corresponding to an occupation probability of exactly 50%, while the temperature (T) determines the sharpness of the transition in probability from 1 to 0 across E_F .

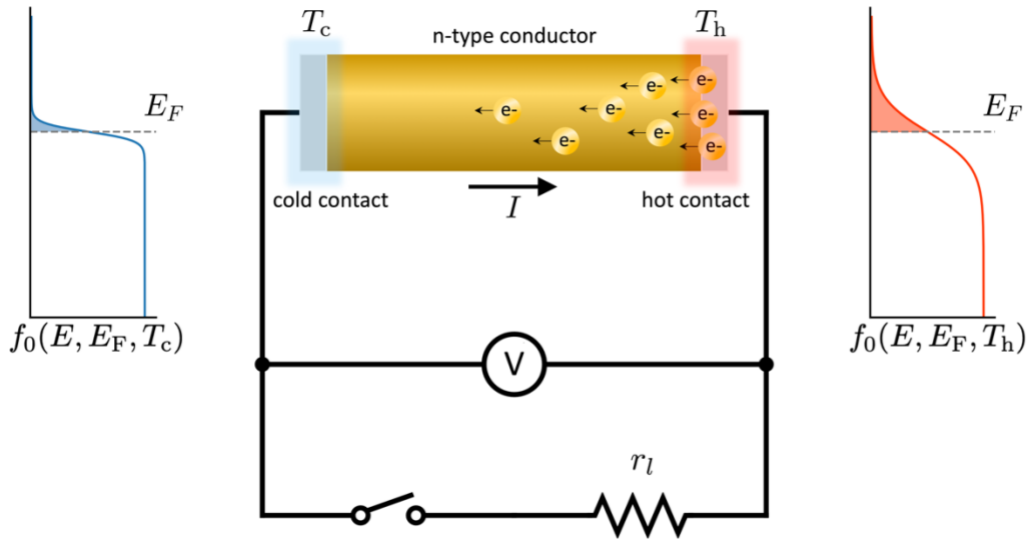


Figure 2.1: A thermoelectric circuit illustrating the origin of the Seebeck effect. The larger area under the red distribution plot indicates an excess of free electrons on the hot side. Potential energy is stored in the electron concentration gradient and is measured per unit charge as $\Delta V_{oc} = S(T_h - T_c)$. The current in the circuit, I , only appears once the switch is closed.

The red and blue shaded areas under the two f_0 plots in Figure 2.1 illustrate a relative excess of free electrons on the hot side. While the switch in the circuit remains

open, internal currents will flow to equalize the hot and cold side distributions. For simplicity, we assume that current is carried by electrons at a single energy E_J in the n-type conductor—*i.e.* that Figure 2.1 illustrates a single-channel device.⁹¹ Such a device can be realized in quantum dots,⁹² for example. To equalize the distributions at energy E_J , we will eventually have:

$$\frac{E_J - E_F^h}{T_h} = \frac{E_J - E_F^c}{T_c} \approx \frac{E_J - E_F}{T} \quad (2.3)$$

provided that the temperature difference is small. The quantity in Eq. (2.3) indicates the available electron energy per unit temperature in the n-type conductor. Thus, dividing by the charge of an electron, we find the voltage difference per unit temperature difference generated in the device:

$$S = -\frac{1}{eT}(E_J - E_F) \quad (2.4)$$

If electrons flow at energy $k_B T$ above the Fermi energy, then $S = -k_B/e$, which is approximately $-100 \mu\text{V/K}$. Indeed, the Seebeck coefficient of viable thermoelectric materials is typically of the same order of magnitude. For materials with energy *bands*, unlike the single channel device, E_J must be calculated as an average over the electron distribution.

The voltmeter in Figure 2.1 will read $\Delta V_{oc} = S\Delta T$ while the switch remains open and no current flows in the circuit. Once the switch is closed, the (conventional) current will flow in the indicated direction. In this example, transport within the thermoelectric element is ballistic, meaning electrons do not exchange energy inside the n-type

conductor. Conversely, if any scattering takes place, then the voltage reading will be reduced by a factor

$$\frac{\Delta V}{\Delta V_{oc}} = \frac{r_l}{r + r_l} \quad (2.5)$$

when current flows, with r being the resistance of the thermoelectric element. Thus, it is necessary to have both a large Seebeck coefficient and a large electrical conductivity ($\sigma = L/rA$) to maximize the power delivered to the load. This is an important requirement for optimizing the electronic properties of a candidate material.

Note that the Seebeck contribution of the hot and cold contacts (and indeed the remainder of the circuit) in Figure 2.1 was ignored. This can be justified as follows. First, most pure metals have Seebeck coefficients on the order of 1 to 10 $\mu\text{V/K}$,⁴ at least an order of magnitude smaller than our estimate via Eq. (2.4). This limits the Seebeck voltage across the contacts. Second, if the metal contacts are thin (as is often the case), the temperature difference across them, and hence the proportional Seebeck voltage, will be very small. In general, the open circuit voltage across a series combination of elements is

$$\Delta V_{oc} = \sum_i S_i \Delta T_i \quad (2.6)$$

where ΔT_i is the temperature difference across element i and S_i is its Seebeck coefficient.

2.3.2. The Peltier Effect

The Peltier effect⁸⁴ is the principle of operation for thermoelectric coolers (TECs) and was discovered shortly after the Seebeck effect. The Peltier coefficient, Π , relates the charge current flowing through a junction of dissimilar conductors to the heat current through the same junction:

$$I_Q = \Pi I \quad (2.7)$$

Here, I_Q is the Peltier heat current in Watts. Eq. (2.7) states that there is a proportional transport of thermal energy accompanying the flow of electrons (and/or holes).

The single-channel device is shown again in Figure 2.2, this time illustrating the Peltier effect under an applied voltage. To maintain current continuity, electrons with sufficient thermal energy are transmitted through the n-type conductor at energy E_J . The left contact then cools as thermal equilibrium is re-established. On the opposite side, hot electrons (arriving with energy E_J) rapidly thermalize, transferring the excess energy to the right contact, which heats up. Reversing the polarity of the applied voltage will, conversely, cool the right contact and heat the left.

Each electron transports approximately $E_Q = E_J - E_F$ thermal energy between the contacts. Accordingly, the heat transported per unit charge is the Peltier coefficient:

$$\Pi = -\frac{1}{e}(E_J - E_F) \quad (2.8)$$

Note that Eq. (2.8) together with Eq. (2.4) implies

$$\Pi = TS \quad (2.9)$$

for the single-channel conductor. This relationship holds generally and was first observed by Sir William Thomson (Lord Kelvin) in the mid-nineteenth century. Eq. (2.9) is sometimes given as the definition of the Peltier coefficient. Indeed, as we shall momentarily, the S is in a sense the only fundamental thermoelectric parameter.

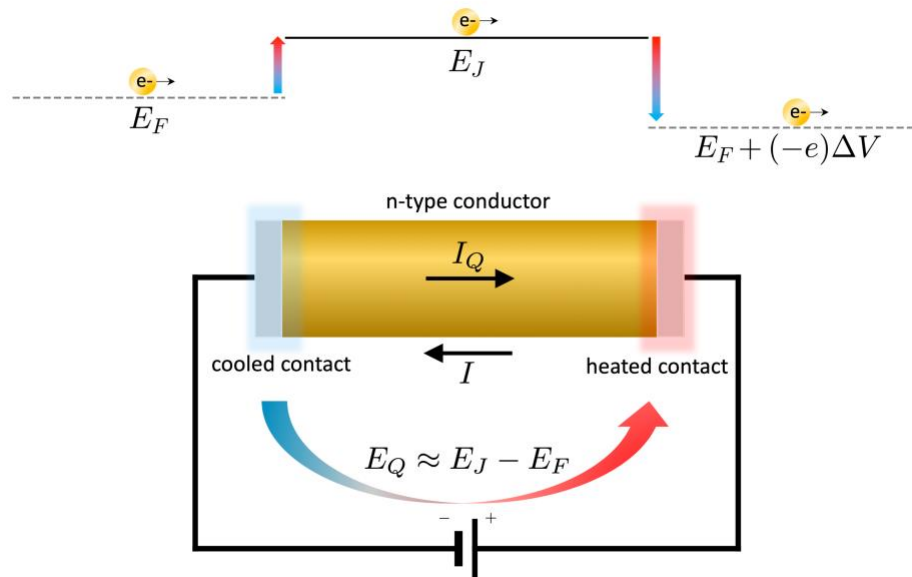


Figure 2.2: A thermoelectric circuit illustrating the origin of the Peltier effect. Electrons absorb or expel energy as they traverse the discontinuous energy levels across different materials, leading to local cooling or heating of the surroundings.

2.3.3. The Thomson Effect

Lastly, the Thomson effect is the change in heat content that occurs when an electric current travels through a temperature gradient in the volume of a conductor. This change can lead to both heating and cooling, depending on the relative directions of the temperature gradient and electric current. The Thomson coefficient is given by⁹³

$$\tau = T \frac{dS}{dT} \quad (2.10)$$

Together, Eq. (2.9) and (2.10) comprise what are known as the “Kelvin relations”, expressing Π and ϵ in terms of S and T .

For a more complete understanding of the Thomson effect, we consider the flow of both charge and heat as processes driven by gradients in the electrochemical potential and temperature of the system. The total charge (J) and heat (Q) current densities through conductor can be expressed in terms of the two driving forces as⁸⁰

$$J = \sigma \left(-\frac{d\psi}{dx} \right) - \sigma S \frac{dT}{dx} \quad (2.11)$$

$$Q = \sigma \Pi \left(-\frac{d\psi}{dx} \right) - (\kappa_e + \sigma S \Pi) \frac{dT}{dx} \quad (2.12)$$

Here, $\psi = V + E_F/(-e)$ is the electrochemical potential (in an n-type conductor) and V is an applied voltage. Eliminating the gradient of ψ from (2.12), we find

$$Q = \Pi J - \kappa_e \frac{dT}{dx} \quad (2.13)$$

The energy flux is then obtained from the charge and heat currents:

$$J_E = J\psi + Q \quad (2.14)$$

Using the continuity equation in one dimension, the change in the total energy density is

$$\frac{\partial \rho_E}{\partial t} + \frac{dJ_E}{dx} = 0 \quad (2.15)$$

and, because the electric current density is uniform, we get

$$\frac{\partial \rho_E}{\partial t} = -\frac{dQ}{dx} - J \frac{d\psi}{dx} \quad (2.16)$$

Then, using Eqs. (2.9), (2.11) and (2.13) to expand the above, we identify three independent mechanisms affecting the volumetric energy change in the current-carrying conductor:

$$\frac{\partial \rho_E}{\partial t} = \frac{J^2}{\sigma} + \frac{d}{dx} \left[\kappa_e \frac{dT}{dx} \right] + J \left[S \frac{dT}{dx} - \frac{d}{dx} (TS) \right] \quad (2.17)$$

On the right-hand side of Eq. (2.17), the first term is the resistive Joule heat, which increases the heat content regardless of the sign (direction) of J . The second term is independent of the electric current and represents simple heat conduction within the electron gas. The final term, being linear in J , represents the reversible change in volumetric heat content due to thermoelectric phenomena—this term quantifies the Thomson effect. Upon expanding the rightmost x derivative, we find the thermoelectric contribution:

$$\left(\frac{\partial \rho_E}{\partial t} \right)_{\text{TE}} = -J \left(T \frac{dS}{dx} \right) \quad (2.18)$$

In a homogeneous conductor, the spatial gradient of the Seebeck coefficient is due to the spatial temperature gradient: $\frac{dS}{dx} = \frac{dS}{dT} \frac{dT}{dx}$. Hence, with Eq. (2.10):

$$\left(\frac{\partial \rho_E}{\partial t} \right)_{\text{TE}} = -J \frac{dT}{dx} \tau \quad (2.19)$$

An interpretation of the Thomson coefficient follows from Eq. (2.19) as the rate of change of the volumetric heat content, per unit temperature gradient, per unit current density.

2.4. The Figure of Merit

The efficiency of a thermoelectric generator, $\eta_{TEG} \equiv P_{out}/Q_h$, is defined as the ratio of electrical power output (P_{out}) to the rate of heat supplied to the hot junction (Q_h). Similarly, the coefficient of performance (COP) of a thermoelectric cooler, $\phi_{TEC} \equiv Q_c/P_{in}$, is the rate of heat drawn from the cold junction (Q_c) divided by the rate of electrical energy expenditure (P_{in}). Equations for these quantities are usually defined by assuming a lack of parasitic heat conduction, while also neglecting resistances outside the thermoelectric element. The reader is referred to Ref. 3 for derivations of the formulae in the following discussion.

For a unipolar thermoelectric device, the efficiency and COP are given by

$$\eta_{TEG} = \left(1 - \frac{T_c}{T_h}\right) \times \frac{\sqrt{1 + Z\bar{T}} - 1}{\sqrt{1 + Z\bar{T}} - \frac{T_c}{T_h}} \quad (2.20)$$

$$\phi_{TEC} = \frac{SIT_c - \frac{1}{2}I^2r - K(T_h - T_c)}{SI(T_h - T_c) + I^2r} \quad (2.21)$$

where \bar{T} is the average temperature between the hot and cold sides of the device. The quantities $r = L/\sigma A$ and $K = \kappa A/L$ are the electrical resistance and thermal conductance of the thermoelectric element, respectively, where A is the cross-sectional area and L is the length. The quantity Z is defined as

$$Z = \frac{S^2}{rK} \quad (2.22)$$

As with any heat engine, the efficiency of the TEG is limited by the Carnot efficiency,

$$\eta_{TEG} \leq \frac{T_h - T_c}{T_h} \quad (2.23)$$

and the maximum coefficient of performance is limited by

$$\phi_{TEC} \leq \frac{T_c}{T_h - T_c} \times \frac{\sqrt{1 + Z\bar{T}} - \frac{T_h}{T_c}}{\sqrt{1 + Z\bar{T}} + 1} \quad (2.24)$$

Both η_{TEG} and ϕ_{TEC} are monotonic functions of ZT , so it suffices to compare candidate materials based on ZT alone.

For physical intuition, Z can be related to an easily measured quantity, the maximum of $(T_h - T_c)$. Considering the rate of cooling,

$$Q_c = SIT_c - \frac{1}{2}I^2r - K(T_h - T_c) \quad (2.25)$$

it is straightforward to see that Q_c , as function of I , attains a maximum value of

$$(Q_c)_{\max} = \frac{S^2T_c^2}{2r} - K(T_h - T_c) \quad (2.26)$$

at current

$$I = \frac{ST_c}{r} \quad (2.27)$$

The maximum temperature difference, $(T_h - T_c)_{\max}$, is such that parasitic heat conduction at the rate $K(T_h - T_c)_{\max}$ exactly matches the rate of heat removal via the Peltier effect. Accordingly, by setting $(Q_c)_{\max} = 0$, we find that:

$$Z = \frac{2(T_h - T_c)_{\max}}{T_c^2} \quad (2.28)$$

It is common practice to instead quote the *dimensionless* figure of merit as

$$ZT = \frac{S^2 \sigma T}{\kappa_e + \kappa_L} \quad (2.29)$$

The quantities S , σ , and κ_e depend on the electronic band structure and the nature of electron scattering in the conductor. These considerations form central aspects of the transport models developed in subsequent sections.

2.5. Electronic Band Structure

The conduction band is isotropic in direct band gap III-V semiconductors, meaning that the electron energy varies only with the magnitude of the electron wave vector, \mathbf{k} . Equivalently, a single electron effective mass (m^*) describes the conduction band minimum to a good approximation.⁹⁴ Assuming parabolic energy bands, this leads to the dispersion relation of the bulk,

$$E(\mathbf{k}) = \frac{\hbar^2 |\mathbf{k}|^2}{2m^*} \quad (2.30)$$

where the energy varies with $|\mathbf{k}|$ like that of a free particle, except with the electron mass “adjusted” in the presence of ion cores in a crystal lattice. Several technologically important III-Vs exhibit non-parabolicity at low energies, and are better described by a dispersion of the form^{95,96}

$$E(\mathbf{k}) = \frac{\hbar^2 |\mathbf{k}|^2}{2m_e} + \frac{1}{2} [\alpha(\mathbf{k}) - 1] E_g \quad (2.31)$$

where m_e is the free electron mass, E_g is the band gap, and $\alpha(\mathbf{k})$ is given by

$$\alpha(\mathbf{k}) = \sqrt{1 + \frac{2\hbar^2|\mathbf{k}|^2}{m_e} \left(\frac{m_e - m^*}{m^*E_g} \right)} \quad (2.32)$$

We shall use Eqs. (2.31) and (2.32) to describe the band structure of bulk materials.

The distinguishing characteristic of carrier-confined systems is that electrons (and holes) do not propagate freely in one or more directions. There is, accordingly, a component to the electron energy that depends on the size of the system in the dimension of confinement. If an electron is confined in all three dimensions, the available energies will be wholly discrete. However, if there is at least one physically large dimension, the energy states will comprise continuous sub-bands offset by the eigenvalues that describe the confined part of the wave function.

We approximate the NW as a cylinder with radius R . The Schrödinger equation for a potential $V(\rho, \phi) = 0$ for $\rho \leq R$ and $V = \infty$ for $\rho > R$ is a separable partial differential equation that can be solved analytically.⁹⁷ This leads to energy eigenvalues

$$E_{l,u} = \frac{\hbar^2 k_{l,u}^2}{2m^*} \quad (2.33)$$

where $k_{l,u} = w_{l,u}/R$ and $w_{l,u}$ is the u^{th} (positive) root of the ordinary Bessel function⁹⁸ $J_l(x)$ of order l . Together, l and u serve as quantum numbers describing solutions to the angular and radial parts of the wave function, respectively. The energy dispersion for the j^{th} sub-band is found by adding the axial contribution:

$$E_j(k_x) = E_{l,u}^{(j)} + \frac{\hbar^2 k_x^2}{2m^*} \quad (2.34)$$

taking \hat{x} along the NW axis. The five lowest sub-bands ($j = 1$ to 5) in a cylindrical quantum wire correspond to quantum numbers $(l, u) = (0, 1), (1, 1), (2, 1), (0, 2),$ and $(3, 1),$ respectively.

The bulk electronic density of states (eDOS) as a function of energy, is given by

$$\rho^{3D}(E) = \frac{\mathcal{N}}{2\pi^2} \left(\frac{2m^*}{\hbar^2} \right)^{\frac{3}{2}} \sqrt{E} \quad (2.35)$$

with the conduction band minimum taken as $E = 0$. The valley degeneracy, \mathcal{N} , is unity if the minimum is at the Γ point of the 1st Brillouin zone ($\mathbf{k} = 0$), as is the case for direct band gap III-Vs. For the one-dimensional case, the density of states in the j^{th} sub-band is

$$\rho_j^{1D}(E) = \frac{1}{\pi R^2} \times \frac{\mathcal{N}}{\pi} \left(\frac{2m^*}{\hbar^2} \right)^{\frac{1}{2}} \frac{1}{\sqrt{E - E_{l,u}^{(j)}}} \quad (2.36)$$

defined for $E \geq E_{l,u}^{(j)}$. Here, division by a factor of πR^2 adjusts the expression to three-dimensional units.

In general, for any given band or sub-band, the equilibrium carrier concentration is

$$n = \int_{E_0}^{\infty} \rho(E) f_0(E, E_F, T) dE \quad (2.37)$$

Note that n corresponds uniquely to an E_F . In the one-dimensional case, n is the sum over n_j using the eDOS ρ_j^{1D} .

Both the concentration and the energy distribution of charge carriers have strong effects on the thermoelectric transport coefficients. To see this, however, we must first introduce the physics of near-equilibrium transport.

2.6. Transport Formalism

From Eqs. (2.9), (2.11) and (2.12), the electronic and heat current densities can be expressed in terms of S , σ , and κ_e alone:

$$J = \sigma F - \sigma S \frac{dT}{dx} \quad (2.38)$$

$$Q = \sigma S T F - (\kappa_e + \sigma S^2 T) \frac{dT}{dx} \quad (2.39)$$

Here, the gradient of the electrochemical potential, $-d\psi/dx$, makes up the total electric field,

$$F = \varepsilon + \frac{1}{e} \frac{\partial E_F}{\partial x} \quad (2.40)$$

where $\varepsilon = -dV/dx$ and $e > 0$ is the fundamental charge. The remaining (non-electronic) transport coefficient, κ_L , describes heat conduction through the atomic lattice:

$$Q_l = -\kappa_L \frac{dT}{dx} \quad (2.41)$$

Eqs. (2.38) to (2.41) can be used to determine the thermoelectric transport coefficients, provided that the current densities J and Q can be calculated

independently. This can be done by solving for the non-equilibrium electron distribution via the Boltzmann Transport Equation (BTE):

$$\frac{\partial f}{\partial t} = \left(\frac{\partial f}{\partial t}\right)_{\text{force}} + \left(\frac{\partial f}{\partial t}\right)_{\text{diff}} + \left(\frac{\partial f}{\partial t}\right)_{\text{scatt}} \quad (2.42)$$

Here, the subscripts “diff” and “scatt” represent “diffusion” and “scattering”, respectively. The BTE is an equation for the distribution function, f , which in general depends on position, velocity, and time. We shall make use of it here with several standard assumptions which greatly simplify the problem of finding f ; firstly, by looking for solutions of the form

$$f = f_0 + g \quad (2.43)$$

with g that is *linear* in the (small) applied field and temperature gradient. Given isotropy of the conduction band, it suffices to discuss scalar quantities related to $k = |\mathbf{k}|$. The individual terms in Eq. (2.42) are then expanded as follows.*

First, the “force” term that motivates electron drift is written as

$$\left(\frac{\partial f}{\partial t}\right)_{\text{force}} = -\frac{dk}{dt} \frac{\partial f}{\partial k} \quad (2.44)$$

where the net force, $F \equiv dp/dt$, is the Coulomb force $F = (-e)\varepsilon$ in an electric field ε . Taking $p = \hbar k$ allows the force term to be rewritten in terms of the applied field. Using Eq. (2.43), this is

$$\left(\frac{\partial f}{\partial t}\right)_{\text{force}} = \frac{e\varepsilon}{\hbar} \frac{\partial}{\partial k} (f_0 + g) \quad (2.45)$$

Since g is proportional to ε , the force term is truncated to

* as per the usual derivation of the linearized electron BTE⁹⁹

$$\left(\frac{\partial f}{\partial t}\right)_{\text{force}} = \frac{e\varepsilon}{\hbar} \frac{\partial f_0}{\partial k} \quad (2.46)$$

in the linear approximation.

Next, the "diffusion" term is written as

$$\left(\frac{\partial f}{\partial t}\right)_{\text{diff}} = -v(k) \frac{\partial f}{\partial x} \quad (2.47)$$

The spatial gradient of the distribution is due to the gradients of E_F and the temperature:

$$\frac{\partial f}{\partial x} = \frac{\partial f}{\partial E_F} \frac{\partial E_F}{\partial x} + \frac{\partial f}{\partial T} \frac{dT}{dx} \quad (2.48)$$

Moreover, from the definition of f_0 (Eq. (2.2)), it is easy to see the following equivalencies:

$$\frac{\partial f_0}{\partial E_F} = \left(\frac{T}{E - E_F}\right) \frac{\partial f_0}{\partial T} = -\frac{1}{\hbar v(k)} \frac{\partial f_0}{\partial k} \quad (2.49)$$

with

$$v(k) = \frac{1}{\hbar} \frac{\partial E}{\partial k} \quad (2.50)$$

Therefore, from Eqs. (2.47) to (2.50), the diffusion term is

$$\left(\frac{\partial f}{\partial t}\right)_{\text{diff}} = \frac{1}{\hbar} \frac{\partial f_0}{\partial k} \left[\frac{\partial E_F}{\partial x} + \left(\frac{E - E_F}{T}\right) \frac{dT}{dx} \right] \quad (2.51)$$

with another truncation, this time to obtain a linear result with respect to the temperature gradient.

Finally, if the field and/or temperature gradient are steady and uniform, it is assumed that the distribution does not otherwise evolve over time, so the partial time derivative in the BTE (Eq. (2.42)) is eliminated. Altogether, the linearized BTE is

$$\left(\frac{\partial f}{\partial t}\right)_{\text{scatt}} = -\frac{1}{\hbar} \frac{\partial f_0}{\partial k} \left\{ e\varepsilon + \frac{\partial E_F}{\partial x} + \left(\frac{E - E_F}{T}\right) \frac{dT}{dx} \right\} \quad (2.52)$$

To determine the current densities J and Q from f , we consider the particle flux through an arbitrary surface with normal vector $\hat{\mathbf{n}}$:

$$j_{\hat{\mathbf{n}}} = \int (\mathbf{v} \cdot \hat{\mathbf{n}}) \rho_{\mathbf{k}} f(\mathbf{r}, \mathbf{k}, t) d\mathbf{k} \quad (2.53)$$

where $\rho_{\mathbf{k}}$ is the density of states and $\mathbf{v}(\mathbf{k})$ is the group velocity:

$$\rho_{\mathbf{k}} = \begin{cases} \frac{1}{4\pi^3} & (3\text{D}) \\ \left(\frac{1}{\pi R^2}\right) \frac{1}{\pi} & (1\text{D}) \end{cases} \quad (2.54)$$

$$\mathbf{v}(\mathbf{k}) = \frac{1}{\hbar} \nabla_{\mathbf{k}} E \quad (2.55)$$

Here, $\rho_{\mathbf{k}}$ is the number of electron states per unit real-space volume, per unit \mathbf{k} -space volume; with the former, but not the latter, always being three-dimensional. Hence, the particle current is obtained as a flux per unit area in both the bulk and one-dimensional (NW) case using Eqs. (2.53) to (2.55). This allows for a direct comparison of the transport coefficients which we shall later obtain.

Given the particle current, prescribing a unit charge (e) or unit thermal energy ($E - E_F$) gives the electric and heat currents:

$$J = -e \int \rho_{\mathbf{k}} v(\mathbf{k}) f(\mathbf{r}, \mathbf{k}, t) d\mathbf{k} \quad (2.56)$$

$$Q = \int [E(\mathbf{k}) - E_F] \rho_{\mathbf{k}} v(\mathbf{k}) f(\mathbf{r}, \mathbf{k}, t) d\mathbf{k} \quad (2.57)$$

2.7. The Relaxation Time Approximation

Solutions to the linearized BTE (Eq. (2.42)) can be obtained immediately by positing that

$$\left(\frac{\partial f}{\partial t}\right)_{\text{scatt}} = -\frac{f(k, t) - f_0(k)}{\tau(k)} \quad (2.58)$$

Eq. (2.58) asserts that scattering events relax the non-equilibrium distribution over a characteristic time $\tau(k)$, which represents the average time between scattering events.⁷⁴ This is the aptly named “relaxation time approximation” (RTA). We note that Eq. (2.58) is a separable differential equation describing the exponential decay of the solution, f . With Eq. (2.43), the solution of Eq. (2.58) is of the form

$$f(k, t) = f_0(k) + g(k, 0) \times \exp[-t/\tau(k)] \quad (2.59)$$

The relaxation time, $\tau(k)$, must be independent of the distribution itself for this to be possible. Substituting Eq. (2.58) into Eq. (2.52) yields the solution of the BTE within the RTA:

$$f(k) = f_0(k) + \frac{\tau(k)}{\hbar} \frac{\partial f_0}{\partial k} \left\{ e\varepsilon + \frac{\partial E_F}{\partial x} + \left(\frac{E - E_F}{T} \right) \frac{dT}{dx} \right\} \quad (2.60)$$

In III-V semiconductors, defining a $\tau(k)$ is complicated by the strong presence of electron scattering by polar-optical (PO) phonons.⁷⁴ Unlike scattering by ionized

impurities, for example, PO phonon scattering involves the absorption or emission of a new particle (a phonon of frequency ω_{po}), and a corresponding (significant) change in the electron energy. This means that the PO scattering rate is in fact dependent upon the electron distribution.⁸¹ The RTA is therefore not a strictly valid approach for obtaining electron distributions in III-Vs. It is, however, possible to define a “quasi-relaxation time” for PO scattering¹⁰⁰ in one- or two-dimensional conductors, using an approach which is known to be accurate for two-dimensional systems.¹⁰¹ The total relaxation time can then be obtained using Matthiessen’s rule,

$$\frac{1}{\tau(k)} = \sum_i \frac{1}{\tau_{(i)}(k)} \quad (2.61)$$

where $i = \text{“PO”}, \text{“AC”}, \text{“PE”}, \text{and “II”}$ represents the four major scattering mechanisms in extrinsic III-V semiconductors:¹⁰² polar-optical phonon scattering, acoustic deformation potential scattering, piezoelectric scattering, and ionized impurity scattering, respectively.

In some applications of the RTA (for example, Refs. 11 and 22), the total relaxation time is assumed to be of the form

$$\tau(E) = \tau_0 \left(\frac{E}{k_B T} \right)^s \quad (2.62)$$

where s characterizes the energy (or k) dependence of the dominant scattering mechanism.^{11,74} While this leads to more simple expressions for S , σ , and κ_e , it also introduces an adjustable parameter, τ_0 , which affects the values of the mobility-related transport coefficients, σ and κ_e . To avoid this, we shall use expressions for $\tau_{(i)}$ found in

literature—based on well-known material parameters—then calculate the total relaxation time explicitly from Eq. (2.61), as described below, instead of using Eq. (2.62).

2.8. Nanowire Transport Coefficients

The relaxation rates for PO, AC and PE scattering in a cylindrical quantum wire are taken from Fishman.¹⁰⁰ For PO scattering, it is assumed that the longitudinal optical branch of the phonon dispersion is flat, such that the polar optical phonon energy is uniformly $E_{\text{po}} = \hbar\omega_{\text{po}}$. The PO scattering relaxation rate is then approximated by

$$\frac{1}{\tau_{\text{po}}(k)} = \frac{e^2 m^* E_{\text{po}}}{2\pi^2 \hbar^3} \left(\frac{1}{\epsilon_\infty} - \frac{1}{\epsilon_s} \right) \left\{ \frac{N_{\text{po}} [1 - 2I_1(x_q^+) K_1(x_q^+)]}{x_q^+ \sqrt{k^2 + q_0^2}} \right. \\ \left. + \frac{(N_{\text{po}} + 1) [1 - 2I_1(x_q^-) K_1(x_q^-)]}{x_q^- \sqrt{k^2 - q_0^2}} \Theta(E_j(k) - E_{l,u}^{(j)} - E_{\text{po}}) \right\} \quad (2.63)$$

where $k = k_x$ is the magnitude of the wave vector along the NW axis. $E_j(k)$ is given by Eq. (2.34) for the sub-band dispersion, and the expressions

$$q_0^2 \equiv \frac{2m^* E_{\text{po}}}{\hbar^2} \quad (2.64)$$

$$x_q^\pm \equiv R \left(k + \sqrt{k^2 \pm q_0^2} \right) \quad (2.65)$$

are used to simplify the notation. The quantities ϵ_s and ϵ_∞ in Eq. (2.63) are the low and high frequency dielectric permittivities, respectively. N_{po} is the occupation number of polar-optical phonons in thermal equilibrium, from Bose-Einstein statistics:

$$N_{\text{po}} = \frac{1}{\exp\left(\frac{E_{\text{po}}}{k_B T}\right) - 1} \quad (2.66)$$

$\Theta(E)$ is the Heaviside step function, which in Eq. (2.63) excludes phonon emission when the electron energy is less than E_{po} . The functions $I_\nu(x)$ and $K_\nu(x)$ are modified Bessel functions of the first and second kind,⁹⁸ respectively, both of order ν .

The AC scattering relaxation rate is given by

$$\frac{1}{\tau_{\text{ac}}(k)} = \frac{2m^* E_{\text{ac}}^2 k_B T}{\pi R^2 \hbar^3 c_l k} \quad (2.67)$$

where E_{ac} is the acoustic deformation potential and c_l is the longitudinal elastic constant.

For piezoelectric scattering, the relaxation rate is:

$$\frac{1}{\tau_{\text{pe}}(k)} = \frac{2m^* e^2 \mathcal{P}^2 k_B T}{\pi \hbar^3 \epsilon_s k} \left[\frac{1 - 2I_1(x_k)K_1(x_k)}{x_k^2} \right] \quad (2.68)$$

with $x_k = 2kR$ and \mathcal{P} , the (dimensionless) piezoelectric coefficient.

Finally, for scattering by background ionized impurities, the relaxation rate is¹⁰³

$$\frac{1}{\tau_{\text{ii}}(k)} = \frac{e^4 m^* N_I}{2\pi \hbar^3 \epsilon_s^2 k^3} \left\{ \frac{2K_1(x_k)I_0(x_k)}{x_k} - \frac{4K_1(x_k)I_1(x_k)}{x_k^2} \right. \\ \left. - I_1^2(x_k)[K_1^2(x_k) - K_0^2(x_k)] \right\} \quad (2.69)$$

where N_I is the density of ionized impurities. The II scattering rate is reduced if the impurities are remote (for example, with modulation doping). For remote impurities, the scattering rate is given by Eq. (2.69) with the first two terms in the braces omitted and the sign of the third term made positive.

To address the issue of screening, we consider the static dielectric response function^{103,104} of a one-dimensional conductor,

$$\frac{\epsilon(x_k)}{\epsilon_s} = 1 + \frac{2e^2}{\pi\epsilon_s x_k^2 R^2} \left[K_1(x_k) I_1(x_k) - \frac{1}{2} \right] \times \left(\frac{1}{\pi} \int_{-\infty}^{\infty} \frac{f_0(k' + 2k) - f_0(k')}{E(k' + 2k) - E(k')} dk' \right) \quad (2.70)$$

which will depend on temperature through f_0 . This, in effect, scales the dielectric constant of the medium by the right-hand side of Eq. (2.70). However, at room temperature, the ratio $\frac{\epsilon(x_k)}{\epsilon_s}$ is nearly unity for all nonzero k , so screening can be neglected to a very good approximation.¹⁰⁰

In doped III-V NWs, II scattering dominates at low energies for both background and remote impurities. This is shown for the case of an InSb NW in Figure 2.3. Contrary to the bulk case, deformation potential scattering (AC) is significant in NWs and increases with the inverse square of the NW radius. The onset of PO scattering by phonon emission becomes the dominant mechanism above the optical phonon energy and, as a result, the non-equilibrium distribution (Eq. (2.60)) is strongly depleted at k_{po} . While a power law relaxation time of the form in Eq. (2.62) can, in principle, be defined based on of the *effective* scattering relaxation rate, the resulting smooth curve will not accurately predict the actual scattering rate at a given energy. Hence, τ_0 and s (from Eq. (2.62)) are best used as fitting parameters for experimental data,²² rather than a means of predictive calculation.

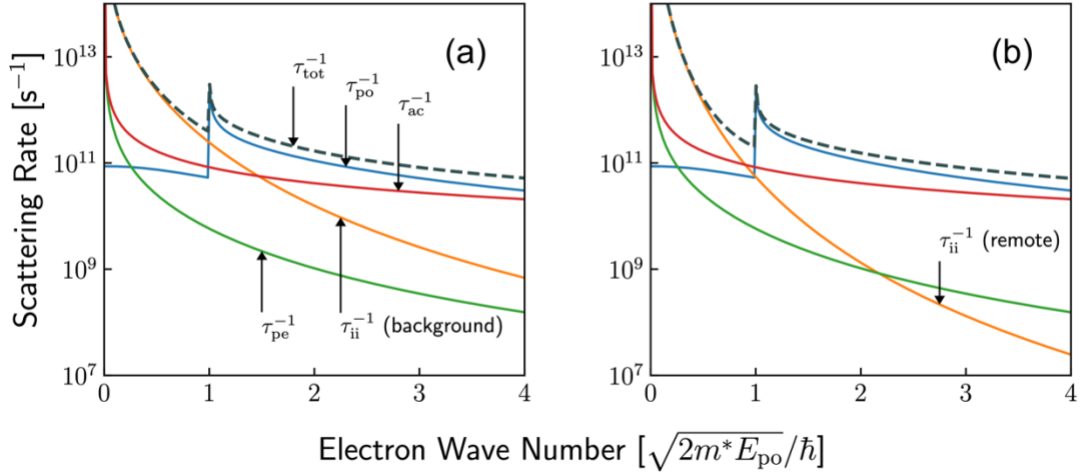


Figure 2.3: Total (dashed) and individual scattering rates in an InSb nanowire at 300 K with (a) background impurity and (b) remote impurity scattering. The nanowire diameter is 20.0 nm and $n = 4.36 \times 10^{16} \text{ cm}^{-3}$.

In terms of electron wave numbers, the current densities due to a single one-dimensional sub-band (labelled j) are given by

$$J_j = \frac{-e}{\pi^2 R^2} \int_{-\infty}^{\infty} v(k) f_j(k) dk \quad (2.71)$$

$$Q_j = \frac{1}{\pi^2 R^2} \int_{-\infty}^{\infty} [E_j(k) - E_F] v(k) f_j(k) dk \quad (2.72)$$

where the group velocity is

$$v(k) = \frac{\hbar k}{m^*} \quad (2.73)$$

Here, $v(k)$ is found by differentiating the NW energy dispersion, Eq. (2.34). The expression $f(k)$ should be understood to mean $f(E_j(k))$ via Eq. (2.2) and (2.34). Note that the equilibrium distribution $f_0(k)$ will not produce any current since $v(k)f_0(k)$ and

$[E_j(k) - E_F]v(k)f_0(k)$ are odd functions of k , which symmetrically spans both negative and positive values. Currents depend solely on the non-equilibrium component of the low-field solution, through $v(k)g_j(k)$, which is even in k .

Adapting the notation for the total electric field (Eq. (2.40)), we write the solution as

$$g_j(k) = \frac{\tau(k)}{\hbar} \frac{\partial f_0}{\partial k} \left\{ eF + \left(\frac{E_j(k) - E_F}{T} \right) \frac{dT}{dx} \right\} \quad (2.74)$$

The NW transport coefficients are then obtained as follows.

The electrical conductivity is defined by Eq. (2.38) in isothermal conditions, where it reduces to an analogue of Ohm's Law:

$$\sigma_j \equiv \frac{J_j}{F} \Big|_{\frac{dT}{dx}=0} \quad (2.75)$$

Using Eq. (2.71), (2.74) and (2.75), the electrical conductivity evaluates to

$$\sigma_j = -\frac{2e^2}{\pi^2 R^2} \int_0^\infty v(k) \left(\frac{\tau(k)}{\hbar} \frac{\partial f_0}{\partial k} \right) dk \quad (2.76)$$

Next, we note that the definition of the Seebeck coefficient (Eq (2.1))—the open-circuit voltage per unit temperature difference—is equivalently re-expressed as the total field per unit temperature gradient. As per Eq. (2.38) with $J = 0$, we obtain

$$S_j \frac{dT}{dx} = F \quad (2.77)$$

Using Eq. (2.71) and (2.74), the vanishing electric current density is

$$0 = \frac{-e}{\pi^2 R^2} \int_{-\infty}^{\infty} v(k) \frac{\tau(k)}{\hbar} \frac{\partial f_0}{\partial k} \frac{dT}{dx} \left\{ eS_j + \left(\frac{E_j(k) - E_F}{T} \right) \right\} dk \quad (2.78)$$

which, under a constant temperature, gradient simplifies to

$$0 = \int_{-\infty}^{\infty} v(k) \tau(k) \frac{\partial f_0}{\partial k} [eTS - (E_j(k) - E_F)] dk \quad (2.79)$$

where T , S and E_F are constant with respect to k . The Seebeck coefficient is then easily found by rearranging Eq. (2.79):

$$S_j = -\frac{1}{eT} \left[\frac{\int_{-\infty}^{\infty} E_j(k) v(k) \tau(k) \frac{\partial f_0}{\partial k} dk}{\int_{-\infty}^{\infty} v(k) \tau(k) \frac{\partial f_0}{\partial k} dk} - E_F \right] \quad (2.80)$$

The ratio of integrals in Eq. (2.80) is interpreted as the average energy of the non-equilibrium electron distribution¹¹ and is directly analogous to the quantity E_j of the single-channel device⁹² discussed earlier.

Lastly, to obtain the electronic thermal conductivity, we once again take $J = 0$, whereby Eq. (2.39) and (2.77) yield a familiar relation for the electronic heat flux:

$$Q_j = -\kappa_{e,j} \frac{dT}{dx} \quad (2.81)$$

From Eq. (2.72), (2.74) and (2.77), we obtain:

$$\frac{Q_j}{dT/dx} = \frac{1}{\pi^2 R^2} \int_{-\infty}^{\infty} (E_j(k) - E_F) v(k) \frac{\tau(k)}{\hbar} \frac{\partial f_0}{\partial k} \left[eS_j + \left(\frac{E_j(k) - E_F}{T} \right) \right] dk \quad (2.82)$$

which leads directly to the electronic thermal conductivity,

$$\kappa_{e,j} = \frac{2}{\pi^2 R^2} \left\{ -e S_j \int_0^\infty (E_j(k) - E_F) v(k) \frac{\tau(k)}{\hbar} \frac{\partial f_0}{\partial k} dk \right. \\ \left. - \frac{1}{T} \int_0^\infty (E_j(k) - E_F)^2 v(k) \frac{\tau(k)}{\hbar} \frac{\partial f_0}{\partial k} dk \right\} \quad (2.83)$$

If the value of S_j has not yet been computed, a straightforward expansion follows from Eq. (2.80):

$$\kappa_{e,j} = \frac{1}{\pi^2 R^2} \left(\frac{1}{\hbar T} \right) \left\{ \frac{\left[\int_{-\infty}^\infty (E_j(k) - E_F) v(k) \tau(k) \frac{\partial f_0}{\partial k} dk \right]^2}{\int_{-\infty}^\infty v(k) \tau(k) \frac{\partial f_0}{\partial k} dk} \right. \\ \left. - \int_{-\infty}^\infty (E_j(k) - E_F)^2 v(k) \tau(k) \frac{\partial f_0}{\partial k} dk \right\} \quad (2.84)$$

To determine the total transport coefficients, sub-band contributions to the electrical and thermal conductivities can be added directly (assuming, for the latter, that the hole contribution is insignificant¹⁰⁵). The total Seebeck coefficient, however, is calculated as an average weighted by the conductivity contribution of each sub-band, *i.e.* $\sum S_j \sigma_j / \sum \sigma_j$.

2.9. Bulk Transport Coefficients

For a baseline to compare with the NW case, the linearized BTE (Eq. (2.52)) can be solved in low-field conditions for a bulk, isotropic, and direct band gap semiconductor using the method given by Rode.^{102,106} The solution here has the form:

$$f(\mathbf{k}) = f_0(k) + g(k) \cos \theta \quad (2.85)$$

where θ is the angle between the applied fields and the electron wave vector (\mathbf{k}). Eq. (2.85) can be understood as a first order expansion of f in spherical harmonics.¹⁰⁷ A distribution of this form characterizes the response of charge carriers inhabiting a spherical (*i.e.* isotropic) conduction band in three dimensions.

In complete generality, the scattering term in the electron BTE is given by^{96,106}

$$\left(\frac{\partial f}{\partial t}\right)_{\text{scatt}} = \int \{s(\mathbf{k}', \mathbf{k})f(\mathbf{k}')[1 - f(\mathbf{k})] - s(\mathbf{k}, \mathbf{k}')f(\mathbf{k})[1 - f(\mathbf{k}')]\} d\mathbf{k}' \quad (2.86)$$

where $s(\mathbf{k}, \mathbf{k}')$ is the differential scattering rate (the rate per unit \mathbf{k} -space volume) and describes the probability per unit time for an electron being scattered from state \mathbf{k} into state \mathbf{k}' . The weighting factor $f(\mathbf{k})[1 - f(\mathbf{k}')]$ is the probability of state \mathbf{k} being occupied while \mathbf{k}' is empty simultaneously, as is required for the event described by $s(\mathbf{k}, \mathbf{k}')$ to occur. The other (positive) term in the integrand accounts for the converse case (a transition from \mathbf{k}' to \mathbf{k}), which can occur just as well.

Following Rode's derivation,¹⁰⁶ the differential scattering rate is separated into contributing elastic and inelastic rates,

$$s(\mathbf{k}, \mathbf{k}') = s_{\text{el}}(\mathbf{k}, \mathbf{k}') + s_{\text{inel}}(\mathbf{k}, \mathbf{k}') \quad (2.87)$$

Since elastic scattering is energy-conserving, it can be shown by the principle of detailed balance⁸¹ that

$$s_{\text{el}}(\mathbf{k}, \mathbf{k}') = s_{\text{el}}(\mathbf{k}', \mathbf{k}) \quad (2.88)$$

The same relation does not hold for inelastic scattering—here attributed entirely to PO scattering, which changes the electron energy by $\pm\hbar\omega_{\text{po}}$. In this case, detailed balance requires:

$$s_{\text{inel}}^+(\mathbf{k}', \mathbf{k}) = s_{\text{inel}}^-(\mathbf{k}, \mathbf{k}') \times \exp\left(-\frac{E_{\text{po}}}{k_B T}\right) \quad (2.89)$$

where the superscripts (+) and (−) indicate phonon absorption and emission, respectively. An electron can scatter both into and out of a state by both absorption and emission, though its energy must exceed E_{po} for emission to be possible.

The equilibrium distribution, $f_0(k)$, is the trivial solution of the BTE (Eq. (2.52)) without applied fields or temperature gradients. Upon substituting Eq. (2.85) into Eq. (2.86), we obtain the equation

$$\int \{s(\mathbf{k}', \mathbf{k})f_0(k')[1 - f_0(k)] - s(\mathbf{k}, \mathbf{k}')f_0(k)[1 - f_0(k')]\} d\mathbf{k}' = 0 \quad (2.90)$$

The fact that the integral is zero can be deduced from three observations: (1) $f_0(k)$ depends only on the magnitude of \mathbf{k} here; (2) the elastic scattering rates conserve the magnitude of \mathbf{k} in an isotropic crystal; and (3) the fact that $f_0(k')[1 - f_0(k)] = f_0(k)[1 - f_0(k')] \exp(-E_{\text{po}}/k_B T)$, with PO scattering being the only inelastic mechanism. Essentially, Eq. (2.90) states that the equilibrium component of the solution can be ignored. Then, by taking terms linear in the perturbation, the BTE for $f(\mathbf{k})$ is reduced to an integral equation for $g(k)$, which in Rode's method^{96,102,106,108} is solved by iterating:

$$g_{i+1} = \frac{S_{\text{in}}^- g_i^- \Theta(E - E_{\text{po}}) + S_{\text{in}}^+ g_i^+ - \xi}{S_{\text{out}}^- \Theta(E - E_{\text{po}}) + S_{\text{out}}^+ + \frac{1}{\tau_{\text{el}}}} \quad (2.91)$$

Here, ξ is equal to the right-hand side of Eq. (2.52) and $\tau_{\text{el}}(k)$ is the total relaxation time due to the elastic scattering mechanisms (AC, PE, and II). The inelastic scattering functions $S_{\text{in/out}}^\pm$, which are given explicitly in Appendix II, are related to integrals over the differential scattering rates in Eq. (2.89). The \pm superscripts indicate a value calculated at $k' = k \pm k_{\text{po}}$, where k_{po} is the magnitude of the electron wave vector at energy E_{po} . Note that k_{po} must be determined by inversion of the non-parabolic bulk dispersion, Eq. (2.31) and (2.32), as also shown in Appendix II.

The iteration begins by taking $g_0(k) = 0$ for all k , yielding the first result:

$$g_1(k) = -\frac{\xi}{S_{\text{out}}^- \Theta(E - E_{\text{po}}) + S_{\text{out}}^+ + \frac{1}{\tau_{\text{el}}}} = -\tau(k)\xi \quad (2.92)$$

which is that same as the RTA (Eq. (2.74)). It is not necessary to re-compute the scattering rates nor the perturbation ξ at each iteration, as these are known functions of k and independent of $g_i(k)$ (though not independent of $f_0(k)$). Convergence of Eq. (2.91) is monotonic, so one merely “updates” $g_i(k)$ until the difference between the i^{th} and $(i + 1)^{\text{th}}$ iterations is negligible. In practice, the number of required iterations is around 10 to 100.

We observe from Eq. (2.91) and (2.92) that $g(k)$ will remain proportional to ξ , given $g_0 = 0$ and that the recursion relation, Eq. (2.91), is effectively

$$g_{i+1} = C_1 g_i^- + C_2 g_i^+ + C_3 \xi \quad (2.93)$$

for some constants C_1 , C_2 and C_3 . Therefore, in calculating the thermoelectric transport coefficients, which are “per unit field” quantities, one shall find that they depend neither on ε nor $\frac{dT}{dx}$, as required physically in the low field (*i.e.* linear response) regime. From a computational perspective, the choices of ε and $\frac{dT}{dx}$ in are completely arbitrary.

Integrating Eqs. (2.56) and (2.57) over spherical coordinates ($d\mathbf{k} = k^2 \sin \theta dk d\theta d\phi$) with the vertical axis parallel to the applied fields, we obtain the expressions:

$$J = -\frac{e}{3\pi^2} \int_0^\infty k^2 v(k) g(k) dk \quad (2.94)$$

$$Q = \frac{1}{3\pi^2} \int_0^\infty [E(k) - E_F] k^2 v(k) g(k) dk \quad (2.95)$$

by using the form of $f(\mathbf{k})$ in Eq. (2.85). Here the velocity obtained by differentiating the non-parabolic bulk dispersion (Eqs. 2.31 and 2.32):

$$v(k) = \frac{\hbar k}{m_e d(k)} \quad (2.96)$$

$$d(k) = \frac{\alpha(k)}{\frac{m_e}{m^*} + [\alpha(k) - 1]} \quad (2.97)$$

and $m^* = m_e d(0)$ is the electron effective mass at the bottom of the conduction band.

The converged distribution $g(k)$, together with the carrier velocity, determines the

differential current density. This is illustrated in Figure 2.4, along with the k -dependence of the relevant scattering rates.

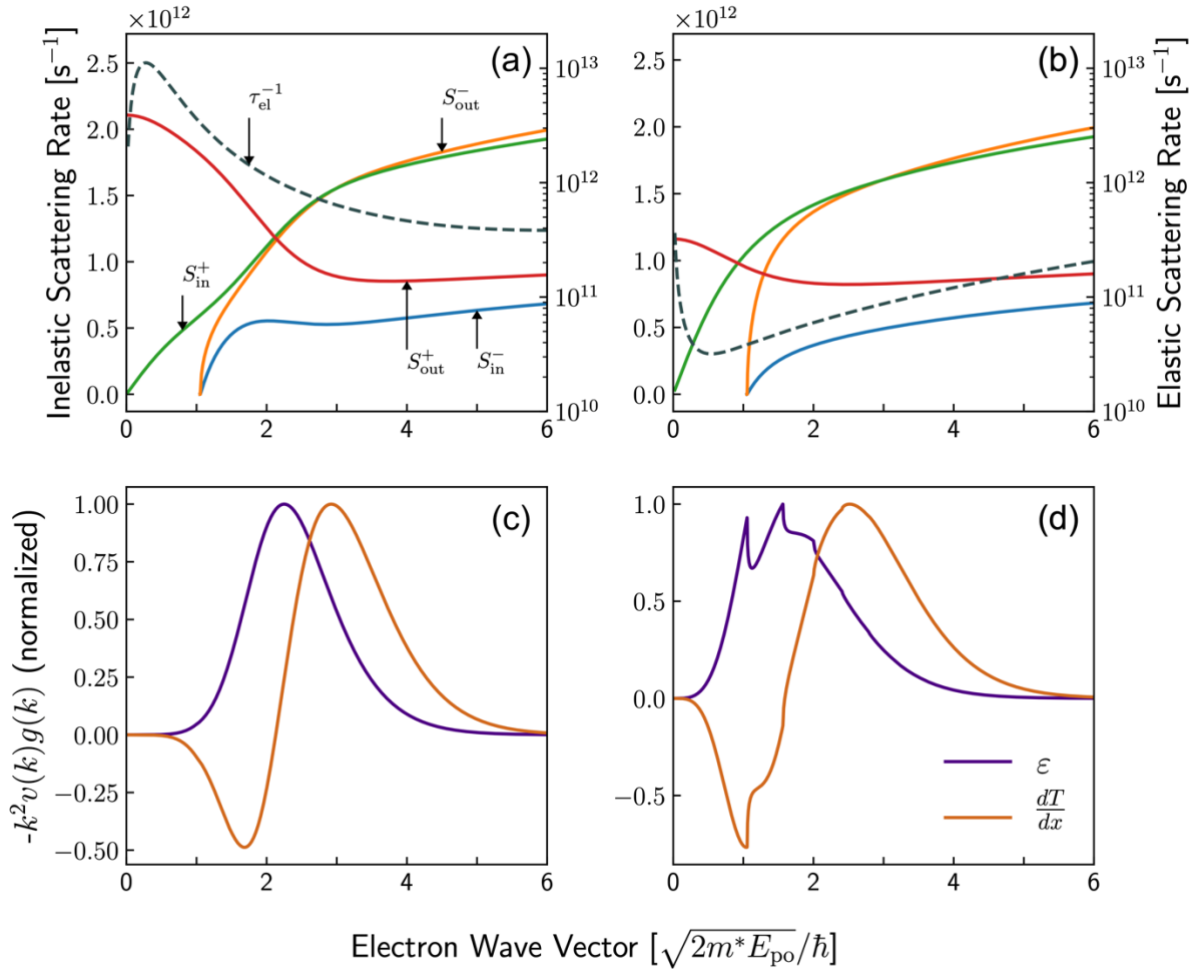


Figure 2.4: Elastic and inelastic scattering rates for bulk III-V semiconductors, shown here for InSb at (a) the optimum carrier concentration of $n = 1.79 \times 10^{17} \text{ cm}^{-3}$ and (b) at the intrinsic carrier concentration, both at 300 K. Panels (c) and (d) show the differential electric current density (proportional to the transport distribution) in either case. The distribution is smoothed by stronger elastic scattering due to ionized impurities in (a) and (c).

Before proceeding with derivations of the bulk transport coefficients, it is prudent to derive an expression for the gradient of the chemical potential, $\frac{\partial E_F}{\partial x}$, in terms of the temperature gradient. In a homogenous conductor,

$$\frac{\partial E_F}{\partial x} = \frac{\partial E_F}{\partial T} \frac{dT}{dx} \quad (2.98)$$

where the right-hand side can be evaluated using the partial derivative identity:

$$\frac{\partial E_F}{\partial T} = - \frac{\frac{\partial n}{\partial T}}{\frac{\partial n}{\partial E_F}} \quad (2.99)$$

Another useful relation is easily derived from the Fermi-Dirac distribution:

$$f_0(k)[1 - f_0(k)] = - \frac{k_B T}{\hbar v(k)} \frac{\partial f_0}{\partial k} \quad (2.100)$$

From Eq. (2.54), carrier concentration (n) is

$$\int \rho_k f_0(k) d\mathbf{k} = \frac{1}{\pi^2} \int_0^\infty k^2 f_0(k) dk \quad (2.101)$$

so its partial derivatives, via the relations in Eq. (2.49) and (2.100), are

$$\frac{\partial n}{\partial T} = \frac{1}{\pi^2 k_B T^2} \int_0^\infty k^2 [E(k) - E_F] f_0(k) [(1 - f_0(k))] dk \quad (2.102)$$

$$\frac{\partial n}{\partial E_F} = \frac{1}{\pi^2 k_B T} \int_0^\infty k^2 f_0(k) [1 - f_0(k)] dk \quad (2.103)$$

Thus, the spatial gradient of the electrochemical potential is deduced from Eqs. (2.99), (2.102), and (2.103):

$$\frac{\partial E_F}{\partial x} = \frac{1}{T} \left[E_F - \frac{\int_0^\infty k^2 E(k) f_0(k) [1 - f_0(k)] dk}{\int_0^\infty k^2 f_0(k) [1 - f_0(k)] dk} \right] \frac{dT}{dx} \quad (2.104)$$

Eq. (2.104) is equivalent to the expression given in Ref. 106 without derivation. Note that the gradient of E_F is, indeed, proportional to the temperature gradient. Therefore, in isothermal conditions, only the applied field (ε) comprises F.

We can now determine the transport coefficients. To obtain the electrical conductivity, $g(k)$ is calculated with $\frac{dT}{dx} = 0$, such that

$$\xi = -\frac{e\varepsilon}{\hbar} \frac{\partial f_0}{\partial k} \quad (2.105)$$

and the total field is $F = \varepsilon$. Then, from Ohm's law and Eq. (2.94) for the current density, we have:

$$\sigma = -\frac{e}{3\pi^2 \varepsilon} \int_0^\infty k^2 v(k) g(k) dk \quad (2.106)$$

The Seebeck coefficient was previously obtained by finding S that satisfied $J = 0$ in the open circuit condition. However, it is here more convenient to calculate the Seebeck coefficient from the *short* circuit condition, where the electrostatic potential is uniform ($\varepsilon = 0$). Accordingly, $g(k)$ is found by iterating with

$$\xi = -\frac{1}{\hbar} \frac{\partial f_0}{\partial k} \left\{ \frac{\partial E_F}{\partial x} + \left(\frac{E(k) - E_F}{T} \right) \frac{dT}{dx} \right\} \quad (2.107)$$

Then, from Eq. (2.38):

$$S = \frac{1}{e} \frac{\partial E_F}{\partial x} \left(\frac{dT}{dx} \right)^{-1} - J \left(\sigma \frac{dT}{dx} \right)^{-1} \quad (2.108)$$

where J now represents the short-circuit current and is calculated from Eq. (2.94).

Finally, κ_e is determined under an applied temperature gradient and without current flow ($J = 0$), nor an applied field ($\varepsilon = 0$). In these conditions, Eq. (2.38) yields the definition of the Seebeck coefficient,

$$S = \frac{1}{e} \frac{\partial E_F}{\partial x} \left(\frac{dT}{dx} \right)^{-1} \quad (2.109)$$

which suggests that the ratio of integrals in Eq. (2.104) is E_j for the bulk, in analogy to the RTA result in Eq. (2.80) and the single-channel device result in Eq. (2.4). With this expression for S , Eq. (2.39) collapses to the definition of the electronic thermal conductivity, whence, using Eq. (2.95), we obtain:

$$\kappa_e = \left\{ \frac{1}{3\pi^2} \int_0^\infty [E(k) - E_F] k^2 v(k) g(k) dk \right\} \left(\frac{dT}{dx} \right)^{-1} \quad (2.110)$$

The same ξ (*i.e.*, Eq. (2.107)) should be used to compute the distributions from which we derive both S and κ_e .

The material constants used throughout this chapter are given in Table 2.1. Here the electron effective mass and band gap at 300 K are calculated from the band parameters in Ref. 94. The remaining parameters are taken from Refs. 102 and 106 with the exception of the bulk lattice thermal conductivities, which are widely available.⁴

Table 2.1: Material parameters used for all calculations in this chapter.

parameter	units	InSb	InAs	GaAs	InP
$m^*(300\text{ K})$	m_e	0.0118	0.0247	0.0653	0.07500
$E_g(300\text{ K})$	eV	0.204	0.397	1.483	1.349
ϵ_S	ϵ_0	17.64	14.54	12.90	12.38
ϵ_∞	ϵ_0	15.75	12.25	10.92	9.55
E_{ac}	eV	9.5	11.5	8.6	14.5
c_l	10^{10} N/m^2	7.89	9.98	14.0	12.10
\mathcal{P}	1	0.027	0.017	0.052	0.013
$\kappa_L(\text{bulk})$	W/m-k	18	27	55	68

2.10. Results and Discussion

The bulk transport coefficients and figure of merit were calculated at 300 K with electron concentrations ranging from 10^{16} to 10^{20} cm^{-3} . Bulk results are shown in Figure 2.5. It is clear from these curves that, despite having the highest Seebeck coefficients, bulk GaAs and InP exhibit much lower ZT all carrier concentrations compared to InAs and InSb. This is attributed to the order of magnitude difference in electrical conductivity (more specifically, the electron mobility) between these compounds, with the latter two benefiting from a small electron effective mass. For direct band gap III-V semiconductors, the effective mass is correlated with the value of the energy gap, as evident from Table 2.1. Mahan and Sofo¹⁰⁹ determined an optimum value for E_g of 6 to $10 k_B T$ for a thermoelectric material, using a transport formulation equivalent to the one discussed here. The band gap of InSb is in this range (with $k_B T \approx 0.026\text{ meV}$, at 300 K), while that of InAs is slightly above, and those of GaAs and InP are

too large. Indeed, the largest bulk ZT is achieved in InSb, at $n = 1.79 \times 10^{17} \text{ cm}^{-3}$. However, this value is too small to merit practical applications of a bulk thermoelectric device based on InSb.

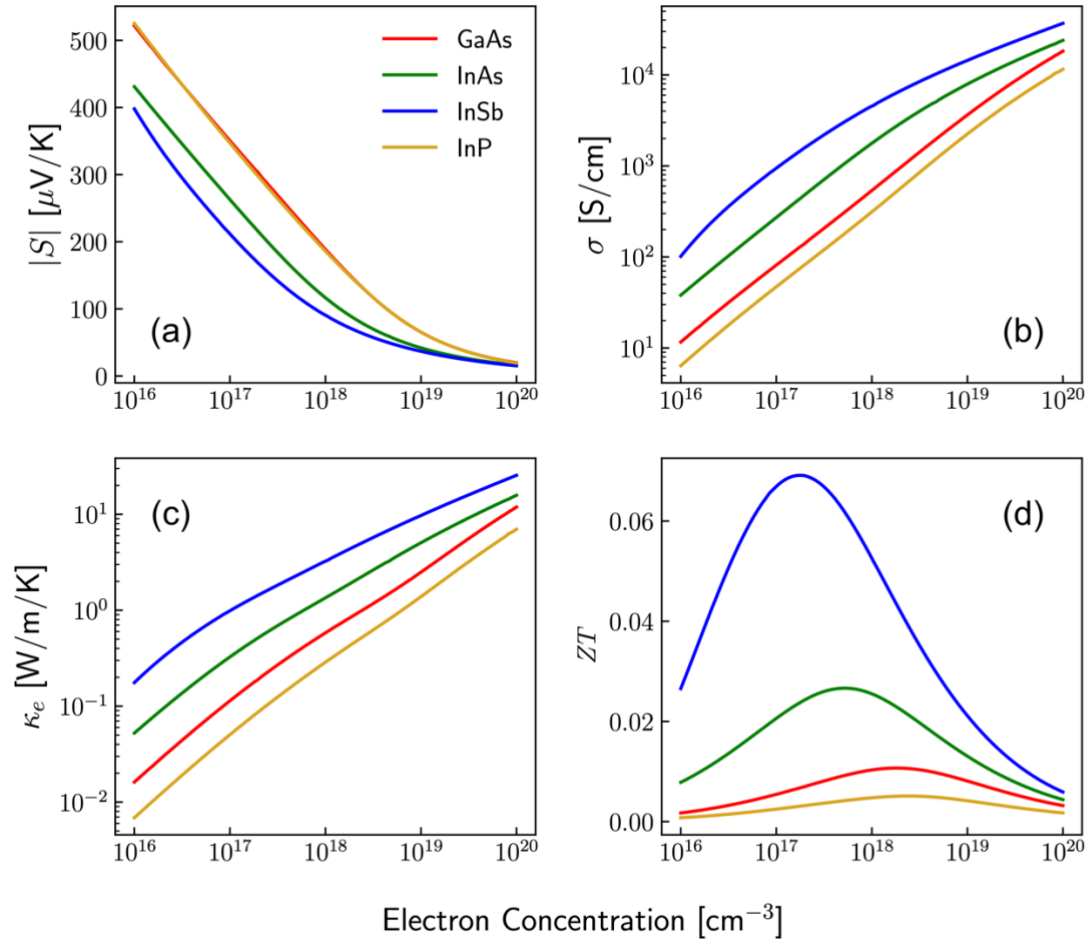


Figure 2.5: Thermoelectric transport coefficients calculated for bulk III-V semiconductors at 300 K. The magnitude of the Seebeck coefficient (a) is calculated using Eq. (2.108), which yields negative values of S , as required. The electrical conductivity (b) and the electronic thermal conductivity (c) are given by Eq. (2.106) and (2.110), respectively. The dimensionless figure of merit (d) is calculated in the usual way (Eq. (1.1)) using the bulk lattice thermal conductivity.

Results for NWs are presented in Figures 2.6 and 2.7 for NW diameters of 10 nm and 1 nm, respectively.

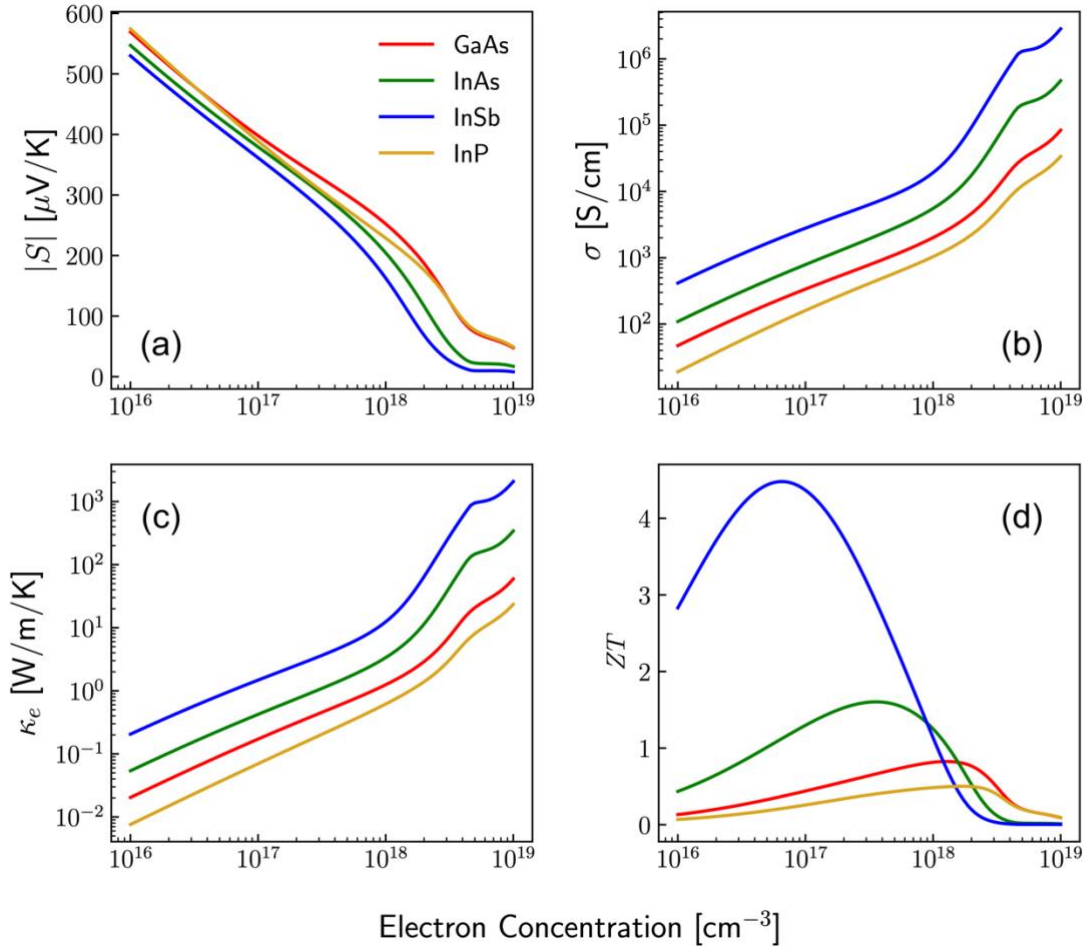


Figure 2.6: Thermoelectric transport coefficients calculated for 10 nm diameter nanowires at 300 K. The total value of all transport coefficients is shown, using the total scattering rate obtained from Matthiessen’s rule applied over Eqs. (2.63) to (2.69), with $R = 5$ nm. The magnitude of the Seebeck coefficient (a) is the conductivity-weighted sum over terms given by Eq. (2.80). The total electrical conductivity and electronic thermal conductivity are calculated by summing over terms given by Eq. (2.76) and (2.83), respectively. The figure of merit (d) is calculated from the total values in the other panels, along with the thermal conductivity curves taken from Ref. 73.

For NW calculations, lattice thermal conductivities as a function of diameter are taken from Ref. 73. The results therein indicate thermal conductivity reductions by 1 to 2 orders of magnitude based on calculations using the complete phonon dispersion^{88,110} for the NW structures.

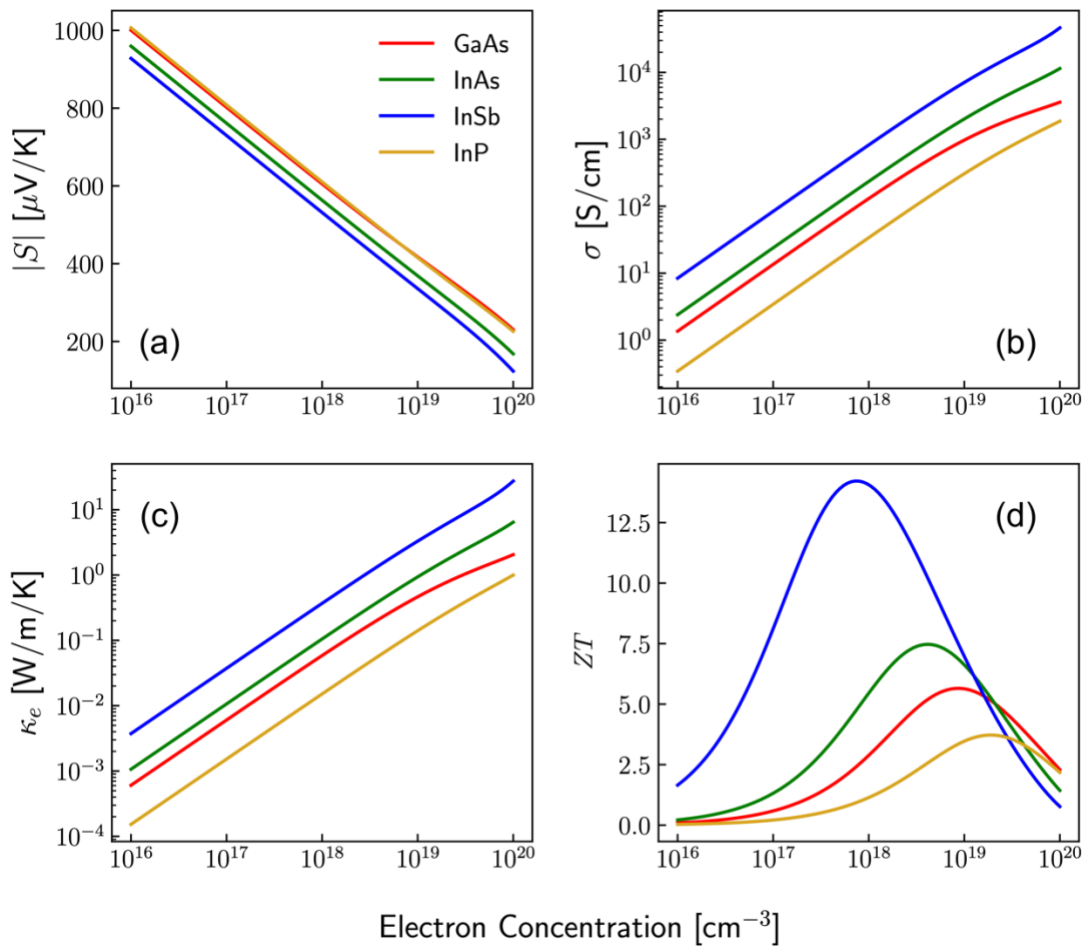


Figure 2.7: Thermoelectric transport coefficients calculated for 1 nm diameter nanowires at 300 K. The total value of all the transport coefficients is shown. The same equations were used as for Figure 2.6, except with $R = 0.5$ nm.

From both Figures 2.6 and 2.7, a large increase in the electrical conductivities is evident versus the bulk values (Figure 2.5). The magnitude of the Seebeck coefficient is also larger in the NW case. Accordingly, so is the power factor, $S^2\sigma$. For 10 nm diameter wires (Figure 2.6), the calculated increase in ZT is nearly 2 orders of magnitude larger than the bulk. A ten-fold reduction of the NW diameter to 1 nm shows an additional ZT increase by a factor of only about 3 (Figure 2.7) because the electron scattering rates (Eq. (2.63) to (2.69)) are increased dramatically as the NW becomes narrower.

The threshold size for electron confinement in nanostructures is usually taken as the thermal de Broglie wavelength, Eq. (1.2), which is a rough indicator of the practical extent of the electron wave function at energy $k_B T$. Since λ_D varies inversely with the effective mass, electron confinement can be achieved at larger diameters in materials with lower effective masses. Figure 2.8 shows the maximum figure of merit and the corresponding n , versus the diameter as a fraction of λ_D .

The room temperature values of λ_D for electrons in the III-Vs considered here are approximately 17 nm (GaAs), 27 nm (InAs), 40 nm (InSb), and 16 nm (InP). This represents a significant engineering challenge, as high-quality vertical arrays of narrow NWs are difficult to produce via SA-VLS growth, especially at higher impurity concentrations.

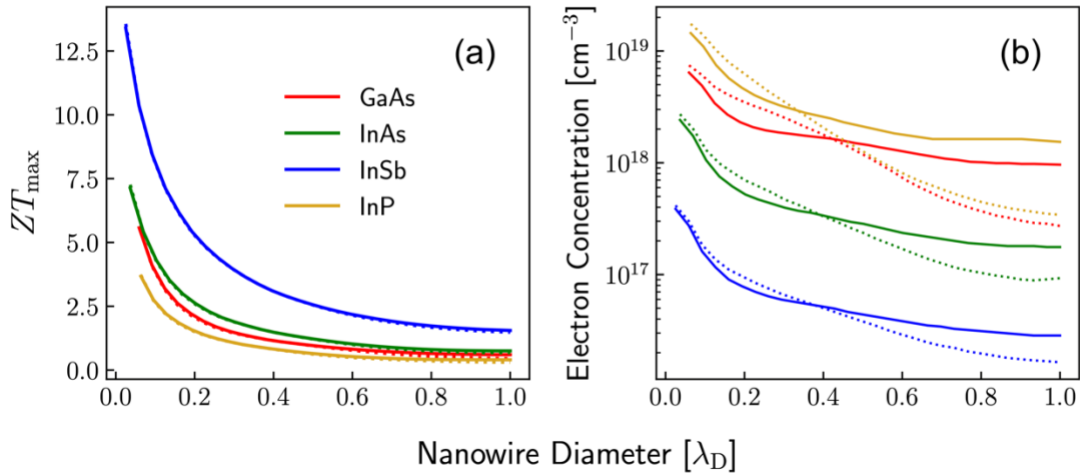


Figure 2.8: (a) Maximum thermoelectric figure of merit for nanowire diameters as fraction of the thermal de Broglie wavelength of the corresponding material, where the minimum diameter is 1 nm and the maximum is λ_D . (b) The electron concentrations that maximize the figure of merit for the corresponding material. Dashed lines in both plots indicate the values for remote impurities.

At larger diameters, the electronic properties are better treated using the bulk dispersion and scattering rates. However, with phonon mean free paths on the order of 100 nm,¹¹¹ reductions in thermal conductivity persist well into the bulk electron transport regime. A significant ZT increase can be predicted for the large NWs in Figure 2.9 versus the bulk (Figure 2.5), owing strictly to thermal conductivity reduction, as per Ref. 73. The resulting ZT values for NW diameters of 50 to 1000 nm, however, are too low to be practical.

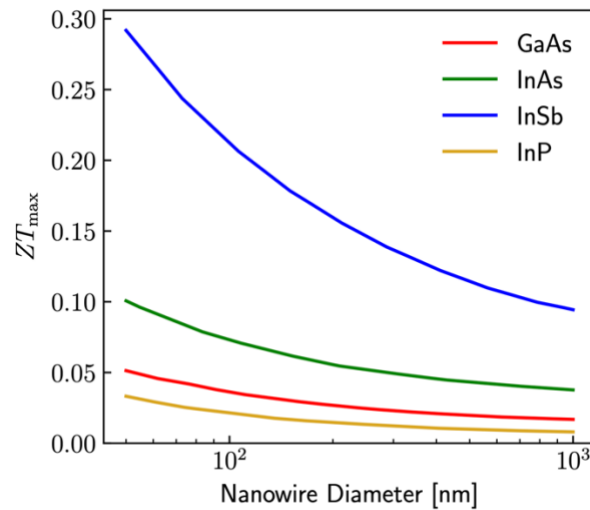


Figure 2.9: Thermoelectric figure of merit of large diameter nanowires.

2.11. Conclusions

Low field thermoelectric transport in III-V semiconductors can be modelled from first principles using the linearized BTE in a semi-classical approach. We have presented here a complete framework for the application of such an approach, using methods compiled from various sources. In both the bulk and NW case, the treatment of electron scattering presents the most significant challenge regarding the calculation of the transport distribution.

For the bulk case, we discussed a method of exact solution based on previous work by Rode,^{96,102,106,108} with an additional generalization to allow for the electronic thermal conductivity to be computed.

For the NW transport distribution, a quasi-relaxation time was calculated from the scattering relaxation rates for the most important mechanisms in highly doped and

polar semiconductors. These models were subsequently used to determine the optimal carrier concentrations that maximize the thermoelectric figure of merit (ZT) in bulk and NW GaAs, InAs, InSb and InP, at 300 K.

We considered both background and modulation doped structures for NWs. In accordance with previous studies, our results indicate that, of the four compounds considered, InSb is the most promising for thermoelectrics. Moreover, the small electron effective mass in InSb allows for carrier confinement to be achieved in larger, more easily manufactured structures, leading to electronic improvements that increase ZT well beyond unity at NW diameters ≤ 40 nm.

3. Measurements of Nanowire Thermal Conductivity

3.1. Summary

Power factor enhancements in NWs, to the degree predicted by theory, remain difficult to achieve with contemporary fabrication methods. Thermal conductivity reductions, on the other hand, are reported universally in NWs and attributed to a variety of mechanisms, including surface roughness, mass disorder, and many kinds of interfaces. Twinning superlattice (TSL) NWs, which feature periodic twinning along the growth direction, are of particular interest as phonon-blocking structures that retain good electronic transport properties simultaneously. This chapter demonstrates the array-scale synthesis of TSL-containing GaAs NWs, along with a direct comparison of the array thermal conductivity to polytypic GaAs NWs of similar length and diameter.

To facilitate thermal conductivity measurements on as-grown NW arrays, we adapted a common NW-composite device architecture for use with the 3ω method. We measured the thermal conductivities of two different vertical GaAs NW arrays, one exhibiting mixed zincblende/wurtzite (ZB/WZ) phase NWs and the other TSL NWs of comparable length and diameter. Values extracted from an effective-medium model indicate thermal conductivities of 8.4 ± 1.6 W/m-K and 5.2 ± 1.0 W/m-K for these two samples, respectively. Our results provide a proof-of-concept for NW thermal conductivity measurements in a device-appropriate setting.

3.2. Introduction

Among the III-V compounds, measurements on InAs^{30–32,34} and GaAs³³ NWs have shown 30-80% reduction in thermal conductivity compared to their bulk value. The influence of structural and compositional features has also been demonstrated. Measurements on Si¹⁸ and Si_{0.96}Ge_{0.04}³⁵ NWs have revealed that surface roughness can grant an additional 70% reduction compared to smooth NWs. Core-shell GaAs-AlAs NWs measured by Juntunen et al.³⁶ showed a non-monotonic dependence on the shell thickness, and a minimal thermal conductivity near 1 W/m-K (versus ~50 W/m-K of bulk GaAs^{112,113}). Li et al.⁴⁹ measured the thermal conductivity of Si/Si_{0.9}Ge_{0.1} superlattice NWs, determining values of 5 to 6 W/m-K at room temperature, much lower than Si NWs of similar size.⁵¹

For a handful of III-V compounds including GaAs,⁵⁵ both the zincblende (ZB) and wurtzite (WZ) phases are accessible during growth and can be selected by adjusting the growth conditions. Polytypic (ZB/WZ),⁶⁶ phase modulated,¹¹⁴ and twinning-ZB^{53,55,56,60} III-V NWs can be produced in this way, with the NW growth conditions determining phase selection.¹¹⁵ Disordered NW structures (Figure 3.1a) are associated with low thermal conductivity⁶⁶ but also low electron mobility,²⁶ which is undesirable for devices. In twinning superlattices (TSLs; Figure 3.1b-d), complementary twin segments form repeating sections that periodically rotate by 60° about the NW axis. From a thermoelectric point of view, TSLs may provide a means of coherent phonon

engineering⁶⁵ based on adjusting the twin period for minimal lattice thermal conductivity.^{47,67,68}

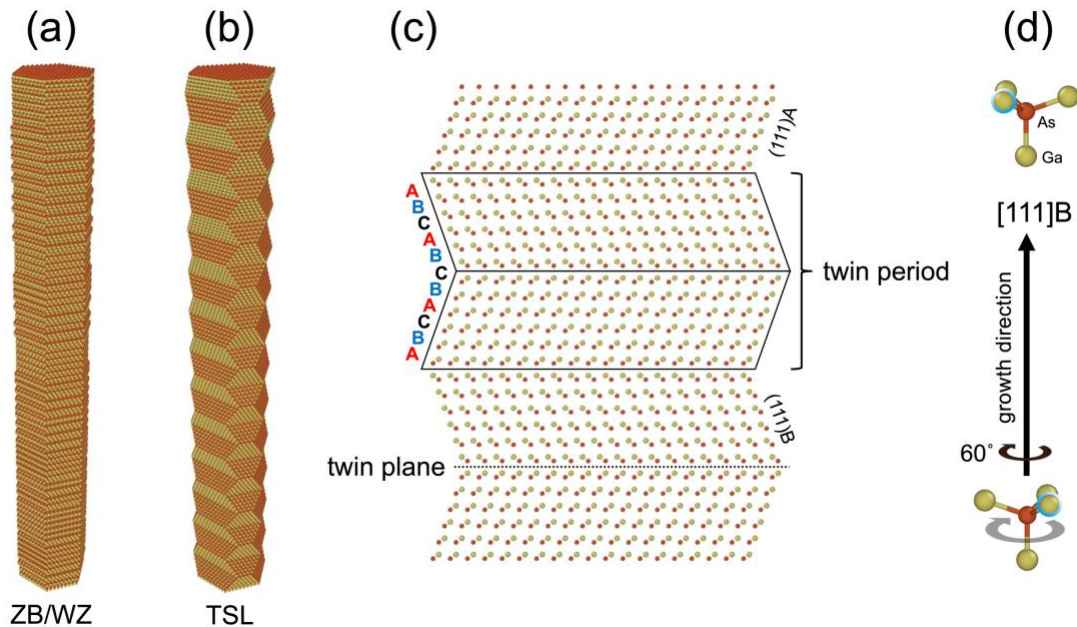


Figure 3.1: Three-dimensional structures for (a) polytypic zincblende/wurtzite (ZB/WZ) and (b) twinning superlattice (TSL) nanowires, showing [111]A and [111]B surface faceting in the latter. (c) Bilayer stacking in the TSL, as seen in an orthogonal projection along $[11\bar{2}]$, exhibiting reversal of the normal ABC stacking sequence across the twin plane. (d) Twinning is equivalent to a rotation of the crystal structure about the NW axis by 60° , illustrated by tetrahedral primitives of bulk GaAs. The indicated growth direction applies to the entire figure.

Many of the NW thermoelectric devices proposed to date^{116–122} employ a composite architecture, with an interstitial material introduced for mechanical support and planarization of the NW array. Among the thermal conductivity measurements reported above, the thermorefectance-based approaches of Persson et al.³⁰ and Juntunen et al.³⁶ are applied directly to measurement devices of this type. Heat flow

remains highly one-dimensional here, so a linear effective-medium model can be used to extract the thermal conductivity of the NWs.³⁰

An alternative to thermoreflectance measurements is the AC 3ω method,^{75,123} which has been used previously to measure the thermal conductivity of NWs embedded in nanoporous Al_2O_3 .^{124–126} Free-standing NW arrays can also be measured in this way, using a spin-on polymer for planarization, as in this work. To examine the influence of crystal structure on the NW thermal conductivity, and to illustrate a novel adaptation of the 3ω method, we report measurements on GaAs NW arrays featuring polytypic ZB/WZ NWs (Figure 3.1a) versus twinning superlattice (TSL) NWs (Figure 3.1b-d).

3.3. Nanowire Growth and Characterization

Arrays of GaAs NWs were grown on $300\ \mu\text{m}$ thick p⁺-Si substrates ($\rho \leq 0.005\ \Omega \cdot \text{cm}$) with a $\langle 111 \rangle$ surface orientation. GaAs NWs were grown in a $2 \times 2\ \text{mm}^2$ area on the substrate surface by the self-assisted vapor-liquid-solid method with a Ga droplet as the seed particle, using gas source molecular beam epitaxy. Two samples were grown with polytypic ZB/WZ NWs (sample A) and twinning superlattice (TSL) NWs (sample B) using identical processes, apart from a Be dopant flux introduced in the latter that induces a TSL structure due to changes in the NW sidewall surface energy.²⁶

After growth, the NW arrays were characterized by scanning electron microscopy (SEM), bright-field transmission electron microscopy (TEM), and high-resolution TEM (HRTEM). Samples were prepared for TEM by mechanically transferring the NWs to a Cu

grid. TEM was performed using a *JEOL 2010F* with 200 kV accelerating voltage. Selective-area electron diffraction (SAED) was performed in the TEM to confirm crystal structure. SEM was performed using a *JEOL 7000F*. SEM confirmed a dense and uniform NW array (Figure 3.2a) from sample B with similar results from sample A with comparable NW length and diameter.

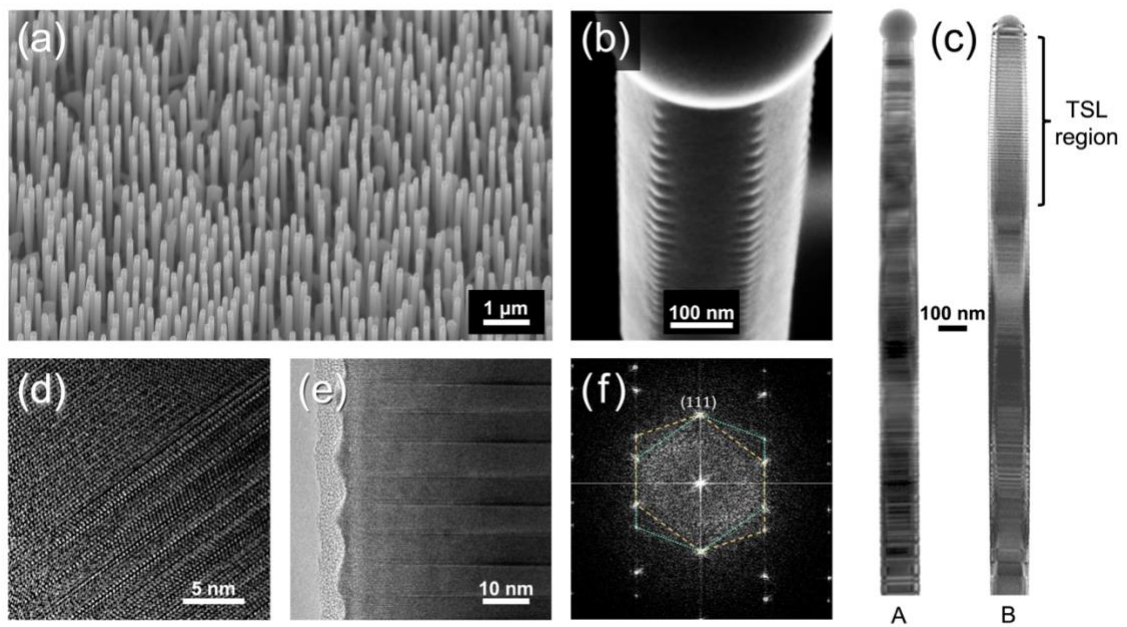


Figure 3.2: (a) SEM image of the NW array from sample B. (b) SEM image of a NW top, showing surface faceting due to a TSL. (c) Size and morphology comparison in side-by-side TEM images of a polytypic NW from sample A (left) and a TSL NW from sample B (right). (d) HRTEM image near the centre of the same NW from sample A, showing polytypic NW structure. (e) HRTEM image near the center of the TSL in sample B. (f) Selective-area electron diffraction pattern confirming ZB twins in the TSL region of sample B.

The growth procedure produced a TSL structure near the top of the NW in sample B, observed by the surface faceting in SEM (Figure 3.2b). A side-by-side comparison, shown in Figure 3.2c, highlights the structural differences between samples

A and B. The crystal structure of sample A is ZB twins with WZ insertions (denoted ZB/WZ, as depicted in Figure 3.1a) as confirmed by HRTEM in Figure 3.2d. The crystal structure of sample B was identical to sample A, except near the top third of the NW where the polytypic structure was replaced with a TSL structure (depicted in Figure 3.1b, c), confirmed by HRTEM in Figure 3.2e and SAED in Figure 3.2f. The Ga droplet that seeded the NW growth is observable at the top of the NW in Figure 3.2b and c. Further growth details are available in Appendix III-a.

3.4. Device Fabrication

The 3ω measurement device is depicted in Figure 3.3. To fabricate the device, layers of benzocyclobutene (BCB) were applied to the NW arrays by repeated spin-coating at 7000 rpm for 77 s, followed by a 1-hour cure at 250 °C in an inert N₂ atmosphere after each coat. In this way, the NWs were completely submerged and insulated by an additional 3.5 μm of BCB above. A layer of *microposit S1827* photoresist was then spin-coated on top of the cured BCB at 3500 rpm for 30 s, and a 1 mm² opening was developed in the photoresist, above a suitable area of the NW array. Using the photoresist as an etch mask, a 0.5 μm deep cavity was etched into the excess BCB using reactive ion etching under 50 W power, with 35.8 sccm CF₄, 5.4 sccm O₂, and 1.8 sccm N₂. This step removed some of the BCB above the measurement section of the NW array, while allowing shorts to be avoided between the heater and longer parasitic NWs. The etch mask was then dissolved in an acetone bath. The height of the remaining BCB

excess was later measured by cross-sectional SEM, as seen in Figure 3.3b. In the final fabrication step, Cr (70 Å) and Pt (1500 Å) metal were deposited on the BCB by evaporation through a mask bearing the heater pattern, and the heater line was positioned diagonally across the cavity etched above the NW array. After deposition, another acetone bath was used to remove the resist and excess metal by lift-off, forming the $30 \times 1000 \mu\text{m}$ heater line and four contact pads illustrated in the inset of Figure 3.3a.

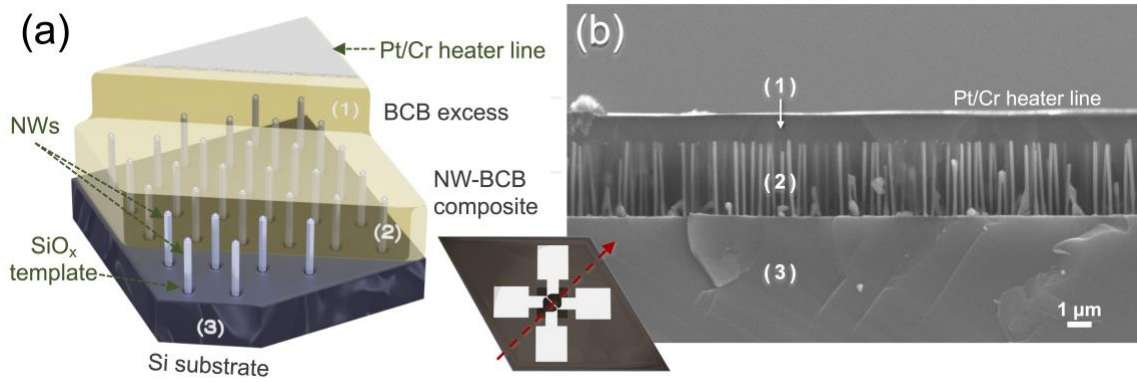


Figure 3.3: Diagrams illustrating the device layers used to model heat conduction: (1) the electrically insulating BCB excess, (2) the target NW-BCB composite layer, and (3) the silicon substrate. (a) 3D schematic of the device, with inset showing the heater line and four contact pads. (b) Cross-sectional SEM image of a device from sample B.

3.5. 3ω Measurements

A *Stanford Research Systems SR810* digital lock-in amplifier was used for AC measurements across a range of frequencies. The complex temperature rise ($\tilde{\theta}_{2\omega,\text{rms}}$) of the heater line was then calculated from the relation¹²⁷

$$\tilde{\theta}_{2\omega,\text{rms}} = \left[\frac{I_{1\omega,\text{rms}}}{\sqrt{2}} \times \frac{dR}{dT} \right]^{-1} (V_{3\omega,\text{rms, re}} - iV_{3\omega,\text{rms, im}}) \quad (3.1)$$

where $I_{1\omega,\text{rms}}$ is the sinusoidal current through the heater line at the source frequency, and $V_{3\omega,\text{rms, re}}$ and $V_{3\omega,\text{rms, im}}$ are the in- and out-of-phase components of the third harmonic voltage across the heater line. In Eq. (3.1), the resistance coefficient $\frac{dR}{dT}$ enables the coupling of voltage and temperature via the temperature-dependence of the line resistance. Resistance coefficients were obtained using a *Thorlabs TED4015* temperature controller together with a Peltier element to sweep sample temperature from 15 to 30 °C while a *Keithley 2000* series multimeter was used to measure line resistances (see Appendix III-b). All AC measurements were done with the sample in vacuum. The heater was contacted by copper probes in a typical four-point configuration with the substrate pressed against an aluminum block. Prior to the 3ω measurement, the electrical resistance was measured between the heater line and the aluminum block (i.e., ground) to confirm the lack of a leakage current through the sample. These measurements yielded resistances exceeding 40 M Ω , owing to the highly insulating BCB. (A small resistance would indicate significant power dissipation inside the sample, invalidating the assumed heat flow model.¹²³) In addition to samples A and B, a third BCB-on-Si sample (sample C) was measured to obtain the baseline thermal conductivity of the BCB. A 400 μm thick Si substrate ($\rho > 1000 \Omega\text{-cm}$) was used for sample C.

3.6. 3ω Data Fitting

To fit the measured temperature data (from Eq. (3.1)), the two-dimensional heat equation can be solved analytically, assuming a uniform heat flux between the line heater and the top layer.^{123,128} This gives the complex temperature rise of the heater as a function of the angular frequency, ω :

$$\tilde{T}_h(\omega) = \frac{\Delta\tilde{T} + pr_{\text{th}}}{1 + i2\omega C_h d_h \left(\frac{\Delta\tilde{T} + pr_{\text{th}}}{p} \right)} \quad (3.2)$$

where

$$\Delta\tilde{T}(\omega) = -\frac{P}{\pi l \kappa_{\perp,1}} \int_0^\infty \frac{1}{A_1 B_1} \frac{\sin^2(b\lambda)}{b^2 \lambda^2} d\lambda \quad (3.3)$$

Here, P is the peak electrical power, while $p = P/2bl$ is the heat flux, b is half the width of the heater line, and l is the length of the heater line. The integration variable, λ , is an inverse length. The parameters C_h , d_h , and r_{th} represent the volumetric heat capacity, thickness, and thermal contact resistance, respectively, of the heater. In Eq. (3.3), $\kappa_{\perp,1}$ is the cross-plane thermal conductivity of the top layer (i.e. the insulating BCB). The remaining thermophysical properties are contained in the coefficients A_1 and B_1 , which are defined by

$$A_{n-1} = \frac{A_n \frac{B_n \kappa_{\perp,n}}{B_{n-1} \kappa_{\perp,n-1}} - \tanh(B_{n-1} d_{n-1})}{1 - A_n \frac{B_n \kappa_{\perp,n}}{B_{n-1} \kappa_{\perp,n-1}} \tanh(B_{n-1} d_{n-1})} \quad (3.4)$$

and

$$B_n = \sqrt{\psi_n \lambda^2 + \frac{i2\omega C_n}{\kappa_{\perp,n}}} \quad (3.5)$$

for layer indices $n = 2, \dots, N$, numbered in increasing order from the second layer down to the substrate (layer (N)), as in Figure 3.3. The quantity ψ_n is the anisotropy ratio, defined as $\psi_n = \kappa_{\parallel,n}/\kappa_{\perp,n}$. The coefficient A_1 of the uppermost layer is determined recursively from Eq. (3.4) and the recurrence is terminated at the substrate layer, where $A_N \equiv -1$. The coefficients B_n , on the other hand, are calculated directly from Eq. (3.5). In this way, the base temperature rise in Eq. (3.3) considers the accumulated influence of layers in the sample, while Eq. (3.2) includes a correction accounting for the physical heater line.¹²³ Thermophysical properties of the sample are extracted by fitting this model (Eqs. (3.2) to (3.5)) to the measured temperature data (Eq. (3.1)).

The data was fitted by minimizing the mean-square-error (MSE) defined by

$$\bar{\epsilon}(\vec{\chi}) = \frac{1}{M} \sum_{k=1}^M \|\tilde{\theta}_{2\omega_k} - \tilde{T}_h(\omega_k, \vec{\chi})\|^2 \quad (3.6)$$

where the vector $\vec{\chi}$ contains the fitting parameters. Each layer in a sample admits four individual parameters, namely the cross-plane thermal conductivity $\kappa_{\perp,n}$, the volumetric heat capacity C_n , the layer thickness d_n , and the anisotropy ratio $\psi_n = \kappa_{\parallel,n}/\kappa_{\perp,n}$.

Samples A and B were modelled as three-layer structures ($N = 3$), consisting of (1) the insulating BCB in contact with the heater, (2) the NW-BCB composite, and (3) the Si substrate, as shown in Figure 3.3. Sample C was modelled as a two-layer structure ($N = 2$), consisting only of (1) a uniform BCB layer and (2) a Si substrate.

The final thermal conductivity of the NW array (κ_{NW}) was calculated from the total thermal conductivity of the NW-BCB composite layer using an effective-medium model:³⁰

$$\kappa_{NW-BCB} = x\kappa_{NW} + (1 - x)\kappa_{BCB} \quad (3.7)$$

Here, the variable $0 \leq x \leq 1$ represents the volume fraction of NWs in layer (2). The volume fraction must account for the NW growth yield because a fraction of oxide holes will not nucleate a NW due to parasitic effects. The yield was estimated by counting all NWs (roughly 4000 individuals) in a $30 \times 30 \mu\text{m}^2$ area of each NW array versus the known density of nucleation sites. The measured thermal conductivities, κ_{NW-BCB} and κ_{BCB} , were obtained by fitting layer (2) of samples A or B and layer (1) of sample C, respectively.

3.7. Results and Discussion

The 3ω measurement data is shown in Figure 3.4a for samples A (red), B (blue), and C (green) along with curves corresponding to the fitted material properties. We considered three separate paradigms for the fit model vis a vis Eqs. (3.2) to (3.5); fitting with (i) the heater contribution neglected ($C_h d_h = 0$, $r_{th} = 0$), (ii) the heater thermal mass neglected ($C_h d_h = 0$, $r_{th} \neq 0$), and (iii) all heater corrections included ($C_h d_h \neq 0$, $r_{th} \neq 0$). Uncertainties on the fitted parameter values were estimated by taking the largest range within the measurement error, which is indicated by the shaded regions around the data points in in Figure 3.4a.

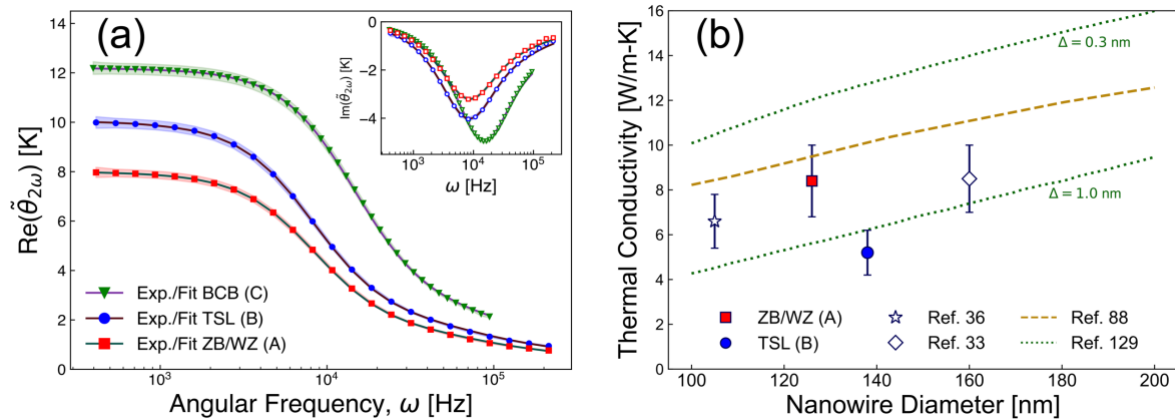


Figure 3.4: (a) Measured temperature amplitudes for samples A, B, and C, along with fitted curves, for the in-phase and out-of-phase (inset) components of each. (b) Thermal conductivity of GaAs NWs, with the polytypic ZB/WZ NWs (red, sample A) and the TSL NWs (blue, sample B) data points corresponding to measurements in panel (a). For comparison, the white markers indicate the experimental results of Juntunen et al.³⁶ and Soini et al.³³ The dashed and dotted lines represent theoretical results from Mingo et al.⁸⁸ and Martin et al.,¹²⁹ respectively, with Δ indicating surface roughness for the latter.

The best overall fit, in terms of the minimal MSE, was achieved using paradigm (ii). Paradigm (iii) produced comparable results for the NW and BCB thermal conductivities, agreeing with (ii) within uncertainty. As can be expected,¹²³ the thermal mass of a $d_h = 157$ nm heater line had only a small effect on the extrapolated values. Inclusion of the thermal resistance, on the other hand, greatly improved the fit. Appendix III-c confirms the sensitivity of the heat model to the thermal conductivities of the upper two layers vis a vis the finite penetration depth^{123,128} of the temperature oscillations, as compared to the thicknesses of the layers (1) and (2) in our samples.

To consider thermal contact resistance between the sample layers, we used the slightly modified model of Olson et al.¹³⁰ to extend Eqs. (3.2) to (3.5). This approach effectively yielded zero resistance between layers (1)-(2) and between layers (2)-(3) in

both samples A and B. A finite thermal resistance between the Cr/Pt heater line and the BCB of layer (1) was necessary to fit the high frequency data ($\omega > 10^4$ Hz) shown in Figure 3.4a. $r_{th} = 0.02 \pm 0.01$ cm²-K/W was obtained for both samples A and B. The complete parameters are tabulated in Appendix III-d.

The array thermal conductivities were determined from NW volume fractions $x_A = 0.056 \pm 0.006$ and $x_B = 0.084 \pm 0.009$ for samples A and B, respectively. Volume fractions were calculated from yields 0.50 ± 0.05 and 0.63 ± 0.05 , and NW diameters $D_A = 126 \pm 5$ nm and $D_B = 138 \pm 5$ nm, for samples A and B, respectively. The thermal conductivity of BCB was 0.19 ± 0.03 W/m-K obtained from sample C. The thermal conductivities for the disordered polytypic ZB/WZ NWs (sample A) and the TSL NWs (sample B) were $\kappa_A = 8.4 \pm 1.6$ W/m-K and $\kappa_B = 5.2 \pm 1.0$ W/m-K, respectively.

As a point of comparison, the bulk GaAs thermal conductivity of ~ 50 W/m-K^{112,113} would give a thermal conductivity of ~ 3 W/m-K at the same volume fraction of samples A or B, where ~ 0.6 W/m-K was in fact measured for the NW-BCB layers. The NW thermal conductivities extracted from the samples are indeed much smaller than 50 W/m-K. The thermal conductivity of the ZB/WZ NWs from sample A was in the same range as prior theoretical and experimental results, as shown in Figure 3.4b (red data point). Here, the theoretical curves taken from Mingo et al.⁸⁸ (dashed) and Martin et al.¹²⁹ (dotted) indicate the approximate size dependence of the thermal conductivity for NWs with fully diffuse phonon-boundary scattering and for NWs with boundaries characterized by a root-mean-square roughness, Δ , respectively. Based on these trends,

the ZB/WZ NWs have a proportionally larger thermal conductivity compared to the 105 nm diameter NWs from Ref. 36. However, the TSL NWs from sample B (blue data point in Figure 3.4b) exhibited a decrease in thermal conductivity within statistical error, despite an even larger diameter. This result is among the lowest thermal conductivities achieved to date for GaAs NWs.

Lower values may yet be attainable by carefully adjusting the TSL period. As in traditional superlattices,^{42,43} there should exist an optimum twin period that minimizes the thermal conductivity of TSL NWs.^{47,67,68} The mechanism of thermal conductivity reduction, while not fully understood,⁴¹ is usually attributed to both coherent and incoherent phonon transport in superlattices.^{27,50} A fraction of phonon modes experience repeated reflections between interfaces, leading to resonances that inhibit axial propagation. Conversely, the same interfaces form resistive barriers for phonons that decohere at shorter length scales. In this view, the superlattice period selects the phonon modes (frequencies and wavelengths) affected by either scattering regime, resulting in a tunable thermal conductivity depending on the contribution of these modes to heat conduction in the periodic structure. Compared to traditional heterojunctions in NWs,⁴⁹ the inherent sharpness of TSL interfaces should improve phonon coherence and provide greater tunability.

3.8. Conclusions

In summary, we measured the thermal conductivity of GaAs NW arrays with polytypic ZB/WZ versus TSL structure, using a NW-BCB composite device structure adapted for the 3ω method. From an effective medium model, we extracted the NW array thermal conductivities, $\kappa_A = 8.4 \pm 1.6$ W/m-K and $\kappa_B = 5.2 \pm 1.0$ W/m-K for the ZB/WZ and TSL NW arrays, respectively.

These results pave the way for future systematic studies aimed at understanding the effect of crystal structure on heat flow in III-V NWs. Further reductions in the thermal conductivity may be possible by tuning the period of the TSL structure (the twin segment length), varying the NW diameter, and inducing TSL formation in other NW materials.

4. Simulations of Heat Transport in Nanowires

4.1. Summary

The zincblende and wurtzite crystal phases of III-V semiconductors correspond to repeating ABC or AB stacking sequences, respectively, of atomic bilayers along the cubic $\langle 111 \rangle$ direction. However, finite structures like NWs are subject to more relaxed sequence selection rules. Because of this, polytypism and/or twinning are common, with many (mostly disordered) stackings of A, B, and C planes being observed in NWs. In principle, this is a vast space of stable configurations, comprised of both periodic and aperiodic structures, which present atomically sharp interfaces in the form of phase and/or twin boundaries. Systematic experiments to investigate structural effects on the thermal conductivity may be difficult with currently available growth technologies. On the other hand, a computational approach affords a straightforward generalization to arbitrary NW structures.

In this chapter, we investigate and compare thermal transport in pristine, twinning superlattice (TSL), and disordered polytypic GaAs NWs, using non-equilibrium molecular dynamics simulations and phonon transmission spectra obtained from the atomistic Green's function method. We find that a TSL period of 50 Å minimizes the thermal conductivity and determine phonon coherence lengths of about 20 to 50 nm, depending on the NW diameter. Our findings indicate a strong dependence of the thermal conductivity on the NW surface and internal structure.

4.2. Introduction

The unique one-dimensional geometry of semiconductor NWs enables the engineering of thermal conductivity for thermoelectric applications.^{24,131,132} Thermoelectrics require a low thermal conductivity to sustain the temperature gradients that drive charge transport. The total thermal conductivity of a crystalline solid includes heat transported by electrons and heat transported by vibrations of the atomic lattice. The lattice contribution is, however, larger than the electronic contribution by at least an order of magnitude in typical semiconductors.¹¹ This fact can be used to control the thermal conductivity with structural features that impede phonon propagation, ideally without reducing carrier mobility.

Values well below the bulk thermal conductivity are obtained even in crystalline NWs^{31,32,51} because phonon transport is suppressed by boundary scattering, which becomes more significant with increasing surface roughness.^{18,35,129} Modulating the internal structure of NWs can further reduce the thermal conductivity by introducing interfaces and mass disorder to the lattice. For example, Li et al.⁴⁹ demonstrated an order of magnitude reduction in thermal conductivity for Si/Si-Ge superlattice (SL) NWs compared to single crystalline Si NWs of similar diameter. The authors attributed the difference to boundary and alloy scattering in the SL NWs, noting a loss of sharpness in the heterojunctions due to diffusion during NW growth. However, atomically sharp interfaces are desired to coherently control the phonon spectra of NWs²⁷ without disrupting electron transport.¹³³

In III-V NWs, both a stable zincblende (ZB) phase (ABCABC... stacking) and a stable wurtzite (WZ) phase (ABAB... stacking) can be achieved.⁵² A wide range of twinning and polytypic structures can also be synthesized in controlled conditions that modify the bilayer stacking sequence during epitaxial growth.^{56,134,135} Twinning superlattice (TSL) NWs^{52–54} comprise a subset of these structures, in which the ZB stacking sequence reverses order periodically (for example, ABCBA). By symmetry of the lattice, this creates a stack of ZB twin segments corresponding to a 60° rotation about the NW axis (Figure 4.1a, b). Relative rotation between twins in the TSL creates a mismatch in the transverse electronic band structure,⁶⁹ such that the twin boundaries effectively connect two dissimilar structures, as in traditional heterojunction SLs. However, due to the inherent sharpness of twin interfaces, TSL NWs may exhibit more coherent phonon transport than traditional SLs. Coherence of the optical TSL modes has been observed by Raman scattering in GaP TSL NWs at room temperature.⁶⁵ Computational studies on a variety of semiconductor SL systems,^{27,47,136,137} as well as TSL Si NWs,⁶⁷ find thermal conductivities depending non-linearly on the twin period, suggesting that tunable (*i.e.*, coherent) acoustic phonon modes could also be realized in practice.

Here, we investigate phonon transport in TSLs and related NW structures that can be observed in the III-V material system, with the goal of elucidating structural effects on the thermal conductivity. Using non-equilibrium molecular dynamics (NEMD) simulations, we simulated heat transfer in coherently twinned (Figure 4.1a, b), randomly

polytypic (Figure 4.1c) and pristine (Figure 4.1d, e) GaAs NWs across a range of twin periods and ZB/WZ ratios. Following previous studies,⁶⁷ we also examined phonon transmission in detail using the atomistic Green's function^{78,79} (AGF) method.

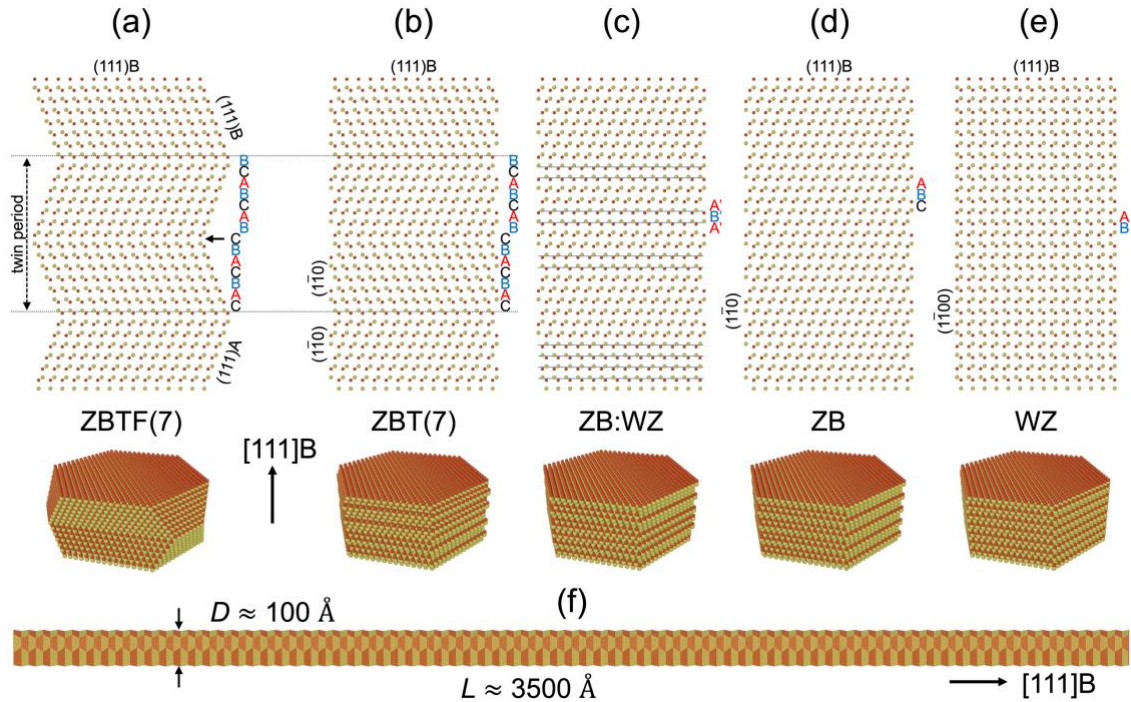


Figure 4.1: Orthographic and perspective views of several representative NW structures studied in this chapter. (a) A faceted TSL NW with a twin segment length of 7 bilayers. (b) A non-faceted TSL NW structure with the same periodicity as (a). (c) A NW exhibiting random polytypism with a ZB/WZ ratio of 50%. (d) A single-crystalline ZB NW. (e) A single-crystalline WZ NW. Corresponding three-dimensional models are shown below each structure in (a)-(e). Horizontal lines in (a)-(e) represent the twin or polytypic boundaries. The faceted TSL NW in (f) spans the length of the simulation cell used in NEMD calculations and is shown here at the largest diameter studied (100 Å).

4.3. Generalizing Nanowire Structures

Viewing the NWs as stacks of atomic bilayers along $\langle 111 \rangle_B$, three unique planes of lattice points can be identified up to translational symmetry along the NW axis, as

usually distinguished by the labels A, B, and C. Any permutation of the bilayer stacking sequence represents another valid stacking sequence in the NW, provided there are no adjacent identical planes. The WZ structure (Figure 4.1e) is obtained from AB stacking, and the ZB structure (Figure 4.1d) is obtained from ABC stacking. Random ZB/WZ polytypic NWs (Figure 4.1c) containing a ZB fraction $0 \leq x \leq 1$, here called ZBWZ(x), can be obtained by randomized insertion of the required number of WZ segments. TSL structures (Figure 4.1a, b) are generated by flipping the ZB stacking order after every n bilayers. This produces a NW with a twin period of $2n$ atomic bilayers. Two structures of this type were considered here—those with (111)A and (111)B side facets (Figure 4.1a) and those with vertical sidewalls (Figure 4.1b). These are referred to as ZBTF(n) and ZBT(n), respectively. The ZBTF structure produces twin segments that are horizontal truncations (slices) of an octahedral supercell with one face perpendicular to the NW axis,⁵⁴ as are readily observed in TSL NWs.^{52,53,55} For ZBTF(n), there exists a maximum n (*i.e.*, twin segment length), corresponding to the distance between two flat faces of the octahedral supercell. By comparison of the faceted ZBTF(n) structure to the non-faceted ZBT(n) structure, the relative importance of the NW surface can be deduced, since the ZBT(n) surface is a close approximation to the non-twinning ZB (1 $\bar{1}$ 0) surfaces, whereas ZBTF(n) exhibits corrugated but more stable (111)A/(111)B faceting of the sidewalls.

4.4. Computational Methods

The LAMMPS¹³⁸ package was used for all NEMD simulations together with the empirical Tersoff potential¹³⁹ to describe the various configurations of GaAs studied here. This potential accurately reproduces the bonding and cohesive energies of several Ga-As configurations as well as the elastic constants of ZB GaAs when compared with calculations from density functional theory (see Tables I-IV in Ref. 139). The total length of the NWs was extended to approximately 350 nm, where size-dependent saturation of the thermal conductivity was observed (see Appendix IV-a). Periodic boundary conditions were imposed to connect the top and bottom layers of the NWs, with vacuum regions isolating the finite structure laterally. The simulated NWs had diameters of approximately 50, 75, or 100 Å. Figure 4.1f shows a scale model of the 100 Å diameter ZBTF(7) NW used in NEMD simulations. All structures were equilibrated at a constant pressure and temperature of 1 atm and 300 K, respectively, over 2.67 million timesteps with $\Delta t = 5 \times 10^{-4}$ ps. Subsequently, to simulate heat transfer, the NWs were divided into 52 equal-sized bins along the z -direction, and an artificial heat flux was imposed between the first bin and the central bin by kinetic energy swapping according to the Müller-Plathe algorithm.⁷⁷ This led to a steady heat flow and a linear temperature gradient extending from the hot center bin to both cold bins at opposite ends of the NW. Thermal conductivity was then obtained from the steady state by applying Fourier's law.

To calculate frequency-dependent phonon transmission across planar interfaces in the various NW structures, we employed the AGF method^{78,79} with the usual “contact-device-contact” geometry adapted to our NW structures. The “device” portions were formed by one unit cell of a periodic NW (for example, an ABC triplet for ZB), while the “contacts” consisted of infinite repetitions of the same unit cell along $\pm z$. Harmonic approximations of the inter-atomic force constants were extracted using the Phonopy¹⁴⁰ code, following energy minimization implemented in LAMMPS. Further details are provided in the Appendix IV-b.

4.5. Results and Discussion

4.5.1. *Thermal Conductivity*

NW thermal conductivities from NEMD simulations are shown in Figure 4.2a for pristine ZB and TSL NWs (ZBT(n) and ZBTF(n)), and in Figure 4.2b for polytypic NWs (ZBWZ(x)), at three different diameters of 50, 75, and 100 Å (indicated by the line weight). A large but diminishing increase of the thermal conductivity is clearly seen for each type of NW as the diameter increases, corresponding to a decreasing rate of phonon-boundary scattering with increasing NW diameter.

The NW structures transition from predominantly WZ to ZB when moving left to right in Figure 4.2a or b. In Figure 4.2a, the ZBT(n) thermal conductivity (red) converges to the value for pristine ZB (dashed lines, black) with increasing twin period (bottom axis) or twin segment length, n (top axis). Similarly, the ZBWZ(x) thermal conductivity

(blue) in Figure 4.2b converges to the pristine ZB value as x approaches 1 on the right. This is expected, with ZBWZ(1) being exactly ZB by definition. On the left-hand sides of Figure 4.2a and b, thermal conductivities approach the WZ NW value, where the “twin segments” become single bilayers ($n \rightarrow 1$) or where the ZBWZ ratio (x) becomes zero. Key results from the NEMD simulations are tabulated in Table 4.1, including the left-most data points in Figure 4.2a and b (corresponding to WZ), which are omitted from the plot for clarity. Notably, WZ NWs have higher thermal conductivity compared to ZB, which is discussed further below.

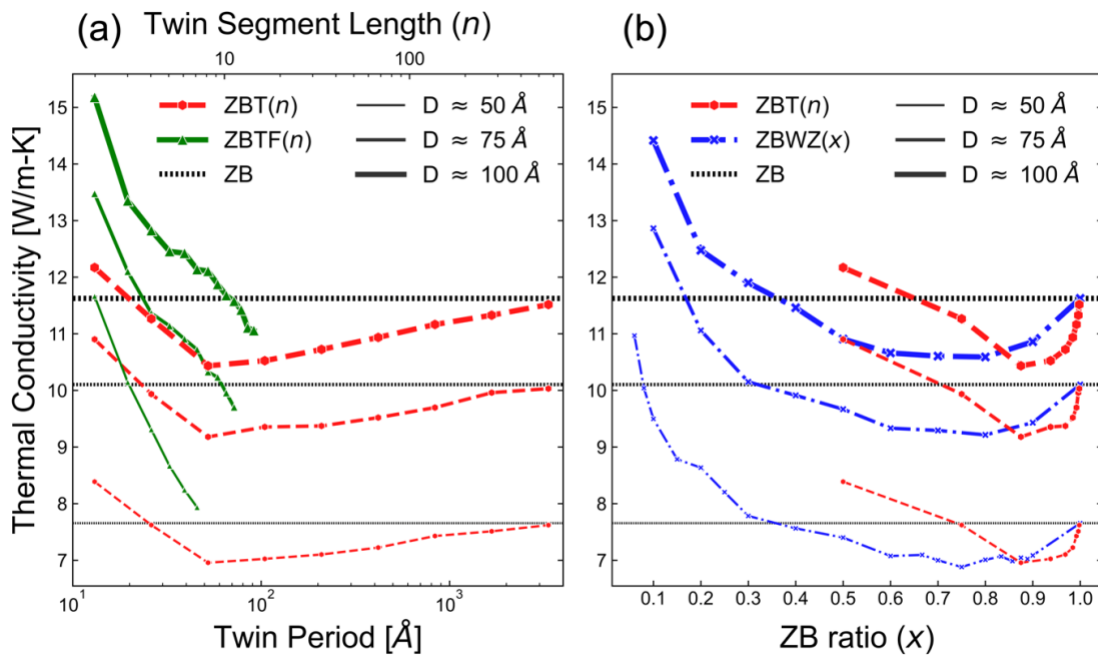


Figure 4.2: (a) NEMD results for the thermal conductivity of non-faceted TSL NWs (ZBT(n), red) and faceted TSL NWs (ZBTF(n), green) versus twin period (bottom axis) or twin segment length in bilayers, n , (top axis). (b) Thermal conductivity versus ZB ratio in ZBWZ(x) (blue) and ZBT(n) (red). Diameters are indicated by the line weight. Dashed lines (black) correspond to the pristine ZB NW thermal conductivities.

Table 4.1: Summary of thermal conductivity extrema (in W/m-K) obtained by NEMD simulations.

	$D = 50 \text{ \AA}$		$D = 75 \text{ \AA}$		$D = 100 \text{ \AA}$	
	min	max	min	max	min	max
ZB	7.7 ± 0.1		10.1 ± 0.1		11.6 ± 0.1	
ZBT(n)	6.9 ± 0.1	8.4 ± 0.1	9.2 ± 0.1	10.9 ± 0.1	10.4 ± 0.1	12.2 ± 0.1
ZBWZ(x)	6.9 ± 0.1	11.4 ± 0.2	9.2 ± 0.1	12.9 ± 0.1	10.6 ± 0.1	14.4 ± 0.3
ZBTF(n)	7.9 ± 0.1	11.7 ± 0.1	9.7 ± 0.1	13.5 ± 0.1	11.1 ± 0.1	15.2 ± 0.1
WZ	22.9 ± 0.4		24.2 ± 0.5		26.5 ± 0.2	

Various transitions between the pristine WZ and ZB phases are represented by the interior data points in Figure 4.2. Here, minima below the pristine ZB conductivity are attained for the ZBT(n) and ZBWZ(x) structures, corresponding to a twin period of $\sim 50 \text{ \AA}$ ($n = 8$) and a ZB ratio of $x \approx 0.8$, respectively. The ZBTF(n) structures also approach such a minimum, but only at the two larger diameters. Thermal conductivity minima appear approximately constant among ZBT(n) and ZBWZ(x) NWs, regardless of diameter. Also, the difference between pristine ZB and the minimum ZBT(n) or ZBWZ(x) value—the depth of the red or blue “valleys” in Figure 4.2—increases with diameter. From this, we infer the increasing contribution of interface versus boundary scattering as diameter increases. For the faceted ZBTF(n) NWs, a monotonically decreasing thermal conductivity is observed in Figure 4.2a up to the maximum possible period length. ZBTF(n) also yields consistently higher thermal conductivities compared to ZBT(n) at the same twin segment length, as well as exhibiting a stronger dependence on the twin segment length. This implies that the (111)A/(111)B side facets of the ZBTF(n) structure scatter phonons with higher specularity²⁹ compared to the atomically rougher (1 $\bar{1}$ 0)

ZBT(n) and ZB surfaces. Higher specularity better preserves phonon coherence, thereby amplifying the structural effect of periodicity (*i.e.*, the dependence on n). Higher specularity also increases the overall thermal conductivity by decreasing the rate of boundary scattering.

To discern the effect of TSL periodicity, the number of WZ bilayer inclusions⁵² introduced by twinning were counted to determine the effective ZB fraction:

$$x = 1 - \frac{1}{n} \quad (4.1)$$

Using Eq. (4.1), the results in Figure 4.2a are recast in terms of the ZB/WZ fraction and plotted in Figure 4.2b. Here, the ZBT(x) (red) and ZBWZ(x) NWs (blue) yield distinct values at the same effective ZB/WZ fraction, despite exhibiting comparable minima in thermal conductivity. The ZBWZ(x) and ZBT(x) structures are evidently not equivalent in terms of heat conduction, which indicates importance of the periodic structure on phonon transport.

To further understand the thermal conductivity results of Figure 4.2, we consider the limit of fully incoherent phonon transport and treat the NWs simply as a mixture of pristine ZB and WZ. In this view, ZBT(x) NWs are a stack of ZB segments separated by twin interfaces (WZ inclusions), while the ZBWZ(x) NWs are random stacks of ZB and WZ segments (including WZ-WZ or ZB-ZB adjacencies). The total thermal resistance is then the sum of series contributions from the ZB/WZ segments, plus the interfaces between them,⁵⁰ $R_{\text{eff}} = \sum R_i + \sum r_j$. It follows that the effective thermal conductivity can be written as

$$\frac{1}{\kappa_{\text{eff}}} = \frac{1}{L_{\text{NW}}} \left(\frac{1}{\kappa_{\text{ZB}}} \sum_i \ell_{\text{ZB}_i} + \frac{1}{\kappa_{\text{WZ}}} \sum_i \ell_{\text{WZ}_i} \right) + N_{\text{int}} \left(\frac{r A_{\text{NW}}}{L_{\text{NW}}} \right) \quad (4.2)$$

In Eq. (4.2), L_{NW} is the total NW length, A_{NW} is the NW cross-sectional area, $\kappa_{\text{ZB/WZ}}$ is the thermal conductivity of pristine ZB or WZ, $\ell_{\text{ZB/WZ}_i}$ is the length of a given ZB or WZ segment, N_{int} is the number of ZB-WZ interfaces, and r is the effective interfacial thermal resistance. Eq. (4.2) reduces to

$$\frac{1}{\kappa_{\text{eff}}} = \left(\frac{1}{\kappa_{\text{ZB}}} - \frac{1}{\kappa_{\text{WZ}}} \right) x + \frac{1}{\kappa_{\text{WZ}}} + N_{\text{int}} \left(\frac{r A_{\text{NW}}}{L_{\text{NW}}} \right) \quad (4.3)$$

where x is the fraction of ZB in the NW. This result models the thermal conductivity of ZBT(x) and ZBWZ(x) NWs in the limit where twin and polytypic interfaces, respectively, are spaced further apart than the effective coherence length, l_c , of incident phonons.²⁷ This would mean that phonons decohere between subsequent interfaces, so resonant modes cannot be sustained. We can therefore estimate l_c as approximately the twin period at which the NEMD results diverge from the incoherent model for ZBT(x).

The number of interfaces in ZBT(x) is given by

$$N_{\text{int}}^{\text{TSL}}(x) = 2n_z(1 - x) \quad (4.4)$$

where $n_z = L_{\text{NW}}/a_z$ is the total number of bilayers in the NW, and a_z is the bilayer atomic spacing along the $\langle 111 \rangle_{\text{B}}$ axis. In the pristine ZB limit, $N_{\text{int}}^{\text{TSL}} \rightarrow 0$ as $x \rightarrow 1$; and $N_{\text{int}}^{\text{TSL}} \rightarrow 2n_z$ as $x \rightarrow 0$, when every consecutive bilayer is one segment of a new twin. Eqs. (4.3) and (4.4) are applicable in the limit of large x ($n \approx 100$ or greater), where ZB segments can be identified in ZBT(x) unambiguously.

In ZBWZ(x), the number of interfaces depends on the specific distribution of WZ segments. Accordingly, the *average* number of interfaces, $N_{\text{int}}^{\text{ZBWZ}}$, for a given ZB fraction was determined. Each WZ cell consists of 2 bilayers and the number of randomly distributed WZ cells is given by $k = (1 - x)m$, where $m = n_z/2$. By a counting argument, the average number of interfaces in ZBWZ(x) is the sum of the number of interfaces over all possible combinations, divided by the number of combinations:

$$N_{\text{int}}^{\text{ZBWZ}}(x) = 2k \binom{m-1}{k} / \binom{m}{k} = \frac{2k(m-k)}{m} \quad (4.5)$$

We confirm that $N_{\text{int}}^{\text{ZBWZ}} \rightarrow 0$ as $k \rightarrow 0$ (no WZ in ZB) and that $N_{\text{int}}^{\text{ZBWZ}} \rightarrow 0$ as $k \rightarrow m$ (no ZB in WZ). For ZBWZ(x), incoherent transport occurs as $x \rightarrow 0$ or $x \rightarrow 1$, since interfaces are most abundant on average near $x = 0.5$.

Figure 4.3 reproduces the NEMD results from Figure 4.2, together with the fit from the incoherent model of Eq. (4.3) with the values of Table 4.2. The WZ inclusions at the twin interfaces in the ZBT(x) NW introduce a lower but comparable equivalent thermal resistance than WZ segments in the random ZBWZ(x) NW. However, the interfacial resistances converge for ZBT(x) and ZBWZ(x) with increasing diameter. At larger diameters, local differences between the outer NW surfaces (Figure 4.1b and c) become less important and the interface is characterized mostly by the internal structures, which are equivalent. Similarly, the increasing l_c is due to decreasing boundary scattering as the diameter increases. Our results for the coherence length in GaAs TSL NWs are in good agreement with the experimental values for GaP TSL NWs

reported by De Luca et al.⁶⁵ To the best of our knowledge, similar experiments have not been performed on GaAs TSL NWs to date.

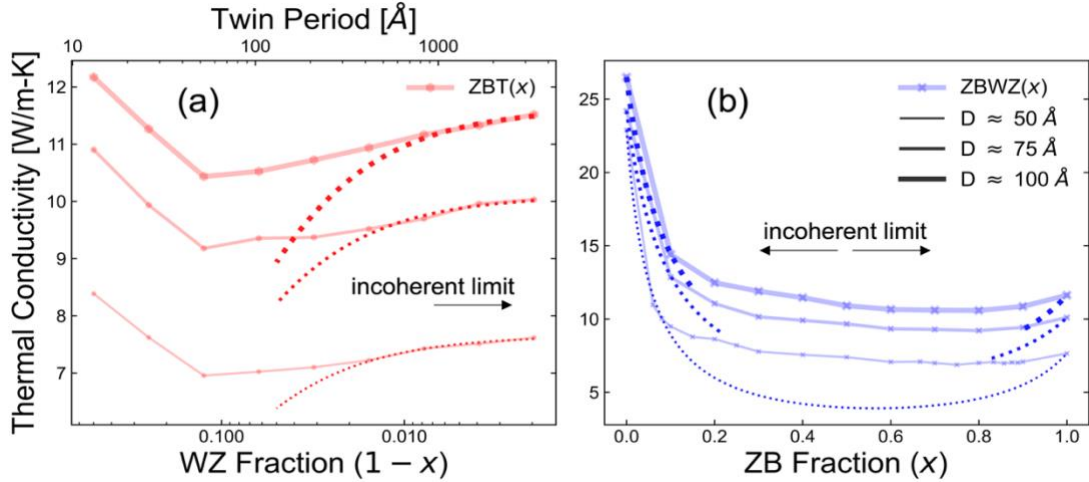


Figure 4.3: NEMD thermal conductivity for (a) ZBT(x) and (b) ZBWZ(x) versus thermal conductivity in the incoherent limit (dotted lines). Corresponding values of r and l_c are shown in Table 4.2.

Table 4.2: Coherence length (l_c) and interfacial thermal resistance (r) between WZ and ZB segments.

diameter [Å]	r^{ZBWZ} [10^6 K/W]	r^{ZBT} [10^6 K/W]	l_c [Å]
50	12.0	5.5	195
75	2.4	1.8	290
100	1.3	1.2	520

4.5.2. Transmission Functions

To understand the globally higher thermal conductivity of WZ and WZ-like NWs, we calculated the transmission function $\mathcal{T}(\omega)$ for ZBT(1) (or WZ), ZBT(2), ZBT(3), and ZB NWs at 50 Å diameter. Results for the transmission function, as well as transmittance compared to ZB, $\mathcal{T}_i/\mathcal{T}_{\text{ZB}}$, are shown in Figure 4.4a.

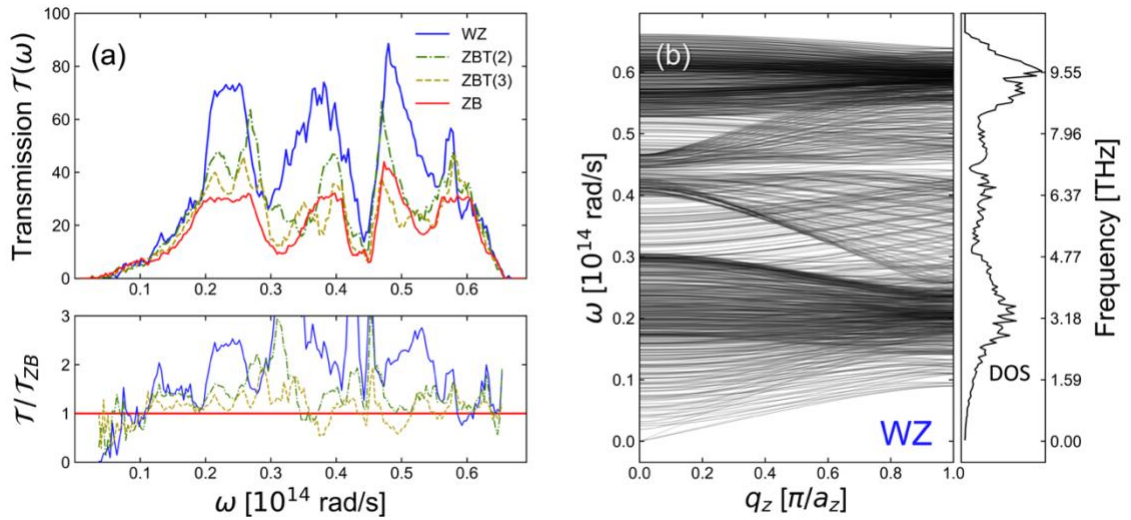


Figure 4.4: (a) Values of the transmission function $\mathcal{T}(\omega)$ for pristine WZ and ZB, as well as several intermediate twinning structures, for NW diameters of 50 Å. In the lower panel of (a), transmission functions are normalized by the ZB transmission. (b) Phonon dispersion and density of states (DOS) for the WZ NW.

Several common features can be discerned among the various transmission spectra. $\mathcal{T}(\omega)$ are much smaller at low frequencies (up to $\omega \approx 0.1 \times 10^{14}$ rad/s) and vanish as $\omega \rightarrow 0$. The same is true at high frequencies, where $\mathcal{T}(\omega) \rightarrow 0$ at $\omega \approx 0.65 \times 10^{14}$ rad/s. The largest values of the transmission function, as well as the largest differences in transmission between the structures, occur in the central frequency range. Differences are less severe in the low frequency range, because long wavelength

phonons are unaffected by structural modulation at smaller length scales. At the highest frequencies, transmission is uniformly low because flat optical bands (representing standing wave modes) are inefficient for axial energy transport. Peaks in the central frequency range match roughly to frequency regions containing dense and sloping optical bands (for example, in Figure 4.4b).

Comparing across the four NW structures, *vis a vis* the lower panel in Figure 4.4a, the transmission function is largest overall for WZ and decreases for increasingly ZB-like NWs, in agreement with the NEMD results for small n . While all four curves exhibit the same general shape, frequency-selective enhancement of the transmission function is evident for ZBT(2) and ZBT(3) from 0.2 to 0.3×10^{14} rad/s, as compared to the ZB case (red curve) in Figure 4.4a. For the ZBT(3) case, selective suppression of the transmission function compared to that for ZB can also be seen around 0.4 and 0.5×10^{14} rad/s. Competition between these mechanisms may explain the minimum in thermal conductivity that is observed by NEMD near $n = 8$, as well as the equivalence between the ZB and ZBT(n) thermal conductivities near small n .

The density of WZ inclusions decreases as $\frac{1}{n}$ with increasing twin segment length n in ZBT(n). The conductivity in the incoherent limit (large n) can be fitted with an effective interface resistance. However, no such interpolation can reproduce the minima of ZBT, because the number of interfaces changes monotonically. In the *coherent* picture, on the other hand, energy is transported by the discrete vibrational modes of the NW unit cell and $\mathcal{T}(\omega)$ represents the relative number of transmission channels

available at energy $\hbar\omega$. Across most of the frequency range, there are many more transmission channels for the WZ NW than for ZB and the other NWs. The ZBT NWs contain both WZ and ZB sub-structures. Thus, when n is small, as in ZBT(2), the transmission is attenuated with respect to WZ (due to the ZB sub-structure) and amplified with respect to ZB (due to the WZ-substructure). Based on these trends and the NEMD data, we infer that TSL modes are most significant near $n = 8$ (twin period ≈ 50 Å). This is further supported by the fact that the minimum thermal conductivity occurs at $n = 8$ independent of the NW diameter.

4.6. Conclusions

A highly tunable NW thermal conductivity was observed by variation of the bilayer stacking sequence. Using NEMD simulations, GaAs NW thermal conductivities ranging from 6.9 to 22.9, 9.2 to 24.2, and 10.4 to 26.5 W/m-K were observed at NW diameters 50, 75, and 100 Å, respectively. Our results indicate that the NW boundaries are of crucial importance to the thermal conductivity, *vis a vis* the discrepancy between ZBT(n) and ZBTF(n) structures with the same periodicity. By comparing uniform and random structures with the same relative crystal phase mixture, we confirmed coherent phonon transport in the twinning ZBT(n) NWs, which at twin period lengths of ~ 50 Å yielded the smallest conductivities overall. The phonon coherence length was estimated at ~ 520 Å for the largest diameter wires. This represents an encouraging result for emerging NW thermoelectrics, insofar as the low thermal conductivities may be

achievable in a controlled and tunable way. The higher thermal conductivity of WZ and WZ-like phases was attributed to higher phonon transmission compared to the ZB phase. Non-monotonic trends in the TSL NW thermal conductivity may be explained by competing suppression and amplification of the transmission function as the twin segment length increases.

Twinning and polytypism are also observed in NWs of several other III-V compounds, including InAs,⁵² InSb,⁵⁶ InP,⁵³ and GaP.⁶⁵ Lower thermal conductivities can be expected in TSL NWs of InAs and especially InSb, where bulk thermal conductivities are around one half and one quarter, respectively, of the bulk GaAs value.⁴ For prospective thermoelectric device applications, higher efficiency is expected from InSb,⁷³ but Ohmic contact formation to InAs is better understood.^{141,142} In future work, the methods presented here can be extended to other III-V materials.

5. Phase Diagram for Twinning Superlattice Nanowires

5.1. Summary

It is essential to understand the mechanisms controlling crystal phase selection during growth to realize any potential benefits from twinning superlattice (TSL) or other structurally complex nanowires (NWs). While previous work has shown that TSLs can be induced in GaAs NWs by the introduction of a Te or Be dopant flux,⁶⁰ the V/III flux ratio and the growth temperature are also important variables in this respect.

This chapter examines TSL formation in Te-doped GaAs NWs grown by a self-assisted vapor–liquid–solid mechanism (with a Ga droplet as the seed particle) using selective-area molecular beam epitaxy. We investigated the crystal structure of NWs across various growth conditions using transmission electron microscopy, finding periodic TSLs only at the low V/III flux ratio of 0.5 and at intermediate growth temperatures of 492 to 537 °C. Higher V/III flux ratios (up to 2) as well as both lower and higher temperatures produced polytypic NWs instead of periodic twinning. These results are explained by a kinetic growth model based on the diffusion flux feeding the Ga droplet.

The contents of this chapter are based on our publication⁶³ in *Nano Letters*, “Phase Diagram for Twinning Superlattice Te-Doped GaAs Nanowires”.

5.2. Introduction

Semiconductor nanowires (NWs) are being examined for a wide range of applications such as photovoltaics, thermoelectrics, betavoltaics, and photodetectors.^{143–145} Recently, twinning superlattices (TSLs) have been explored as a new class of crystal structure in cubic and zincblende (ZB) semiconductors. In the case of III–V semiconductors (such as InP, GaAs, and GaP), the TSL structure is comprised of periodic ZB twins along the length of the NW (the [111]B growth direction), described by a 60° rotation of the ZB crystal structure and accompanied by (111)A and (111)B microfaceting of the NW sidewalls (Figure 5.1a).^{53,55,60,65,146} The bilayer stacking sequence in TSL NWs (Figure 5.1b) resembles that of normal ZB (Figure 5.1c), except for a reversal of the ABC stacking order between consecutive ZB twins.⁵² The ABA sequence across any twin plane (in this case, B) marks a substructure in the TSL with wurtzite (WZ) stacking (Figure 5.1d,e). The twin boundaries and microfaceted surface structure of TSLs have been proposed as a means of phonon engineering to improve thermoelectric efficiency.^{65,67,68} TSLs have also been proposed as a means of allowing direct (phonon-free) inter-band absorption in indirect band gap semiconductors.⁷⁰

Previous work has shown that TSLs can be induced in GaAs NWs by the introduction of a Te or Be dopant flux,⁶⁰ following similar demonstrations of TSL formation by Zn doping of InP,⁵³ GaP,¹⁴⁶ and GaAs⁵⁵ NWs. According to Ref. 60, TSL formation is related to a change in the side facet surface energies of doped ZB GaAs NWs, such that the formation of alternating (111)A and (111)B facets becomes

energetically preferred over vertical $(1\bar{1}0)$ facets. In the present study, we further examine the growth conditions required for TSL formation in NWs, deriving a critical curve outlining the required substrate temperature and V/III flux ratio.

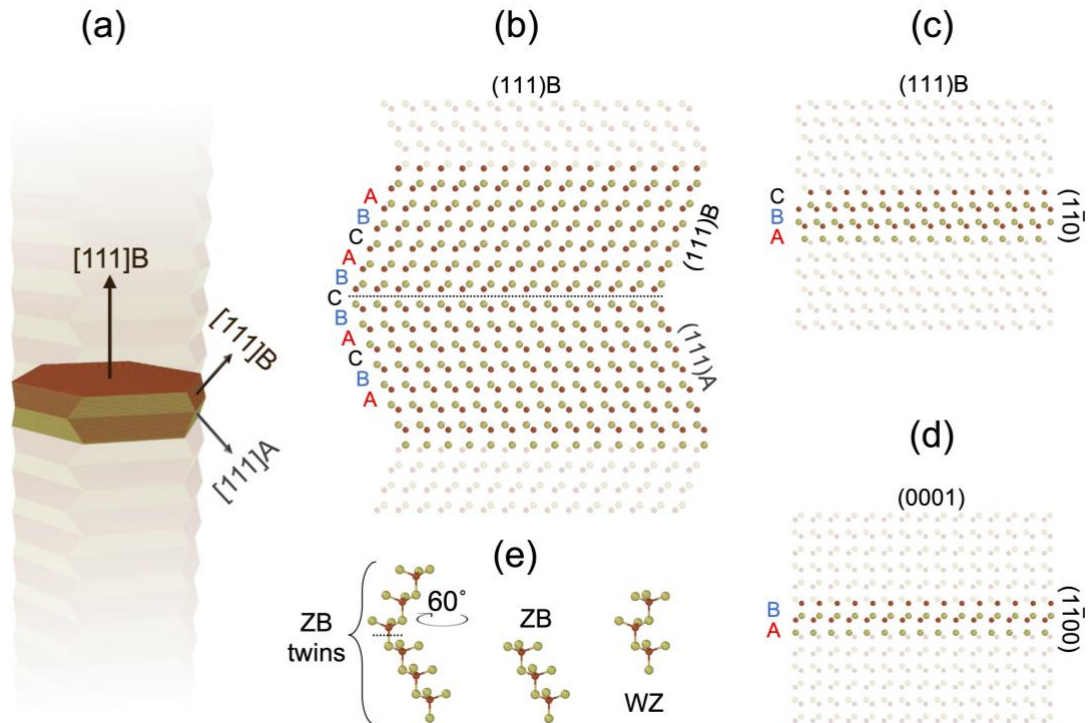


Figure 5.1: (a) Three-dimensional morphology of a TSL NW, with arrows indicating the growth direction and the surface microfacet orientations in one period of the TSL. (b) Bilayer stacking sequence for a ZB TSL nanowire, illustrating reversal (mirroring) of the stacking sequence across the twin boundary. Included for comparison, bilayer stacking sequences in (c) ZB and (d) WZ NWs. (e) Stacking sequence of tetrahedral primitives for each structure type. Yellow and red atoms represent Ga and As, respectively.

5.3. Methods

Self-assisted (SA) GaAs NWs were grown on $\langle 111 \rangle$ Si by the vapor–liquid–solid (VLS) method in a gas source molecular beam epitaxy (MBE) system, using a Ga effusion cell and As_2 supplied by a hydride (AsH_3) gas cracker. Selective-area growth was enabled

by 30 nm of SiO_x deposited by plasma-enhanced chemical vapor deposition and patterned with a hexagonal array of holes, 360 nm in separation, using electron beam lithography. Before loading into the MBE, the substrate was subjected to an HF etch to remove any native oxide at the bottom of the holes. NW growth was limited to the extent of the patterned array where droplet nucleation was promoted by the holes, as confirmed by scanning electron microscopy (SEM) (Figure 5.2a).

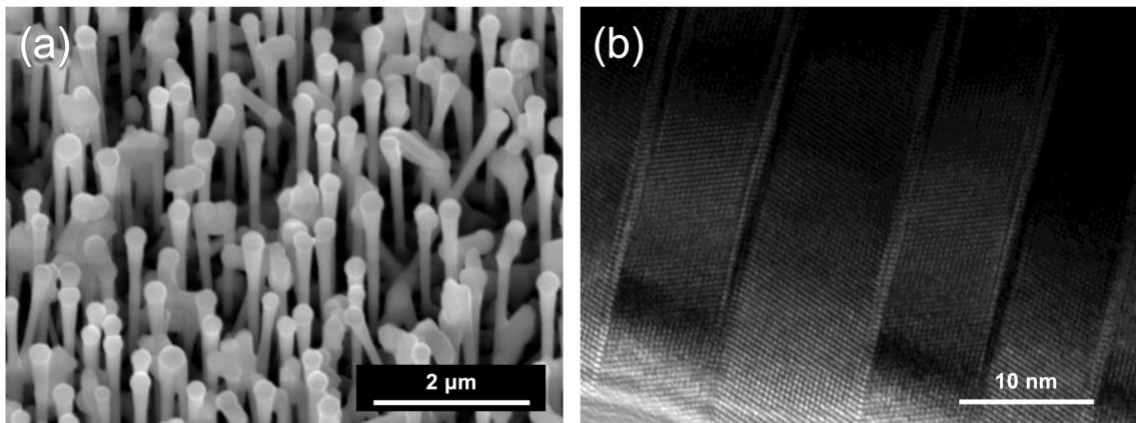


Figure 5.2: (a) SEM image of a self-assisted GaAs NW array grown at 537 °C, with a V/III ratio of 0.5. (b) A corresponding HRTEM image showing twinning at the top of a NW.

The NWs contained an undoped GaAs base grown at a substrate temperature of 630 °C, V/III flux ratio of 2, Ga impingement rate of 0.125 μm/h, and growth duration of 100 min. Subsequently, a NW segment was grown for 30 min with a Ga impingement rate of 0.5 μm/h and Te dopant flux supplied by a GaTe effusion cell. Te fluxes were adjusted for nominal doping levels of 1 to 4 × 10¹⁹ cm⁻³, based on Hall effect measurements on thin film standards, corresponding to NW doping levels of 1 to 4 × 10¹⁸ cm⁻³ as determined by a prior line shape analysis of photoluminescence emission and Raman

scattering.⁶⁴ This dopant flux was shown to induce TSL formation by reducing the surface energies of inward- and outward-tapered NW sidewalls in our previous study.⁶⁰ To further examine the growth parameters required for TSL formation, the final NW segment was grown at temperatures ranging from 448 to 555 °C and with V/III flux ratios of 0.5 and 2. Growths were terminated by shutting the Ga beam and cooling under As₂ flux.

Samples were prepared for transmission electron microscopy (TEM) by mechanically transferring the NWs to a Cu grid. The crystal structure of the NWs was determined by brightfield or high-resolution (HR)TEM (Figure 5.2b), using a *JEOL 2010F* with 200 kV accelerating voltage. Based on the TEM data, we determined a phase diagram indicating the approximate temperatures and V/III flux ratios conducive to TSL formation.

5.4. Results and Discussion

Figure 5.3 shows representative TEM and HRTEM images obtained near the top of the Te-doped GaAs NWs for each of the growth conditions examined in this study. Green points in the phase diagram indicate the observation of a TSL, while red points indicate the absence of a TSL. The higher V/III flux ratio of 2 resulted in a small Ga droplet that was completely consumed by the As₂ flux in the termination step. Consumption of the droplet produced a short polytypic segment at the tips of these NWs¹⁴⁷ (for example, Figure 5.3a), which were otherwise purely ZB and exhibited

vertical $(1\bar{1}0)$ side facets. No twinning was observed at any temperature with a V/III flux ratio of 2.

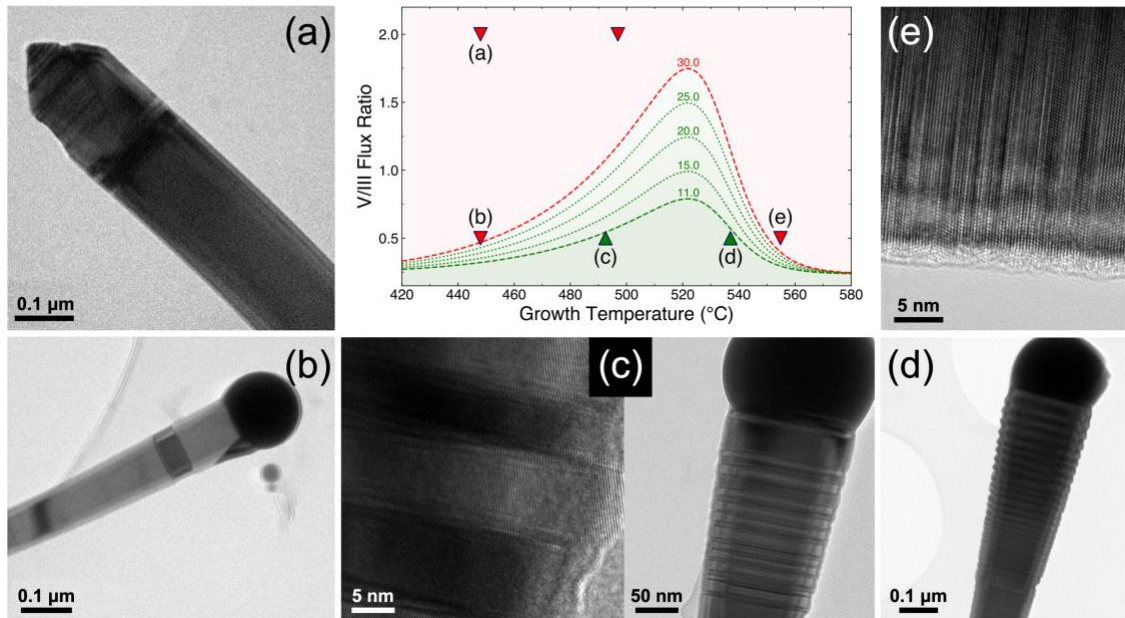


Figure 5.3: Data points at different growth temperatures and V/III flux ratios. Green (TSL) and red (non-TSL) markers indicate the resulting NW morphology. The estimated TSL and non-TSL regions are colored green and red, respectively, with the boundary determined by critical curves calculated from Eqs. 5.5 and 5.6, for $\lambda_3(T_0)/R$ from 11 to 30. Corresponding images of GaAs NW tops showcase the different crystal structures: (a) TEM image showing ZB with low fault density, (b) TEM image showing random ZB twins, (c) HRTEM (left) and TEM (right) showing “pseudoperiodic” TSL, (d) TEM showing periodic TSL, and (e) HRTEM showing a high fault density.

The lower V/III flux ratio of 0.5 resulted in a larger Ga droplet that was not consumed during termination and remained visible in TEM (Figure 5.3b–d). At this flux ratio, we observed a transition into, then out of, a coherent TSL growth regime at 492 to 537 °C (Figure 5.3c,d). Microfaceting of the NW sidewalls corresponding to the $(111)A$ and $(111)B$ facets of the TSL was also visible here, albeit somewhat obscured by the amorphous surface oxide.

A low density of random twins is observed at a growth temperature of 448 °C (Figure 5.3b), with no indication of any microfaceting, to the left of the TSL region. To the right of the TSL region, on the other hand, a high density of random twins is observed (Figure 5.3e) at a growth temperature of 555 °C. Hence, the average twin density is seen to increase with temperature (i.e., droplet size) across Figure 5.3b–e, although coherent TLSs are only achieved in the growth regime represented by the interior green data points. Of these, the “pseudo-periodic” structure observed at 492 °C (Figure 5.3c) is more disordered than the TSL structure at 537 °C (Figure 5.3d).

Radially expanding TSLs form in Te- and Be-doped GaAs NWs during SA-VLS growth under a low V/III flux ratio, with a large droplet contact angle⁶⁰ of $\beta \approx 130^\circ$. The mechanism of TSL formation is related to a change in the surface energies of side facets in doped ZB GaAs NWs, which are modified by dopants incorporating mainly through the NW sidewalls. As such, alternating (111)A and (111)B facets become energetically preferred to the vertical (110) facets.⁵⁷ This explanation differs from a previously proposed mechanism, where TSL formation was explained based on a modification of the droplet chemical potential.¹⁴⁶

In our gas-source MBE growths of self-catalyzed III–V NWs,^{60,134} radial expansion of the NW top facet leads to an inverse tapered (widening) shape, in contrast to Ref. 148, where an almost uniform NW radius was maintained from base to tip. Moreover, the TSL is formed only in the inverse tapered segment of our NWs (Figure 5.3c,d), the growth of which is marked by the start of the dopant flux during growth. While all the

NWs in Figure 5.3 had doping levels corresponding to TSL formation, as per Ref. 60, a TSL was observed only in the NW growths at the lower V/III flux ratio of 0.5 and at intermediate temperatures (492 and 537 °C).

To understand the observed dependence of TSL formation on the growth temperature and V/III flux ratio, we use the results of Ref. 60 and Refs. 149–151. The droplet contact angle corresponding to TSL formation is very close to the large and stable contact angle¹⁵⁰ of $\sim 130^\circ$, at which ZB GaAs NWs begin expanding radially. GaAs NWs form in the WZ phase (Figure 5.1d) at intermediate contact angles¹⁴⁹ from approximately 100° to 125° , where twinning is not possible given the ABAB stacking sequence of bilayers. Tapering (narrowing) of the NWs is observed at a contact angle $\beta \approx 100^\circ$. Based on these data, we can conclude that a large contact angle $\beta \geq 130^\circ$ is required for TSL formation in inverse tapered ZB GaAs NWs. No TSLs can form in WZ nor highly polytypic ZB/WZ NWs growing from Ga droplets with smaller contact angles. The extreme case is represented here by the NWs grown with the high V/III flux ratio of 2, where the droplet was small enough to be consumed completely under the As_2 flux (Figure 5.3a) during termination.

These considerations can be quantified using the following model, where the droplet volume (V) changes with time (t) according to

$$\frac{dV}{dt} = \pi R^2 \left[\chi_3 v_3 + \frac{2 \sin \alpha_3 \lambda_3}{\pi R} v_3 - \frac{dL}{dt} \right] \quad (5.1)$$

Here, R is the radius at the top of the NW, v_3 is the atomic Ga flux, α_3 is the Ga beam angle with respect to the substrate normal (35° in our MBE), λ_3 is the Ga collection

length on the NW sidewalls,¹¹⁴ and χ_3 is the geometrical function of the two angles α_3 and β , which is reduced¹⁵² to $\frac{1}{\sin^2 \beta}$ when $\beta > \alpha_3 + 90^\circ$. The axial NW growth rate, $\frac{dL}{dt}$, in SA growth is As-limited and given by¹⁵³

$$\frac{dL}{dt} = \chi_5 v_5 (1 + \epsilon) - \frac{2}{1 + \cos \beta} v_5^{\text{des}} \quad (5.2)$$

where v_5 is the atomic As flux, χ_5 is the geometrical function for the As beam ($\chi_5 = \chi_3$ at $\alpha_5 = \alpha_3$), and ϵ describes the additional As flux re-emitted from the substrate surface or NW sidewalls. According to Ref. 153, this secondary As flux can be even higher than the primary flux. The second term on the right-hand side describes desorption of As from the droplet and depends on the unknown As concentration in the droplet. We do not consider the shadowing effect¹⁴⁸ because the TSL is contained to the top of the NW.

Using Eqs. (5.1) and (5.2) and assuming $\chi_5 = \chi_3 = \chi$, we obtain

$$\frac{dV}{dt} \propto \frac{v_3}{v_5(1 + \epsilon)} \left[1 + \frac{2 \sin \alpha_3 \lambda_3}{\pi \chi R} + \frac{2}{(1 + \cos \beta) \chi} \frac{v_5^{\text{des}}}{v_3} \right] - 1 \quad (5.3)$$

with the right-hand side determining the sign of the derivative. Based on the experimental observations, the droplet volume must increase at $\beta_* = 130^\circ$ to allow the ZB phase and inverted morphology necessary for forming the TSLs. According to Ref. 60, the TSL period in inverse tapered NWs increases linearly with the NW top radius.

Therefore, the curve

$$\left(\frac{dV}{dt} \right)_{\beta=\beta_*} = 0 \quad (5.4)$$

separates the TSL domain in the phase diagram (V/III flux ratio versus temperature).

From Eq. (5.3), we get the critical curve in the form

$$\frac{v_5}{v_3} = \frac{1}{1 + \epsilon} \left[1 + \frac{2 \sin \alpha_3 \sin^2 \beta_* \lambda_3(T)}{\pi R} + \frac{2 \sin^2 \beta_* v_5^{\text{des}}(T)}{1 + \cos \beta_* v_3} \right] \quad (5.5)$$

where $\lambda_3(T)$ and $v_5^{\text{des}}(T)$ are the two temperature-dependent functions.

We further assume, for simplicity, that $v_5^{\text{des}}/v_3 \ll 1$ by neglecting the As desorption term in Eq. (5.5), which can be justified in many cases.^{153,154} Furthermore, the diffusion length of Ga adatoms is limited by surface incorporation at low temperatures and by desorption from the NW sidewalls at high temperatures,¹¹⁴ with a resulting maximum at $T_0 \approx 522$ °C (795 K). Thus, the temperature dependence of the Ga adatom diffusion length, λ_3 , can be written as¹¹⁴

$$\lambda_3(T) = \lambda_3(T_0) \times \frac{B + C}{B \exp \left[-C \left(\frac{T_0}{T} - 1 \right) \right] + C \exp \left[B \left(\frac{T_0}{T} - 1 \right) \right]} \quad (5.6)$$

where B is the coefficient in the Arrhenius dependence for temperature-activated diffusion of Ga adatoms on the NW sidewalls and C is the coefficient in the Arrhenius dependence for Ga desorption.

The critical curves shown in Figure 5.3 are obtained from Eqs. (5.5) and (5.6), taking $\epsilon = 3.25$ (as in Ref. 153), $B = 20$ (for a Ga diffusion activation barrier of 1.38 eV), and $C = 100$ (for a Ga desorption activation barrier of 6.88 eV), with five different ratios $\lambda_3(T_0)/R$ from 11 to 30. The corresponding range of $\lambda_3(T_0)$ is 770 to 2100 nm, using the mean radius of our NWs before widening, $R = 70$ nm. All these values provide the

correct separation between the TSL and non-TSL regions, in view of the data in Figure 5.3. However, the lowest value (770 nm) agrees best with previously published results regarding the Ga diffusion length on the sidewalls of MBE-grown SA GaAs NWs (usually in the range from 500 to 1000 nm).^{155–157} Including As desorption will not significantly change these results, since it should be almost negligible at low temperatures and enhanced at higher temperatures, resulting in a slight decrease of the droplet size in the latter case. Although our experimental phase diagram contains only a few points, the trend of TSL formation at an optimal temperature and only for low V/III flux ratios is clear and reproduced by the model for a plausible range of Ga diffusion lengths. Overall, the model qualitatively explains the low V/III flux ratio and intermediate growth temperatures required for TSL formation in Te-doped GaAs NWs, with both factors enabling large droplets by maximizing Ga input from surface diffusion.

5.5. Conclusions

To summarize, we examined the crystal structures of several Te-doped SA-VLS grown NWs and found coherent TSL formation in inverse tapered NWs, at a V/III flux ratio of 0.5 and substrate temperatures 492 and 537 °C. Growths outside these conditions did not yield TSL NWs, rather pristine ZB, polytypic, or nonperiodic twinning NWs. Based on the observed requirement of a large Ga droplet (and correspondingly large droplet contact angle), we developed a model to explain the apparent phase boundary outlining the TSL growth regime. Using our model, we calculated a critical curve determined by the maximum V/III ratio that allows for an increasing droplet contact angle at a given temperature. These findings may be useful to control TSL formation in GaAs and other III–V NWs doped with different impurities, such as Be or Zn.

6. Summary and Future Work

6.1. Thesis Summary

Using a first principles analysis, the predicted power factor enhancement in NWs was identified and explained intuitively via benefits to the inherent trade-off between the Seebeck coefficient and the electrical conductivity. Existing theoretical results were incorporated into a predictive Boltzmann transport model for III-V NWs, allowing the optimal electron concentration to be determined at a specified temperature and NW diameter. Subsequent calculations revealed that:

- 1) InSb is indeed the most promising III-V compound for thermoelectric applications, owing mostly to the high carrier mobility (and hence high conductivity) afforded by a small electron effective mass.
- 2) While bulk III-Vs make for inefficient thermoelectrics, narrow III-V NWs (≈ 10 nm diameter) of InAs and InSb could in theory yield $ZT \geq 1$ near room temperature.
- 3) Ultra-narrow III-V NWs (< 10 nm diameter) could yield much larger ZT values, approaching $ZT = 12$ for InSb, though this would require carrier concentrations that increase rapidly with decreasing diameter.

Motivated by encouraging results from prior studies, we demonstrated large reductions in the thermal conductivity of two GaAs NW arrays featuring structural modulation in the form of ZB/WZ polytypism and a twinning superlattice (TSL) induced

by Be doping during growth. This was enabled by a novel application of the 3ω method to free-standing NW arrays planarized by a spin-on polymer. We found that:

- 1) The polytypic and TSL GaAs NWs yielded thermal conductivities of 8.4 ± 1.6 W/m-K and 5.2 ± 1.0 W/m-K, respectively (versus 50 W/m-K of the bulk). However, we were unable to distinguish, in the latter sample, the effect of impurity scattering due to Be doping from structural effects due specifically to the TSL segment.
- 2) TSL segments can be introduced in MBE-grown GaAs NW arrays, while avoiding a significant detriment to the yield, by initiating the patterned NW growth with a 250 s Ga pre-deposition and gradually ramping the temperature and dopant flux, as exemplified in Figure A2.

To explore structural effects theoretically, we employed NEMD simulations and the Atomistic Green's function method to study phonon transport in III-V NWs with pristine, randomly polytypic, TSL, and faceted TSL crystal structures. Lattice thermal conductivity (κ_L) results from our simulations revealed that heat transport in TSL NWs is analogous to traditional superlattices, despite interfaces in the NW consisting entirely of GaAs-GaAs homojunctions. The following conclusions were drawn from this investigation:

- 1) At the diameters studied, the pristine WZ phase exhibits much higher κ_L compared to the pristine ZB phase; owing (i) to a stronger coupling between 'AB'

bilayer units, which significantly improves phonon transmission, and (ii) smoother surface facets in WZ NWs, which decrease the scattering effect of boundaries.

- 2) κ_L decreases rapidly as the TSL period increases, achieving a minimum value at a period of 50 Å, regardless of diameter. In the randomly polytypic NWs, κ_L decreases more gradually with increasing ZB fraction (x), achieving a comparable minimum value at $x \approx 80\%$.
- 3) While twin/phase interfaces were perfectly sharp by construction, room temperature phonon transport was only partially coherent in these NWs and subject to characterization by an effective coherence length ($l_c = 20$ to 50 nm), which varied with the diameter.
- 4) The comparison of transmission spectra across various periodic structures showed the greatest variation near mid-range frequencies, suggesting that crystal modulation at this scale targets propagating optical modes more so than long-wavelength acoustic phonons. A relatively weaker attenuation of narrow frequency bands was also observed in TSL NWs.

Using a kinetic growth model to explain NW morphologies observed by transmission electron microscopy, we derived a phase diagram to inform future self-assisted (SA) vapour-liquid-solid (VLS) growths of TSL NWs. Our findings illustrated the importance of the growth temperature and V/III flux ratio as control variables in this

respect, in addition to the dopant flux that promotes TSL formation. To summarize, we found that:

- 1) A larger Ga flux is required to achieve a Ga droplet contact angle $\beta \geq 130^\circ$ for TSL formation in inverse tapered ZB GaAs NWs, so a lower V/III flux ratio is necessary as well as a growth (substrate) temperature that maximizes the Ga adatom diffusion length on NW sidewalls.
- 2) Coherent TSL formation in inverse tapered NWs occurs at a V/III flux ratio of 0.5 and substrate temperatures around 492 to 537 °C. A higher V/III flux ratio of 2 and temperatures outside this range were seen to produce polytypic NWs, with temperatures below 492 °C leading to a low density of stacking faults and temperatures above 537 °C leading to a high density of stacking faults.

6.2. Future Work

NWs hold significant promise as a platform for efficient thermoelectric devices (TEDs), provided continuing improvements in synthesis technologies to allow more precise control over crystal defects and impurities. The best NW thermoelectrics reported to date (see Appendix I) are, in terms of ZT values, on par with the well-established bulk materials. Further improvements are necessary, via the power factor and/or the lattice thermal conductivity, for prospective NW TEDs to transcend bulk performance.

Reducing NW diameters could be the most direct way to address both these requirements, as this would lower κ_L and intensify the $S^2\sigma$ increase at the same time. Unfortunately, it seems unlikely that SA-VLS growth methods, such as those employed in this work, will produce quality arrays of 1-10 nm diameter NWs in the immediate future. High yield, colinear NW arrays are typically produced with diameters in the range of about 50 to 250 nm, while narrower NWs tend to bend and grow non-vertically, producing arrays to which end-to-end contacts are impossible to apply.[†] Individual NWs could be plucked from a disordered array and fabricated into micro-TEDs, but higher power output will be required—via many cooperating NW thermoelectric elements—to challenge the current state of the art.

Dense composites of narrow and colinear NWs can be formed by deposition into nanochannels in porous media, as several studies have demonstrated.^{125,126,158} However, encouraging results have yet to be reported and a low electrical conductivity appears to affect these devices as well.¹⁵⁸ Nonetheless, the embedded-NW concept may represent a more scalable alternative to TEDs based on planarized free-standing NWs.¹²¹

On the other hand, SA-VLS growth methods are favoured because much more versatility is offered in terms of the NW structure and composition.¹⁷ It may well be the case that, as most of the literature would suggest, greater reductions in κ_L should be pursued for high efficiency NW TEDs, as opposed to $S^2\sigma$ increases through quantum confinement. Indeed, the phononic properties of TSL NWs have only recently been

[†] However, recent studies have succeeded in growing narrow vertical NW segments on top of a wider base.¹⁵⁰

characterized experimentally,⁶⁵ and our thermal conductivity measurements in Chapter 3 are among the first to be reported to date.

Controlled twinning and phase selection in NWs is a similarly novel concept that could see greater development in the coming years. Apart from pristine, TSL, and randomly polytypic NWs, it may be interesting to consider ZB/WZ phase superlattice NWs¹¹⁴ and varying-period TSL NWs. The structural tuning of phonon transport in this way is well suited for systematic computational investigation, as we demonstrated in Chapter 4. To this end, more advanced optimization strategies could be employed to discover idealized morphologies for phonon blocking in NWs.

Another concern is the distribution of impurities in twinning structures, which is likely non-uniform throughout the volume of the NW. While the presence of impurities can significantly lower κ_L , a non-uniform impurity distribution may be detrimental to electron transport. Based on the available experimental data, dopants preferentially incorporate near twin interfaces⁶³ and along certain crystal planes.^{159,160} We used Be-doping to produce our TSLs in Chapter 3, and Te-doping to produce our TSLs in Chapter 5. However, dopant-free TSLs have also been achieved.^{56,61} Indeed, the final crystallography is more directly a function of the droplet kinetics during growth, rather than the flux or identity of dopants.⁶⁰ If dopant-free TSLs and polytypic NWs can be synthesized more readily, the electrical conductivity stands to benefit from modulation doping to introduce free charge carriers without corresponding impurity ions.

Finally, as our own analysis demonstrates in Chapter 2, GaAs is not ideal as a thermoelectric compound. InSb NWs are more promising, but also more difficult to synthesize, owing to the surfactant effect of Sb atoms.¹⁶¹ Very large ZT values are predicted for InSb NWs and, because the Γ -valley effective mass is so small (Table 2.1), the effective confinement diameter is large at room temperature (≈ 40 nm). InAs is next among the III-Vs in terms of potential performance and is easier to synthesize than InSb. InAs NW TEGs are therefore more likely to be used in demonstrating viable III-V TEDs, although high quality InSb NWs are more likely to benefit from power factor enhancement. More broadly, other semiconductors, such as Zn_4Sb_3 , Bi_2Te_3 , and Bi_2Se_3 , also merit consideration for NW TEDs.

References

1. Tritt, T. M. & Subramanian, M. A. Thermoelectric Materials, Phenomena, and Applications: a Bird's Eye View. *MRS Bull.* **31**, 188–198 (2006).
2. Zebarjadi, M., Esfarjani, K., Dresselhaus, M. S., Ren, Z. F. & Chen, G. Perspectives on Thermoelectrics: from Fundamentals to Device Applications. *Energy Environ. Sci.* **5**, 5147–5162 (2012).
3. Rowe, D. M. *CRC Handbook of Thermoelectrics*. (CRC Press, 2018).
4. Cardarelli, F. *Materials Handbook: a Concise Desktop Reference*. (Springer International Publishing, 2018).
5. Kittel, C. *Introduction to Solid State Physics*. (Wiley, 2005).
6. Shi, Y., Sturm, C. & Kleinke, H. Chalcogenides as Thermoelectric Materials. *J. Solid State Chem.* **270**, 273–279 (2019).
7. Rogl, G. & Rogl, P. Skutterudites, a Most Promising Group of Thermoelectric Materials. *Curr. Opin. Green Sustain. Chem.* **4**, 50–57 (2017).
8. NASA RPS: Radioisotope Power Systems. *NASA RPS: Radioisotope Power Systems* <https://rps.nasa.gov/>.
9. Hicks, L. D. & Dresselhaus, M. S. Thermoelectric Figure of Merit of a One-dimensional Conductor. *Phys. Rev. B* **47**, 16631–16634 (1993).
10. Hicks, L. D. & Dresselhaus, M. S. Effect of Quantum-Well Structures on the Thermoelectric Figure of Merit. *Phys. Rev. B* **47**, 12727–12731 (1993).

11. Pichanusakorn, P. & Bandaru, P. Nanostructured Thermoelectrics. *Mater. Sci. Eng. R Rep.* **67**, 19–63 (2010).
12. Kundu, S., Sarkar, C. K. & Basu, P. K. Thermoelectric Power of a One-Dimensional Electron-Gas System. *Phys. Rev. B* **38**, 5730–5732 (1988).
13. Mahan, G. D. & Sofo, J. O. The Best Thermoelectric. *PNAS* **93**, 7436–7439 (1996).
14. Kittel, C. *Thermal Physics*. (W. H. Freeman, 1980).
15. Mavrokefalos, A., Pettes, M. T., Saha, S., Zhou, F., & Li Shi. Combined Thermoelectric and Structure Characterizations of Patterned Nanowires. in *2006 25th International Conference on Thermoelectrics* 234–237 (IEEE, 2006).
16. Seol, J. H. *et al.* Measurement and Analysis of Thermopower and Electrical Conductivity of an Indium Antimonide Nanowire from a Vapor-Liquid-Solid Method. *J. Appl. Phys.* **101**, 023706 (2007).
17. McIntyre, P. C. & Fontcuberta i Morral, A. Semiconductor Nanowires: to Grow or Not to Grow? *Mater. Today Nano* **9**, 100058 (2020).
18. Hochbaum, A. I. *et al.* Enhanced Thermoelectric Performance of Rough Silicon Nanowires. *Nature* **451**, 163–167 (2008).
19. Glassbrenner, C. J. & Slack, G. A. Thermal Conductivity of Silicon and Germanium from 3°K to the Melting Point. *Phys. Rev.* **134**, A1058–A1069 (1964).
20. Liu, Y.-B. *et al.* Synthesis and High-Performance Thermoelectric Properties of Beta-Zn₄Sb₃ Nanowires. *Mater. Lett.* **84**, 116–119 (2012).

21. Tian, Y. *et al.* One-Dimensional Quantum Confinement Effect Modulated Thermoelectric Properties in InAs Nanowires. *Nano Lett.* **12**, 6492–6497 (2012).
22. Schmidt, V. *et al.* Using the Seebeck Coefficient to Determine Charge Carrier Concentration, Mobility, and Relaxation Time in InAs Nanowires. *Appl. Phys. Lett.* **104**, 012113 (2014).
23. Yazji, S. *et al.* Complete Thermoelectric Benchmarking of Individual InSb Nanowires Using Combined Micro-Raman and Electric Transport Analysis. *Nano Res.* **8**, 4048-4060 (2015).
24. Ali, A., Chen, Y., Vasiraju, V. & Vaddiraju, S. Nanowire-Based Thermoelectrics. *Nanotechnology* **28**, 282001 (2017).
25. Wu, P. M. *et al.* Large Thermoelectric Power Factor Enhancement Observed in InAs Nanowires. *Nano Lett.* **13**, 4080–4086 (2013).
26. Karg, S. F. Full Thermoelectric Characterization of InAs Nanowires Using MEMS Heater/Sensors. *Nanotechnology* **25**, 305702 (2014).
27. Tian, Z., Esfarjani, K. & Chen, G. Green's Function Studies of Phonon Transport across Si/Ge superlattices. *Phys. Rev. B* **89**, 235307 (2014).
28. Zou, J. & Balandin, A. Phonon Heat Conduction in a Semiconductor Nanowire. *J. Appl. Phys.* **89**, 2932–2938 (2001).
29. Maznev, A. A. Boundary Scattering of Phonons: Specularity of a Randomly Rough Surface in the Small-Perturbation Limit. *Phys. Rev. B* **91**, 134306 (2015).

30. Persson, A. I., Koh, Y. K., Cahill, D. G., Samuelson, L. & Linke, H. Thermal Conductance of InAs Nanowire Composites. *Nano Lett.* **9**, 4484–4488 (2009).
31. Ren, P. *et al.* Synthesis and Diameter-Dependent Thermal Conductivity of InAs Nanowires. *Nano-Micro Lett.* **6**, 301–306 (2014).
32. Swinkels, M. *et al.* Diameter Dependence of the Thermal Conductivity of InAs Nanowires. *Nanotechnology* **26**, 385401 (2015).
33. Soini, M. *et al.* Thermal Conductivity of GaAs Nanowires Studied by Micro-Raman Spectroscopy Combined with Laser Heating. *Appl. Phys. Lett.* **97**, 263107 (2010).
34. Zhou, F. *et al.* Thermal Conductivity of Indium Arsenide Nanowires with Wurtzite and Zinc Blende Phases. *Phys. Rev. B* **83**, 205416 (2011).
35. Kim, H. *et al.* Effect of Surface Roughness on Thermal Conductivity of VLS-Grown Rough $\text{Si}_{1-x}\text{Ge}_x$ Nanowires. *Appl. Phys. A* **104**, 23–28 (2011).
36. Juntunen, T. *et al.* Thermal Conductivity Suppression in GaAs–AlAs Core–Shell Nanowire Arrays. *Nanoscale* **11**, 20507–20513 (2019).
37. Pokatilov, E. P., Nika, D. L. & Balandin, A. A. Acoustic Phonon Engineering in Coated Cylindrical Nanowires. *Superlattices Microstruct.* **38**, 168–183 (2005).
38. Mei, S. & Knezevic, I. Thermal Conductivity of Ternary III-V Semiconductor Alloys: The Role of Mass Difference and Long-Range Order. *J. Appl. Phys.* **123**, 125103 (2018).
39. Yang, N., Zhang, G. & Li, B. Ultralow Thermal Conductivity of Isotope-Doped Silicon Nanowires. *Nano Lett.* **8**, 276–280 (2008).

40. Ong, Z.-Y., Schusteritsch, G. & Pickard, C. J. Structure-Specific, Mode-Resolved Phonon Coherence and Specularity at Graphene Grain Boundaries. *Phys. Rev. B* **101**, 195410 (2020).
41. Sheng, P. *Introduction to Wave Scattering, Localization, and Mesoscopic Phenomena*. (Springer, 2006).
42. Venkatasubramanian, R., Siivola, E., Colpitts, T. & O’Quinn, B. Thin-Film Thermoelectric Devices with High Room-Temperature Figures of Merit. *Nature* **413**, 597-602 (2001).
43. Venkatasubramanian, R. Lattice Thermal Conductivity Reduction and Phonon Localizationlike Behavior in Superlattice Structures. *Phys. Rev. B* **61**, 3091–3097 (2000).
44. Narayanamurti, V., Störmer, H. L., Chin, M. A., Gossard, A. C. & Wiegmann, W. Selective Transmission of High-Frequency Phonons by a Superlattice: The ‘Dielectric’ Phonon Filter. *Phys. Rev. Lett.* **43**, 2012–2016 (1979).
45. Lin, K.-H. & Strachan, A. Thermal Transport in SiGe Superlattice Thin Films and Nanowires: Effects of Specimen and Periodic Lengths. *Phys. Rev. B* **87**, 115302 (2013).
46. Malhotra, A. & Maldovan, M. Impact of Phonon Surface Scattering on Thermal Energy Distribution of Si and SiGe Nanowires. *Sci. Rep.* **6**, 1-13 (2016).
47. Hu, M. & Poulidakos, D. Si/Ge Superlattice Nanowires with Ultralow Thermal Conductivity. *Nano Lett.* **12**, 5487–5494 (2012).

48. Dames, C. & Chen, G. Theoretical Phonon Thermal Conductivity of Si/Ge Superlattice Nanowires. *J. Appl. Phys.* **95**, 13 (2004).
49. Li, D., Wu, Y., Fan, R., Yang, P. & Majumdar, A. Thermal Conductivity of Si/SiGe Superlattice Nanowires. *Appl. Phys. Lett.* **83**, 3186–3188 (2003).
50. Mu, X. Ultra-Low Thermal Conductivity in Si/Ge Hierarchical Superlattice Nanowire. *Sci. Rep.* **5**, 16697 (2015).
51. Li, D. *et al.* Thermal Conductivity of Individual Silicon Nanowires. *Appl. Phys. Lett.* **83**, 2934–2936 (2003).
52. Caroff, P. *et al.* Controlled Polytypic and Twin-Plane Superlattices in III-V Nanowires. *Nat. Nanotechnol.* **4**, 50–55 (2009).
53. Algra, R. E. *et al.* Twinning Superlattices in Indium Phosphide Nanowires. *Nature* **456**, 369–372 (2008).
54. Johansson, J. *et al.* Structural Properties of <111>B-oriented III-V Nanowires. *Nat. Mater.* **5**, 574–580 (2006).
55. Burgess, T. *et al.* Twinning Superlattice Formation in GaAs Nanowires. *ACS Nano* **7**, 8105–8114 (2013).
56. Yuan, X. *et al.* Dopant-Free Twinning Superlattice Formation in InSb and InP Nanowires. *Phys. Status Solidi RRL* **11**, 1700310 (2017).
57. Ross, F. M., Tersoff, J. & Reuter, M. C. Sawtooth Faceting in Silicon Nanowires. *Phys. Rev. Lett.* **95**, 146104 (2005).

58. Sansoz, F. Surface Faceting Dependence of Thermal Transport in Silicon Nanowires. *Nano Lett.* **11**, 5378–5382 (2011).
59. Moore, A. L., Saha, S. K., Prasher, R. S. & Shi, L. Phonon Backscattering and Thermal Conductivity Suppression in Sawtooth Nanowires. *Appl. Phys. Lett.* **93**, 083112 (2008).
60. Isik Goktas, N., Sokolovskii, A., Dubrovskii, V. G. & LaPierre, R. R. Formation Mechanism of Twinning Superlattices in Doped GaAs Nanowires. *Nano Lett.* **20**, 3344–3351 (2020).
61. Xu, T. *et al.* Faceting, Composition and Crystal Phase Evolution in III-V Antimonide Nanowire Heterostructures Revealed by Combining Microscopy Techniques. *Nanotechnology* **23**, 095702 (2012).
62. Ghukasyan, A., Goktas, N. I., Dubrovskii, V. G. & LaPierre, R. R. Phase Diagram for Twinning Superlattice Te-Doped GaAs Nanowires. *Nano Lett.* **22**, 1345–1349 (2022).
63. Choi, W. *et al.* Direct Electrical Probing of Periodic Modulation of Zinc-Dopant Distributions in Planar Gallium Arsenide Nanowires. *ACS Nano* **11**, 1530–1539 (2017).
64. Goktas, N. I., Fiordaliso, E. M. & LaPierre, R. R. Doping assessment in GaAs Nanowires. *Nanotechnology* **29**, 234001 (2018).
65. De Luca, M. *et al.* Phonon Engineering in Twinning Superlattice Nanowires. *Nano Lett.* **19**, 4702–4711 (2019).

66. Weathers, A. *et al.* Phonon Transport and Thermoelectricity in Defect-Engineered InAs Nanowires. in *MRS Proceedings* vol. 1404 (2012).
67. Xiong, S., Kosevich, Y. A., Sääskilahti, K., Ni, Y. & Volz, S. Tunable Thermal Conductivity in Silicon Twinning Superlattice Nanowires. *Phys. Rev. B* **90**, 195439 (2014).
68. Porter, A., Tran, C. & Sansoz, F. Intrinsic Nanotwin Effect on Thermal Boundary Conductance in Bulk and Single-Nanowire Twinning Superlattices. *Phys. Rev. B* **93**, 195431 (2016).
69. Ikonić, Z., Srivastava, G. P. & Inkson, J. C. Electronic Properties of Twin Boundaries and Twinning Superlattices in Diamond-Type and Zinc-Blende-Type Semiconductors. *Phys. Rev. B* **48**, 17181–17193 (1993).
70. Ikonić, Z., Srivastava, G. P. & Inkson, J. C. Optical Properties of Twinning Superlattices in Diamond-Type and Zinc-Blende-Type Semiconductors. *Phys. Rev. B* **52**, 14078–14085 (1995).
71. Mizuno, S. & Nishiguchi, N. Acoustic Phonon Modes and Dispersion Relations of Nanowire Superlattices. *J. Phys.: Condens. Matter* **21**, 195303 (2009).
72. Hrostowski, H. J., Morin, F. J., Geballe, T. H. & Wheatley, G. H. Hall Effect and Conductivity of InSb. *Phys. Rev.* **100**, 1672–1676 (1955).
73. Mingo, N. Thermoelectric Figure of Merit and Maximum Power Factor in III-V Semiconductor Nanowires. *Appl. Phys. Lett.* **84**, 2652–2654 (2004).

74. Lundstrom, M. *Fundamentals of Carrier Transport*. (Cambridge University Press, 2010).
75. Cahill, D. G. Thermal Conductivity Measurement from 30 to 750 K: The 3ω Method. *Rev. Sci. Instrum.* **61**, 802–808 (1990).
76. Borca-Tasciuc, D.-A. & Chen, G. Anisotropic Thermal Properties of Nanochanneled Alumina Templates. *J. Appl. Phys.* **97**, 084303 (2005).
77. Müller-Plathe, F. A Simple Nonequilibrium Molecular Dynamics Method for Calculating the Thermal Conductivity. *J. Chem. Phys.* **106**, 6082–6085 (1997).
78. Zhang, W., Fisher, T. S. & Mingo, N. The Atomistic Green's Function Method: An Efficient Simulation Approach for Nanoscale Phonon Transport. *Numer. Heat Transf. B: Fundam.* **51**, 333–349 (2007).
79. Sadasivam, S. *et al.* The Atomistic Green's Function Method for Interfacial Phonon Transport. *Annu. Rev. Heat Transf.* **17**, 89–145 (2014).
80. Callen, H. B. The Application of Onsager's Reciprocal Relations to Thermoelectric, Thermomagnetic, and Galvanomagnetic Effects. *Phys. Rev.* **73**, 1349–1358 (1948).
81. Fischetti, M. V. & Vandenbergh, W. G. *Advanced Physics of Electron Transport in Semiconductors and Nanostructures*. (Springer International Publishing, 2016).
82. Ghukasyan, A. & LaPierre, R. R. Modelling Thermoelectric Transport in III-V Nanowires Using a Boltzmann Transport Approach: a Review. *Nanotechnology* **32**, 042001 (2021).

83. Ørsted, H. C. Nouvelles Expériences de M. Seebeck sur Les Actions Électro-Magnétiques. *Ann. Chim. Phys.* **22**, 375 (1823).
84. Peltier, J. C. A. Nouvelles Expériences sur La Caloricité des Courans Électriques. *Ann. Chim. Phys.* **56**, 371 (1834).
85. Mansour, K., Qiu, Y., Hill, C. J., Soibel, A. & Yang, R. Q. Mid-Infrared Interband Cascade Lasers at Thermoelectric Cooler Temperatures. *Electron. Lett.* **42**, 1034 (2006).
86. Bankston, C. P. Experimental and Systems Studies of the Alkali Metal Thermoelectric Converter for Aerospace Power. *J. Energy* **7**, 442–448 (1983).
87. Ivanenok, J. F., Sievers, R. K., Hunt, T. K. & Johnson, G. A. Radioisotope AMTEC Power System Designs for Spacecraft Applications. *IEEE Aerosp. Electron. Syst. Mag.* **8**, 35–39 (1993).
88. Mingo, N. & Broido, D. A. Lattice Thermal Conductivity Crossovers in Semiconductor Nanowires. *Phys. Rev. Lett.* **93**, 246106 (2004).
89. LaPierre, R. R. *et al.* III-V Nanowire Photovoltaics: Review of Design for High Efficiency. *PSS (RRL)* **7**, 815–830 (2013).
90. HoSung, L. *Thermoelectrics: Design and Materials*. (John Wiley & Sons, 2016).
91. Datta, S. *Electronic Transport in Mesoscopic Systems*. (Cambridge University Press, 1997).
92. Esposito, M., Lindenberg, K. & Van den Broeck, C. Thermoelectric Efficiency at Maximum Power in a Quantum Dot. *Europhys. Lett.* **85**, 60010 (2009).

93. Goldsmid, H. *Thermoelectric Refrigeration*. (Springer, 2013).
94. Vurgaftman, I., Meyer, J. R. & Ram-Mohan, L. R. Band Parameters for III-V Compound Semiconductors and Their Alloys. *J. Appl. Phys.* **89**, 5815–5875 (2001).
95. Kane, E. O. Band Structure of Indium Antimonide. *J. Phys. Chem. Solids* **1**, 249–261 (1957).
96. Rode, D. L. Electron Mobility in Direct-Gap Polar Semiconductors. *Phys. Rev. B* **2**, 1012–1024 (1970).
97. Robinett, R. W. Quantum Mechanics of the Two-Dimensional Circular Billiard Plus Baffle System and Half-Integral Angular Momentum. *Eur. J. Phys.* **24**, 231–243 (2003).
98. Abramowitz, M. & Stegun, I. A. *Handbook of Mathematical Functions with Formulas, Graphs, and Mathematical Tables*. (U.S. Government Printing Office, 1948).
99. Singh, J. *Modern Physics for Engineers*. (John Wiley & Sons, 2008).
100. Fishman, G. Phonon-Limited Mobility in a Quasi-One-Dimensional Semiconductor. *Phys. Rev. B* **36**, 7448–7456 (1987).
101. Hirakawa, K. & Sakaki, H. Mobility of the Two-Dimensional Electron Gas at Selectively Doped n-type $\text{Al}_x\text{Ga}_{1-x}\text{As}/\text{GaAs}$ Heterojunctions with Controlled Electron Concentrations. *Phys. Rev. B* **33**, 8291–8303 (1986).
102. Rode, D. L. Low-field Electron Transport. in *Semiconductors and Semimetals* vol. 10 1–89 (Elsevier, 1975).

103. Lee, J. & Spector, H. N. Dielectric Response Function for a Quasi-One-Dimensional Semiconducting System. *J. Appl. Phys.* **57**, 366–372 (1985).
104. Wang, J. & Leburton, J. P. Plasmon Dispersion Relation of a Quasi-One-Dimensional Electron Gas. *Phys. Rev. B* **41**, 7846–7849 (1990).
105. Zhang, L. *et al.* Suppressing the Bipolar Contribution to the Thermoelectric Properties of $\text{Mg}_2\text{Si}_{0.4}\text{Sn}_{0.6}$ by Ge Substitution. *J. Appl. Phys.* **117**, 155103 (2015).
106. Rode, D. L. Electron Transport in InSb, InAs, and InP. *Phys. Rev. B* **3**, 3287–3299 (1971).
107. Baraff, G. A. Maximum Anisotropy Approximation for Calculating Electron Distributions; Application to High Field Transport in Semiconductors. *Phys. Rev.* **133**, A26–A33 (1964).
108. Rode, D. L. & Knight, S. Electron Transport in GaAs. *Phys. Rev. B* **3**, 2534–2541 (1971).
109. Sofo, J. O. & Mahan, G. D. Optimum Band Gap of a Thermoelectric Material. *Phys. Rev. B* **49**, 4565–4570 (1994).
110. Mingo, N. Calculation of Si Nanowire Thermal Conductivity Using Complete Phonon Dispersion Relations. *Phys. Rev. B* **68**, 113308 (2003).
111. Freedman, J. P. *et al.* Universal Phonon Mean Free Path Spectra in Crystalline Semiconductors at High Temperature. *Sci. Rep.* **3**, 2963 (2013).
112. Holland, M. G. Analysis of Lattice Thermal Conductivity. *Phys. Rev.* **132**, 2461–2471 (1963).

113. Carlson, R. O., Slack, G. A. & Silverman, S. J. Thermal Conductivity of GaAs and GaAs_{1-x}P_x Laser Semiconductors. *J. Appl. Phys.* **36**, 505–507 (1965).
114. Fedorov, V. V., Dvoretckaia, L. N., Kirilenko, D. A., Mukhin, I. S. & Dubrovskii, V. G. Formation of Wurtzite Sections in Self-Catalyzed GaP Nanowires by Droplet Consumption. *Nanotechnology* **32**, 495601 (2021).
115. Panciera, F. *et al.* Phase Selection in Self-Catalyzed GaAs Nanowires. *Nano Lett.* **20**, 1669–1675 (2020).
116. Elyamny, S., Dimaggio, E., Magagna, S., Narducci, D. & Pennelli, G. High Power Thermoelectric Generator Based on Vertical Silicon Nanowires. *Nano Lett.* **20**, 4748–4753 (2020).
117. Bin Xu, Khouri, W. & Fobelets, K. Two-Sided Silicon Nanowire Array/Bulk Thermoelectric Power Generator. *IEEE Electron Device Lett.* **35**, 596–598 (2014).
118. Curtin, B. M., Fang, E. W. & Bowers, J. E. Highly Ordered Vertical Silicon Nanowire Array Composite Thin Films for Thermoelectric Devices. *J. Electron. Mater.* **41**, 887–894 (2012).
119. Li, Y., Buddharaju, K., Singh, N., Lo, G. Q. & Lee, S. J. Chip-Level Thermoelectric Power Generators Based on High-Density Silicon Nanowire Array Prepared with Top-Down CMOS Technology. *IEEE Electron Device Lett.* **32**, 674–676 (2011).
120. Keyani, J., Stacy, A. M. & Sharp, J. Assembly and Measurement of a Hybrid Nanowire-Bulk Thermoelectric Device. *Appl. Phys. Lett.* **89**, 233106 (2006).

121. Wang, W., Jia, F., Huang, Q. & Zhang, J. A New Type of Low Power Thermoelectric Micro-Generator Fabricated by Nanowire Array Thermoelectric Material. *Microelectron. Eng.* **77**, 223–229 (2005).
122. Abramson, A. R. *et al.* Fabrication and Characterization of a Nanowire/Polymer-Based Nanocomposite for a Prototype Thermoelectric Device. *J. Microelectromech. Syst.* **13**, 505–513 (2004).
123. Borca-Tasciuc, T., Kumar, A. R. & Chen, G. Data Reduction in 3ω Method for Thin-Film Thermal Conductivity Determination. *Rev. Sci. Instrum.* **72**, 2139–2147 (2001).
124. Paterson, J., Singhal, D., Tainoff, D., Richard, J. & Bourgeois, O. Thermal Conductivity and Thermal Boundary Resistance of Amorphous Al_2O_3 Thin Films on Germanium and Sapphire. *J. Appl. Phys.* **127**, 245105 (2020).
125. Singhal, D. *et al.* Nanowire Forest of Pnictogen–Chalcogenide Alloys for Thermoelectricity. *Nanoscale* **11**, 13423–13430 (2019).
126. Singhal, D. *et al.* Measurement of Anisotropic Thermal Conductivity of a Dense Forest of Nanowires Using the 3ω Method. *Rev. Sci. Instrum.* **89**, 084902 (2018).
127. Dames, C. Measuring the Thermal Conductivity of Thin Films: 3ω and Related Electrothermal Methods. *Annu. Rev. Heat Transf.* **16**, 43 (2013).
128. Dames, C. & Chen, G. 1ω , 2ω , and 3ω Methods for Measurements of Thermal Properties. *Rev. Sci. Instrum.* **76**, 124902 (2005).
129. Martin, P. N., Aksamija, Z., Pop, E. & Ravaioli, U. Reduced Thermal Conductivity in Nanoengineered Rough Ge and GaAs Nanowires. *Nano Lett.* **10**, 1120–1124 (2010).

130. Olson, B. W., Graham, S. & Chen, K. A Practical Extension of the 3ω Method to Multilayer Structures. *Rev. Sci. Instrum.* **76**, 053901 (2005).
131. Li, Z., Sun, Q., Yao, X. D., Zhu, Z. H. & Lu, G. Q. (Max). Semiconductor Nanowires for Thermoelectrics. *J. Mater. Chem.* **22**, 22821 (2012).
132. Kim, J. *et al.* Thermoelectricity in Semiconductor Nanowires: Thermoelectricity in Semiconductor Nanowires. *PSS (RRL)* **7**, 767–780 (2013).
133. Rao, T. V. C. *et al.* Electrical Transport in InAs/GaSb Superlattice: Role of Surface States and Interface Roughness. *Semicond. Sci. Technol.* **27**, 105025 (2012).
134. Leshchenko, E. D., Kuyanov, P., LaPierre, R. R. & Dubrovskii, V. G. Tuning the Morphology of Self-Assisted Gap Nanowires. *Nanotechnology* **29**, 225603 (2018).
135. Dubrovskii, V. G., Sibirev, N. V., Halder, N. N. & Ritter, D. Classification of the Morphologies and Related Crystal Phases of III-V Nanowires Based on the Surface Energy Analysis. *J. Phys. Chem. C* **123**, 18693–18701 (2019).
136. Daly, B. C., Maris, H. J., Imamura, K. & Tamura, S. Molecular Dynamics Calculation of the Thermal Conductivity of Superlattices. *Phys. Rev. B* **66**, 024301 (2002).
137. France-Lanord, A., Merabia, S., Albaret, T., Lacroix, D. & Termentzidis, K. Thermal Properties of Amorphous/Crystalline Silicon Superlattices. *J. Phys.: Condens. Matter* **26**, 355801 (2014).
138. Plimpton, S. Fast Parallel Algorithms for Short-Range Molecular Dynamics. *J. Comput. Phys.* **177**, 1–19 (1995).

139. Albe, K., Nordlund, K., Nord, J. & Kuronen, A. Modeling of Compound Semiconductors: Analytical Bond-Order Potential for Ga, As, and GaAs. *Phys. Rev. B* **66**, 035205 (2002).
140. Togo, A. & Tanaka, I. First Principles Phonon Calculations in Materials Science. *Scr. Mater.* **108**, 1–5 (2015).
141. Pfund, A. *et al.* Fabrication of Semiconductor Nanowires for Electronic Transport Measurements. *CHIMIA* **60**, 729–734 (2006).
142. Suyatin, D. B., Thelander, C., Björk, M. T., Maximov, I. & Samuelson, L. Sulfur Passivation for Ohmic Contact Formation to InAs Nanowires. *Nanotechnology* **18**, 105307 (2007).
143. Li, Z., Tan, H. H., Jagadish, C. & Fu, L. III-V Semiconductor Single Nanowire Solar Cells: a Review. *Adv. Mater. Technol.* **3**, 1800005 (2018).
144. Soci, C. *et al.* Nanowire Photodetectors. *J. Nanosci. Nanotechnol.* **10**, 1430–1449 (2010).
145. Zhang, Y., Wu, J., Aagesen, M. & Liu, H. III-V Nanowires and Nanowire Optoelectronic Devices. *J. Phys. D: Appl. Phys.* **48**, 463001 (2015).
146. Algra, R. E. *et al.* The Role of Surface Energies and Chemical Potential during Nanowire Growth. *Nano Lett.* **11**, 1259–1264 (2011).
147. Pishchagin, A. *et al.* Dynamics of Droplet Consumption in Vapor–Liquid–Solid III-V Nanowire Growth. *Cryst. Growth Des.* (2021).

148. Oehler, F. *et al.* Measuring and Modeling the Growth Dynamics of Self-Catalyzed GaP Nanowire Arrays. *Nano Lett.* **18**, 701–708 (2018).
149. Harmand, J.-C. *et al.* Atomic Step Flow on a Nanofacet. *Phys. Rev. Lett.* **121**, 166101 (2018).
150. Kim, W. *et al.* Bistability of Contact Angle and Its Role in Achieving Quantum-Thin Self-Assisted GaAs nanowires. *Nano Lett.* **18**, 49–57 (2018).
151. Jacobsson, D. *et al.* Interface Dynamics and Crystal Phase Switching in GaAs Nanowires. *Nature* **531**, 317–322 (2016).
152. Glas, F. Vapor Fluxes on the Apical Droplet During Nanowire Growth by Molecular Beam Epitaxy: Vapor Fluxes on the Apical Droplet. *PSS (B)* **247**, 254–258 (2010).
153. Glas, F., Ramdani, M. R., Patriarche, G. & Harmand, J.-C. Predictive Modeling of Self-Catalyzed III-V Nanowire Growth. *Phys. Rev. B* **88**, 195304 (2013).
154. Colombo, C., Spirkoska, D., Frimmer, M., Abstreiter, G. & Fontcuberta i Morral, A. Ga-assisted Catalyst-Free Growth Mechanism of GaAs Nanowires by Molecular Beam Epitaxy. *Phys. Rev. B* **77**, 155326 (2008).
155. Plissard, S., Larrieu, G., Wallart, X. & Caroff, P. High Yield of Self-Catalyzed GaAs Nanowire Arrays Grown on Silicon via Gallium Droplet Positioning. *Nanotechnology* **22**, 275602 (2011).
156. Schroth, P. *et al.* Radial Growth of Self-Catalyzed GaAs Nanowires and the Evolution of the Liquid Ga-Droplet Studied by Time Resolved in-situ X-ray Diffraction. *Nano Lett.* **18**, 101-108 (2018).

157. Tauchnitz, T. *et al.* Decoupling the Two Roles of Ga Droplets in the Self-Catalyzed Growth of GaAs Nanowires on SiO_x/Si(111) Substrates. *Cryst. Growth Des.* **17**, 5276–5282 (2017).
158. Uryupin, O. N. *et al.* Thermoelectric Properties of InSb Nanowires over a Wide Temperature Range. *J. Electron. Mater.* **38**, 990–993 (2009).
159. Du, S. *et al.* Quantitative Dopant Distributions in GaAs Nanowires Using Atom Probe Tomography. *Ultramicroscopy* **132**, 186–192 (2013).
160. Dastjerdi, M. H. T. *et al.* Three-Fold Symmetric Doping Mechanism in GaAs Nanowires. *Nano Lett.* **17**, 5875–5882 (2017).
161. Anyebe, E. A. *et al.* Surfactant Effect of Antimony Addition to the Morphology of Self-Catalyzed InAs_{1-x}Sb_x Nanowires. *Nano Res.* **8**, 1309–1319 (2015).
162. Wilson, D. P., Dubrovskii, V. G. & LaPierre, R. R. Improving the Yield of GaAs Nanowires on Silicon by Ga Pre-Deposition. *Nanotechnology* **32**, 265301 (2021).
163. Dubrovskii, V. G., Hijazi, H., Goktas, N. I. & LaPierre, R. R. Be, Te, and Si Doping of GaAs Nanowires: Theory and Experiment. *J. Phys. Chem. C* **124**, 17299–17307 (2020).
164. Pinel, S. *et al.* Thermal Modeling and Management in Ultrathin Chip Stack Technology. *IEEE Trans. Comp. Packag. Technol.* **25**, 244–253 (2002).
165. Gracias, A., Tokranova, N., Thelen, B. C. M. & Castracane, J. Influence of Diamond Nanoparticles on the Thermal Properties of Benzocyclobutene (BCB). *PSS (A)* **208**, 684–690 (2011).

166. Moghaddam, S., Kiger, K. T., Modafe, A. & Ghodssi, R. A Novel Benzocyclobutene-Based Device for Studying the Dynamics of Heat Transfer During the Nucleation Process. *J. Microelectromech. Syst.* **16**, 1355–1366 (2007).
167. Yang, J. *Processing Procedures for CYCLOTENE 3000 Series Dry Etch Resins*. Dow Chemical Co. (2005).
168. Modafe, A., Ghalichechian, N., Powers, M., Khbeis, M. & Ghodssi, R. Embedded Benzocyclobutene in Silicon: An Integrated Fabrication Process for Electrical and Thermal Isolation in MEMS. *Microelectron. Eng.* **82**, 154–167 (2005).
169. Slack, G. A. Thermal Conductivity of Pure and Impure Silicon, Silicon Carbide, and Diamond. *J. Appl. Phys.* **35**, 3460–3466 (1964).
170. Maycock, P. D. Thermal Conductivity of Silicon, Germanium, III-V Compounds and III-V Alloys. *Solid-State Electron.* **10**, 161–168 (1967).
171. Flubacher, P., Leadbetter, A. J. & Morrison, J. A. The Heat Capacity of Pure Silicon and Germanium and Properties of Their Vibrational Frequency Spectra. *Philos. Mag.* **4**, 273–294 (1959).
172. Mingo, N. & Yang, L. Phonon Transport in Nanowires Coated with an Amorphous Material: an Atomistic Green's Function Approach. *Phys. Rev. B* **68**, 245406 (2003).
173. Guinea, F., Tejedor, C., Flores, F. & Louis, E. Effective Two-Dimensional Hamiltonian at Surfaces. *Phys. Rev. B* **28**, 4397–4402 (1983).

174. Sancho, M. P. L., Sancho, J. M. L., Sancho, J. M. L. & Rubio, J. Highly Convergent Schemes for the Calculation of Bulk and Surface Green Functions. *J. Phys. F: Met. Phys.* **15**, 851–858 (1985).

Appendix

I. Figure of Merit for Various Nanowire Materials

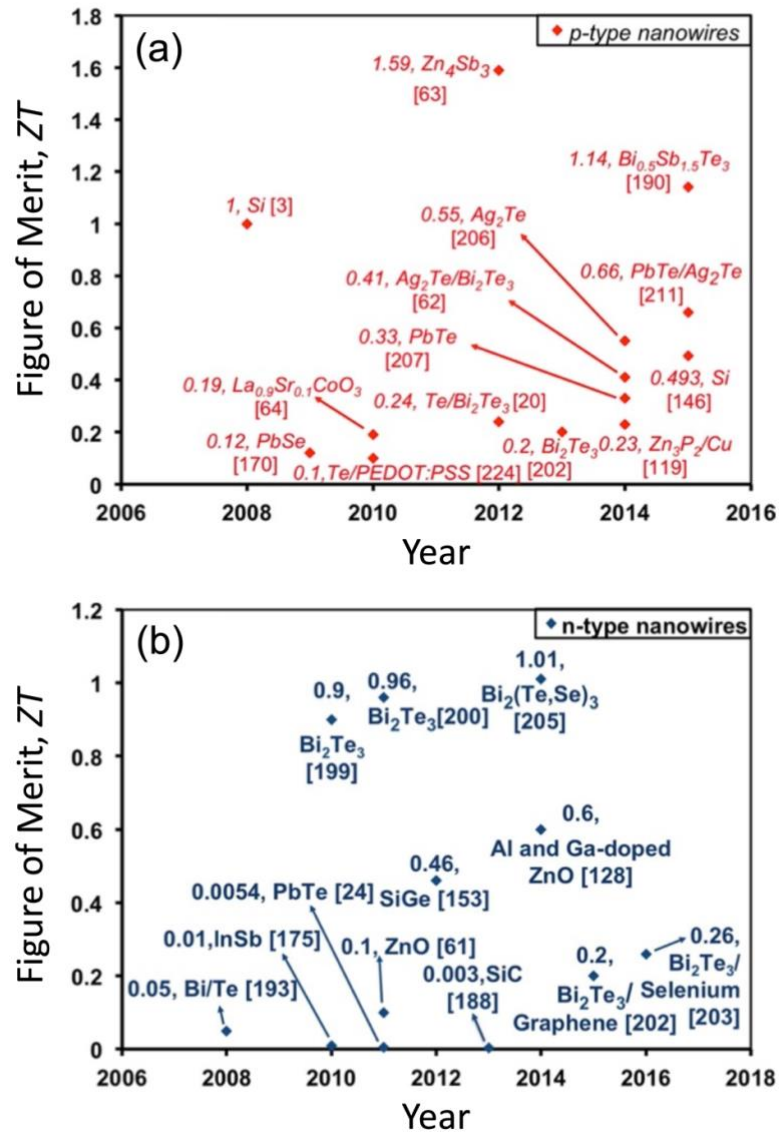


Figure A1: Maximal ZT values (at various temperatures) for recent (a) p-type and (b) n-type NW thermoelectrics. Reprinted with permission from Ref. 24.

II. Bulk Scattering and Band Formulae

Here we present the explicit formulae for the scattering functions $S_{\text{in/out}}^{\pm}$, which were determined by Rode¹⁰⁶ based on the Kane band structure⁹⁵:

$$S_{\text{in}}^{\pm} = \left[N_{\text{po}} + \frac{1}{2} \pm \left(\frac{1}{2} - f_0 \right) \right] \lambda_{\text{in}}^{\pm} \quad (\text{A1})$$

$$S_{\text{out}}^{\pm} = \left[N_{\text{po}} + \frac{1}{2} \pm \left(f_0^{\pm} - \frac{1}{2} \right) \right] \lambda_{\text{out}}^{\pm} \quad (\text{A2})$$

$$\lambda_{\text{in}}^{\pm} = \gamma^{\pm} \left[\frac{(k^{\pm})^2 + k^2}{2k^{\pm}k} (A^{\pm})^2 \ln \left| \frac{k^{\pm} - k}{k^{\pm} + k} \right| - (A^{\pm})^2 - \frac{c^2(c^{\pm})^2}{3} \right] \quad (\text{A3})$$

$$\lambda_{\text{out}}^{\pm} = \gamma^{\pm} \left[(A^{\pm})^2 \ln \left| \frac{k^{\pm} - k}{k^{\pm} + k} \right| - A^{\pm}cc^{\pm} - aa^{\pm}cc^{\pm} \right] \quad (\text{A4})$$

$$\gamma^{\pm} = \frac{e^2 \omega_{\text{po}} m^*}{4\pi \hbar^2 k} \left(\frac{1}{\epsilon_{\infty}} - \frac{1}{\epsilon_0} \right) \quad (\text{A5})$$

$$A^{\pm} = aa^{\pm} + \left(\frac{(k^{\pm})^2 + k^2}{2k^{\pm}k} \right) cc^{\pm} \quad (\text{A6})$$

The coefficients $a(k)$ and $c(k)$ of the s - and p -like basis functions are given by⁹⁶

$$a(k) = \sqrt{\frac{1}{2} + \frac{1}{2\alpha(k)}} \quad (\text{A7})$$

$$c(k) = \sqrt{1 - [a(k)]^2} \quad (\text{A8})$$

The elastic scattering rate τ_{el}^{-1} is the sum of the following three components, which correspond to piezoelectric scattering, acoustic deformation potential scattering, and ionized impurity scattering in the bulk, respectively:

$$\frac{1}{\tau_{\text{pe}}} = \frac{e^2 k_B T P_z^2 m^*}{6\pi \hbar^3 \epsilon_0 k} (3 - 6c^2 + 4c^4) \quad (\text{A9})$$

$$\frac{1}{\tau_{ac}} = \frac{k_B T E_1^2 m^* k}{3\pi \hbar^3 c_l} (3 - 8c^2 + 6c^4) \quad (\text{A10})$$

$$\frac{1}{\tau_{ii}} = \frac{e^4 N m^*}{8\pi \epsilon_0^2 \hbar^3 k^3} \left[D \ln \left(1 + \frac{4k^2}{\beta^2} \right) - B \right] \quad (\text{A11})$$

The inverse screening length β for the Coulomb potential is given by

$$\beta^2 = \frac{e^2}{\pi^2 \epsilon_0 k_B T} \int_0^\infty k^2 f_0 (1 - f_0) dk \quad (\text{A12})$$

and the parameters D and B in Eq. (A11) are calculated from

$$D = 1 + \frac{2\beta^2 c^2}{k^2} + \frac{3\beta^4 c^4}{4k^4} \quad (\text{A13})$$

$$B = \frac{1}{\beta^2 + 4k^2} \left[4k^2 + 8c^2(\beta^2 + 4k^2) + \frac{(3\beta^4 + 6\beta^2 k^2 - 8k^4)c^4}{k^2} \right] \quad (\text{A14})$$

The non-parabolic bulk dispersion (Eqs. (2.31) and (2.32)) can be inverted for the magnitude of the electron wave vector ($k > 0$) using

$$k(E) = \sqrt{\frac{(x(E))^2 - 1}{a_3}} \quad (\text{A15})$$

$$x(E) = \left(\frac{a_3}{2a_1} \right) \left[\sqrt{a_2^2 + \frac{4a_1}{a_3} \left(a_2 + \frac{a_1}{a_3} + E \right)} - a_2 \right] \quad (\text{A16})$$

$$a_1 = \frac{\hbar^2}{2m_e} \quad (\text{A17})$$

$$a_2 = \frac{1}{2} E_g \quad (\text{A18})$$

$$a_3 = \left(\frac{2\hbar^2}{E_g} \right) \frac{(m_e - m^*)}{m_e m^*} \quad (\text{A19})$$

III. 3ω Parameters and Supplementary Information

a. Nanowire Growth

Arrays of GaAs NWs were grown on 300 μm thick p⁺-Si substrates ($\rho \leq 0.005 \Omega \cdot \text{cm}$) with a <111> surface orientation. Using plasma-enhanced chemical vapour deposition (PECVD), 30 nm of SiO_x was deposited on the substrate surface. To provide nanowire (NW) nucleation sites, arrays of holes were etched through the surface oxide in a hexagonal array pattern with a pitch of 360 nm, using electron beam lithography and reactive ion etching. The total extent of the array was confined to a $2 \times 2 \text{ mm}^2$ area on the substrate surface, as defined by the oxide template. GaAs NWs were grown by the self-assisted vapor-liquid-solid method, with a Ga droplet as the seed particle, using gas source molecular beam epitaxy. Ga was supplied from an effusion source and group V elements were supplied as dimers from a hydride gas cracker.

The polytypic zincblende/wurtzite NWs (sample A) and twinning superlattice (TSL) NWs (sample B) arrays were grown using identical processes, apart from the dopant flux introduced in the latter that is used to induce a TSL structure.⁶⁰ A 250 s Ga pre-deposition and the brief growth of a short GaP base were employed to improve the NW yield.¹⁶² GaAs NWs were then grown in three segments: (i) 50 min at a substrate temperature of 630 °C, (ii) a ramp down to 537 °C over the next 50 min, and (iii) a final 30 min of growth at 537 °C. This process ensured a high NW yield at the beginning of growth, followed by a low temperature required for TSL formation in sample B. During the growth of sample B, a Be dopant flux supplied from an elemental effusion cell was

introduced in segment (i) at a NW dopant concentration of $6.0 \times 10^{17} \text{ cm}^{-3}$, then ramped up in segment (ii), and finally held at $3.0 \times 10^{19} \text{ cm}^{-3}$ in segment (iii). The Be dopant flux was increased gradually to avoid Ga droplet instability associated with a high dopant flux. This process is detailed in Figure A2. The incorporated dopant concentration was based on previous calibrations^{64,163} and no intentional dopants were introduced in sample A.

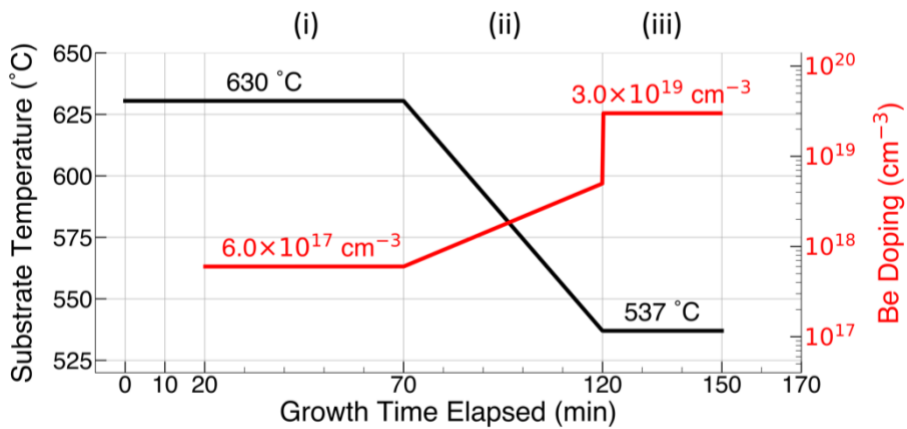


Figure A2: Growth conditions over time, showing the substrate temperature and actual dopant concentration.

b. Heater Line Resistance Coefficients

The measured $R(T)$ data points, from which the resistance coefficients are determined, are shown in Figures A2-A4, for samples A, B, and C, respectively. In each case, the dashed line represents the best-fit and corresponding slope, whereas the blue and red lines indicate the minimum and maximum slope, respectively, within limits of the measurement uncertainty.

Owing to the precision of the resistance measurements, a maximum error of $\pm 1.6\%$ was observed for the slope $\frac{dR}{dT}$ across all samples; hence we determine the resistance coefficients to within 2% error.

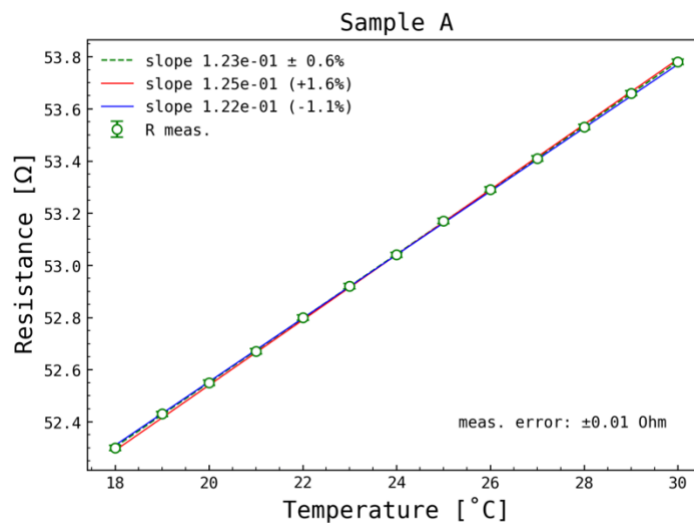


Figure A3: Temperature dependence of the line resistance for sample A.

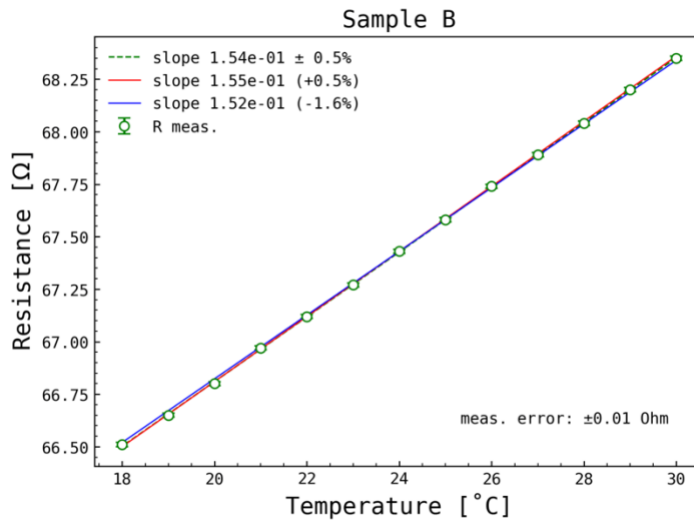


Figure A4: Temperature dependence of the line resistance for sample B.

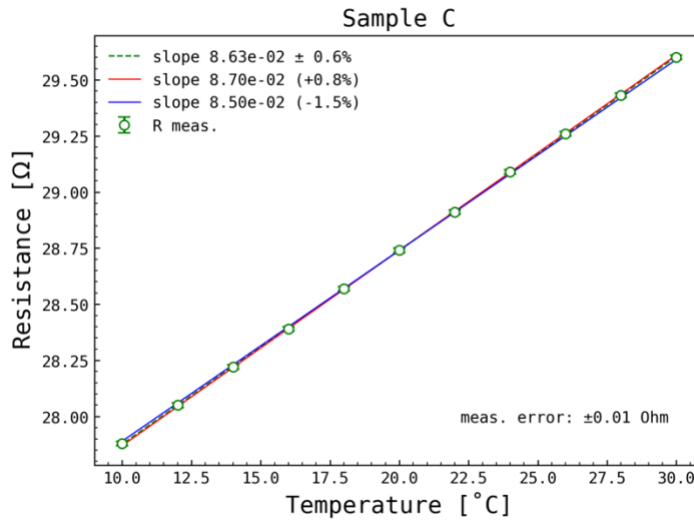


Figure A5: Temperature dependence of the line resistance for sample C.

c. Model Sensitivity

To illustrate the sensitivity of the mean-squared-error objective function

$$\bar{\epsilon}(\vec{\chi}) = \frac{1}{M} \sum_{k=1}^M \|\tilde{\theta}_{2\omega_k} - \tilde{T}_h(\omega_k, \vec{\chi})\|^2 \quad (\text{A20})$$

to individual parameter values, χ_i , we varied the i^{th} component of best fit vector $\vec{\chi}^*$ by $\pm 50\%$ and recorded the resulting change in $\bar{\epsilon}$. Parameters exhibiting high sensitivity are marked by a steep descent into a pronounced minimum for $\bar{\epsilon}$ at χ_i^* (i.e., near 0% perturbation). Conversely, the variation yields much smaller changes for low-sensitivity parameters, namely the heat capacities of layers (2) and (3) in samples A and B. This is evident in Figure A6, where $\vec{\chi}^*(B)$ was varied by perturbing the layer properties of sample B. Figure A6 also demonstrates that the properties of the uppermost layer have the greatest influence on $\bar{\epsilon}$. Thus, the accuracy of the measurement increases with proximity of the target layer to the heater line.

While the theoretical heat model surmised by Eqs. (3.2) to (3.5) in the main text can in principle include an arbitrary number of layers, the effective penetration depth¹²³

$$q^{-1} = \sqrt{\frac{\kappa}{2\omega C}} \quad (\text{A21})$$

must be taken into consideration vis a vis the total thickness of the sample and constituent layers. Figure A7 shows the approximate penetration depth through BCB and the NW-BCB composite, calculated from Eq. (A2), using our results in Tables A1-S3. In both samples A and B, the BCB and composite layers had a combined height of about $6 \mu\text{m}$, whereas sample C had only the $3 \mu\text{m}$ of BCB. Accordingly, the plot of the

penetration depth, Figure A7, indicates complete thermal probing in all three measurement devices, over nearly all the measured frequencies.

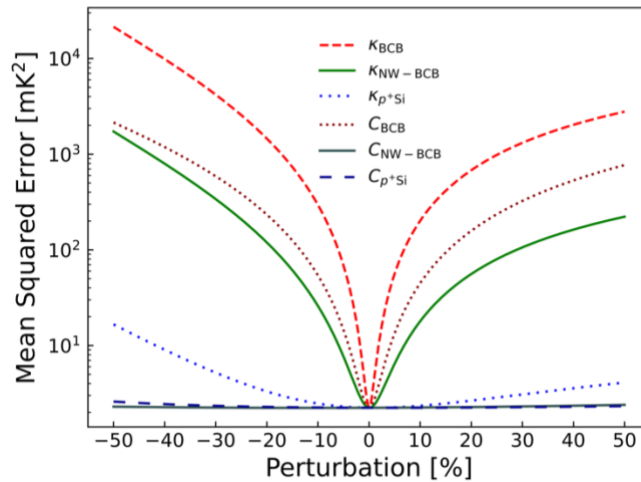


Figure A6: Sensitivity of the objective function versus perturbations about the best fit values. The upper three curves indicate a strong sensitivity to the thermal conductivities of the BCB and NW-BCB layers, as well as the volumetric heat capacity of the BCB. A weaker sensitivity to the substrate (p^+ -Si) thermal conductivity is also seen.

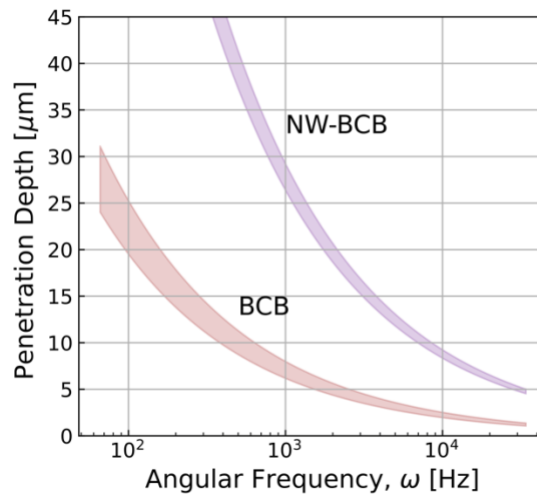


Figure A7: Thermal penetration depth (q^{-1}) in μm , calculated using Eq. (S2), using the range of values for BCB and the NW-BCB composite from Tables S1-S3.

d. Tables of Fitted Parameters

The thermophysical properties of all layers across the three samples, as determined by three fitting paradigms, (i)-(iii), are tabulated in Tables A1-A3. Error estimates are included on the parameter values for which the model exhibits high sensitivity (discussed in Appendix III-d). The results for the anisotropy ratio $\psi = \kappa_{\parallel}/\kappa_{\perp}$ were on the order of 10^{-7} for both sample A and sample B, suggesting highly one-dimensional heat flow through the NW-BCB composites. For the uniform BCB layer in sample C, we fixed $\psi = 1$. Reference value ranges are provided, where available, in the rightmost columns of each table. All entries in the columns (i)-(iii) represent fitted parameter values for the corresponding fit paradigm, except for underlined values, which indicate constant parameters, and values of the mean-squared-error (MSE), $\bar{\epsilon}$. Fitted parameters exceeding their reasonable physical range are emphasized in italic text.

We note immediately that the inclusion of $r_{\text{th}} \neq 0$ improves the fitting error by at least an order of magnitude, so paradigm (i) was discounted. Regarding paradigms (ii) and (iii), we note that thermal conductivity results for the BCB and NW-BCB layers agree within uncertainty for all three samples. Indeed, the heater thermal mass has only a small effect on the measured thermal conductivity (as per Section V of Ref. 123), considering the relative dimensions and heat capacity of the heater line versus that of the target layers. Paradigm (ii) was chosen over (iii) because it produced no unphysical values as well as the lowest overall MSE across the three samples.

Table A1: Fitted parameter values for sample A.

parameter	units	(i)	(ii)	(iii)	ref. value
		$C_h d_h, r_{th} = 0$	$r_{th} \neq 0$	$C_h d_h, r_{th} \neq 0$	
κ_{BCB}	W/m-K	0.546 ± 0.03	0.19 ± 0.04	0.17 ± 0.04	$(0.18 - 0.29)^{164-167}$
C_{BCB}	J/cm ³ -K	1.10 ± 0.03	1.88 ± 0.04	1.99 ± 0.04	$(2.19 - 2.29)^{164,168}$
κ_{BCB-NW}	W/m-K	0.20 ± 0.05	0.65 ± 0.04	0.70 ± 0.06	
C_{BCB-NW}	J/cm ³ -K	3.70×10^{-7}	0.41	4.57×10^{-7}	
κ_{p+Si}	W/m-K	266	67	46	$(35 - 55)^{169}$
C_{p+Si}	J/cm ³ -K	0.0920	1.22	0.97	-
r_{th}	cm ² -K/W	<u>0</u>	0.0114	0.028	-
C_h	J/cm ³ -K	<u>0</u>	<u>0</u>	<u>2.82</u>	$(2.82)^4$
d_h	nm	<u>0</u>	<u>0</u>	<u>157</u>	-
$\bar{\epsilon}$	10 ⁻³ K ²	19.2	2.25	1.92	

Table A2: Fitted parameter values for sample B.

parameter	units	(i)	(ii)	(iii)	ref. value
		$C_h d_h, r_{th} = 0$	$r_{th} \neq 0$	$C_h d_h, r_{th} \neq 0$	
κ_{BCB}	W/m-K	0.47 ± 0.02	0.19 ± 0.04	0.17 ± 0.04	$(0.18 - 0.29)^{164-167}$
C_{BCB}	J/cm ³ -K	1.18 ± 0.04	1.93 ± 0.04	2.02 ± 0.04	$(2.19 - 2.29)^{164,168}$
κ_{BCB-NW}	W/m-K	0.20 ± 0.05	0.61 ± 0.04	0.68 ± 0.07	
C_{BCB-NW}	J/cm ³ -K	2.91	0.38	0.37	
κ_{p+Si}	W/m-K	8.46×10^5	57	48	$(35 - 55)^{169}$
C_{p+Si}	J/cm ³ -K	4.68	2.02	2.05	-
r_{th}	cm ² -K/W	<u>0</u>	0.010	0.027	-
C_h	J/cm ³ -K	<u>0</u>	<u>0</u>	<u>2.82</u>	$(2.82)^4$
d_h	nm	<u>0</u>	<u>0</u>	<u>157</u>	-
$\bar{\epsilon}$	10 ⁻³ K ²	39.2	2.23	3.01	

Table A3: Fitted parameter values for sample C.

parameter	units	(i)	(ii)	(iii)	ref. value
		$C_h d_h, r_{th} = 0$	$r_{th} \neq 0$	$C_h d_h, r_{th} \neq 0$	
κ_{BCB}	W/m-K	0.20 ± 0.03	0.19 ± 0.03	0.17 ± 0.03	$(0.18 - 0.29)^{164-167}$
C_{BCB}	J/cm ³ -K	2.22 ± 0.05	1.85 ± 0.05	2.05 ± 0.05	$(2.19 - 2.29)^{164,168}$
κ_{Si}	W/m-K	256	142	5.03×10^4	$(145 - 156)^{19,170}$
C_{Si}	J/cm ³ -K	1.87	1.82	1.91	$(1.66)^{171}$
r_{th}	cm ² -K/W	<u>0</u>	0.012	0.025	-
C_h	J/cm ³ -K	<u>0</u>	<u>0</u>	<u>2.82</u>	$(2.82)^4$
d_h	nm	<u>0</u>	<u>0</u>	<u>157</u>	-
$\bar{\epsilon}$	10 ⁻³ K ²	143	1.30	11.7	

IV. Computational Details

a. Molecular Dynamics

Thermal conductivity is size-dependent in non-equilibrium molecular dynamics simulations (NEMD), increasing with the size of the simulation cell. We find that this change becomes negligible near a nanowire length of 350 nm in our studies, as shown in Figure A8, for example. The nanowire length is truncated at 350 nm to minimize the duration of NEMD simulations.

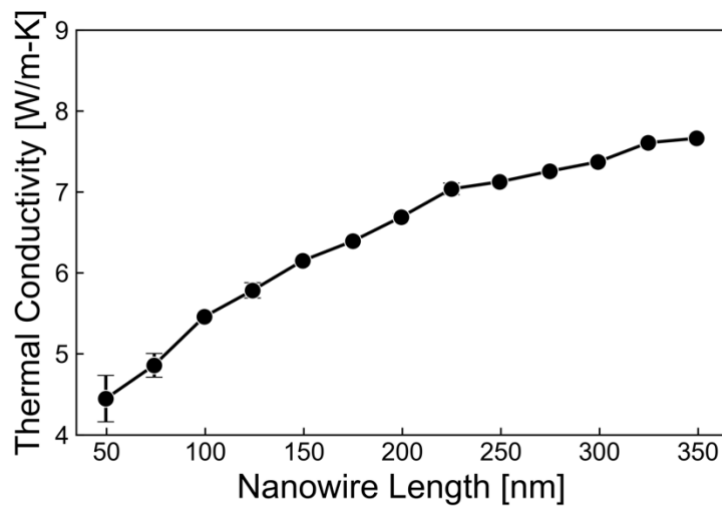


Figure A8: Saturation of the thermal conductivity in non-equilibrium molecular dynamics simulations. Data points correspond to a zincblende nanowire with diameter 50 Å.

b. Atomistic Green's Function

An excellent introduction to the atomistic Green's function (AGF) method can be found in Refs. 78 and 79. Here, we summarize the basic procedure and details relevant to our implementation.

The harmonic matrix for entire system can be partitioned into blocks:

$$\mathbf{H}_{\text{tot}} = \begin{bmatrix} \mathbf{H}_1 & \boldsymbol{\tau}_1^\dagger & 0 \\ \boldsymbol{\tau}_1 & \mathbf{H}_d & \boldsymbol{\tau}_2 \\ 0 & \boldsymbol{\tau}_2^\dagger & \mathbf{H}_2 \end{bmatrix} \quad (\text{A22})$$

where subscripts 1, d , and 2 correspond to the first contact, the device region, and the second contact, respectively. For our purposes, these labels indicate contiguous regions along an arbitrary NW structure; shown as the “device” and two “contact” regions in Figure A9. Interactions among the N_d atoms in the device region are described by the $3N_d \times 3N_d$ submatrix \mathbf{H}_d at the center of \mathbf{H}_{tot} , which is in principle infinitely large. Similarly, the off-diagonal submatrices $\boldsymbol{\tau}_i$ contain the harmonic constants connecting atoms in the device region to either contact ($i = 1, 2$) and *vice versa* for $\boldsymbol{\tau}_i^\dagger$.

To obtain the transmission function, one computes the trace of a matrix product:

$$\mathcal{T}(\omega) = \text{Tr}(\boldsymbol{\Gamma}_1 \mathbf{G} \boldsymbol{\Gamma}_2 \mathbf{G}^\dagger) \quad (\text{A23})$$

where the matrix \mathbf{G} represents the Green's function for the device region:

$$\mathbf{G}(\omega^2) = [\omega^2 \mathbf{I} - \mathbf{H}_d - \boldsymbol{\Sigma}_1(\omega^2) - \boldsymbol{\Sigma}_2(\omega^2)]^{-1} \quad (\text{A24})$$

and the matrices $\boldsymbol{\Gamma}_i = i[\boldsymbol{\Sigma}_i - \boldsymbol{\Sigma}_i^\dagger]$ in Eq. (A23) represent the phonon “escape rate” into either contact. Without the explicit inclusion of boundary scattering,¹⁷² nor other

disordered mechanisms, transmission is limited only by harmonic interface scattering.

Hence, $\mathcal{T}(\omega)$ indicates the “connectivity” of normal modes across the device region.

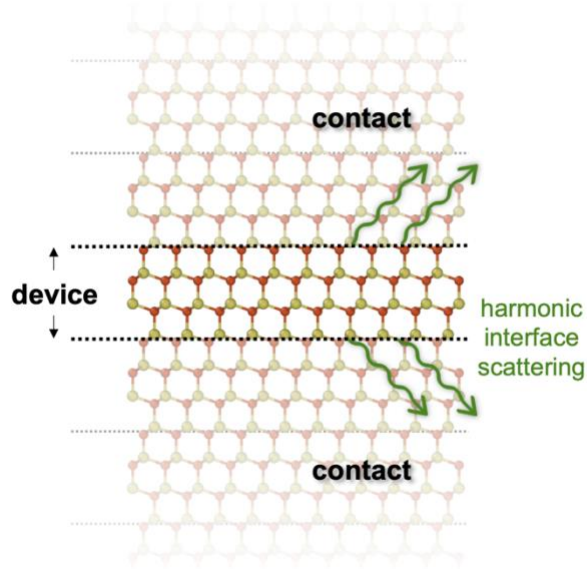


Figure A9: An illustration of the nanowire (NW) system used for atomistic Green’s function calculations. Two semi-infinite “contacts” connect to either end of the “device”, here consisting of one zincblende unit cell. A NW with diameter 35 Å is shown for clarity.

Since the device region is finite, the connection matrices τ_i are populated by finitely many non-zero elements. (This can be understood in terms of atomic interaction distances being effectively finite.) Thus, the self-energy matrices, $\Sigma_i = \tau_i g_i \tau_i^\dagger$, can be computed from finite submatrices by obtaining the surface Green’s functions, g_i^S , of the contacts. We employed the usual decimation technique^{173,174} to approximate g_i^S by recursive renormalization, avoiding explicit inversions of a very large \mathbf{H}_i . Once Σ_i are obtained, the device Green’s function is calculated by matrix inversion, as in Eq. (A24).